76-21,100

VRBA, Frederick John, 1949-
THE MAGNETIC FIELD STRUCTURE AND EMBEDDED
STELLAR POPULATION OF DARK CLOUD COMPLEXES.

The University of Arizona, Ph.D., 1976
Physics, astronomy & astrophysics

THE MAGNETIC FIELD STRUCTURE AND EMBEDDED

STELLAR POPULATION OF DARK CLOUD COMPLEXES

by

Frederick John Vrba

A Dissertation Submitted to the Faculty of the

DEPARTMENT OF ASTRONOMY

In Partial Fulfillment of the Requirements
For the Degree of

DOCTOR OF PHILOSOPHY

In the Graduate College

THE UNIVERSITY OF ARIZONA

1 9 7 6

THE UNIVERSITY OF ARIZONA

GRADUATE COLLEGE

I hereby recommend that this dissertation prepared under my

direction by _____ Frederick John Vrba _____.____

entitled ___ The Magnetic Field Structure and Embedded _____

_____ Stellar Population of Dark Cloud Complexes _____

be accepted as fulfilling the dissertation requirement of the

degree of _____ Doctor of Philosophy _____

_____ Stephen E. Strom _____   ____ 4-5-76 ____
       Dissertation Director   Date

After inspection of the final copy of the dissertation, the

following members of the Final Examination Committee concur in

its approval and recommend its acceptance: [*]

_____   ___ 4 / 5 / 76 ___

_____   _____

_____   _____

_____   _____

_____   _____

[*]This approval and acceptance is contingent on the candidate's
adequate performance and defense of this dissertation at the
final oral examination. The inclusion of this sheet bound into
the library copy of the dissertation is evidence of satisfactory
performance at the final examination.

STATEMENT BY AUTHOR

This dissertation has been submitted in partial fulfillment of requirements for an advanced degree at The University of Arizona and is deposited in the University Library to be made available to borrowers under rules of the Library.

Brief quotations from this dissertation are allowable without special permission, provided that accurate acknowledgment of source is made. Requests for permission for extended quotation from or reproduction of this manuscript in whole or in part may be granted by the head of the major department or the Dean of the Graduate College when in his judgment the proposed use of the material is in the interests of scholarship. In all other instances, however, permission must be obtained from the author.

SIGNED: _Frederick John Vrba_

ACKNOWLEDGMENTS

TABLE OF CONTENTS

TABLE OF CONTENTS--<u>Continued</u>

TABLE OF CONTENTS--<u>Continued</u>

LIST OF TABLES

LIST OF TABLES--<u>Continued</u>

LIST OF ILLUSTRATIONS

LIST OF ILLUSTRATIONS--<u>Continued</u>

ABSTRACT

We have mapped the magnetic field structure of the
massive dark cloud complexes Rho Ophiuchi, R Corona Aus-
trina, NGC 1333, and Lynds 1630 by means of visual, linear
polarization measurements of background stars located at the
periphery of the complexes. In addition, linear polariza-
tion measurements at a wavelength of 2.2μm of stars
embedded in the Ophiuchi dark cloud have established the
magnetic field structure in the denser regions of that cloud.
These data allow us to discuss the importance of magnetic
fields in the evolution of the dark cloud complexes.
Because all of the cloud complexes are active regions of
star formation, we have attempted to examine their evolution
in the context of four suggested mechanisms which may bring
about gravitational collapse: shock wave compression,
Parker instability accretion, cloud-cloud collisions, and
quiescent collapse. It appears that magnetic fields are
insignificant in controlling the evolution of the clouds.

We have also mapped the central regions of each of
the clouds at a wavelength of 2.2μm in order to investigate
the nature of possible embedded clusters of stars and to
compare the star formation efficiencies. Clouds for

which dynamic pressures are estimated to have the greatest

influence appear to have the highest star formation

efficiencies.

CHAPTER 1

INTRODUCTION

The first suggestion of a "medium" between the stars
was made by F. G. W. Struve (1847), who was able to deduce a
mean extinction coefficient from star counts of about one
magnitude per kiloparsec for a general absorbing medium in
our galaxy. Much later Trumpler (1930) confirmed Struve's
early results by measuring diameters of galactic clusters
and comparing these with the cluster distances. The resul-
tant apparent increase in diameter with distance was
attributed to the presence of an interstellar absorptive
medium. Further support for the existence of this medium
was soon forthcoming in Bottlinger and Schneller's (1930)
study of the distribution of Cepheids perpendicular to the
galactic plane and van de Kamp's (1932) discovery that
external galaxies appear to be concentrated near the poles
of our galaxy.

However, far from being uniform, galactic extinction
has a very anisotropic distribution, causing large areas of
the sky to be nearly devoid of stars. Herschel (1784) noted
the association of these areas with bright nebulae. The
advent of photography allowed the early twentieth century

1

astronomer H. D. Curtis (1919) to dramatically confirm the association of bright and dark nebulae. Hubble (1922) postulated that the class of bright nebulae observed to possess absorption line spectra were produced by light from nearby stars reflected by interstellar material. Hubble's work led Russell (1922) to propose that the associated dark clouds are composed of small dust particles. In some cases the total mass estimated for these clouds exceeded several solar masses. Russell was the first to suggest that dark clouds might be the birthplaces of stars. In distribution Bok (1937) showed that the dark clouds are confined to within a few degrees of the plane of the galaxy.

At nearly the same time, the interstellar medium was shown to be composed not only of dust but also of gas. Hartmann (1904) first observed constant velocity H and K lines of calcium in absorption in the spectrum of a spectroscopic binary. It was, however, left to Plaskett and Pearce (1933) to show that the radial velocities of H and K lines observed in early type stars are consistent with the view that intervening space is uniformly filled with calcium gas and that this gas rotates about the galactic center with the same velocity as the early type stars. An equally important development in understanding the role of the gaseous component of the interstellar medium was the observation of the 21 centimeter line of neutral hydrogen

(first predicted by van de Hulst (1945) from theoretical
considerations). The 21 centimeter observations show that
hydrogen maps out the spiral arms of the galaxy.

The final important component of the interstellar
medium, a magnetic field, was first suggested by Alfven in
1937 (see Kaplan and Pikelner 1970). Later this was sup-
ported by the work of Richtmeyer and Teller (1949) and
Fermi (1949) in connection with the observed motion of
cosmic rays. Today a mean value for the interstellar mag-
netic field of several times 10^{-6} Gauss is suggested by
several different methods.

Thus, by 1950 the interstellar medium was understood
to contain dust and gas closely confined to the plane of
the galaxy, much of it in the form of dark clouds of various
shapes and sizes and presumably threaded by a magnetic field.
It also became apparent that very young stars were often
associated with the most massive of the dark clouds. The
stars which Herschel (1784) first noted to be associated
with these clouds are the massive O and B stars which
possess sufficient luminosity to illuminate nearby dark
material. Today it is known that even younger objects such
as T Tauri stars. Herbig Ae and Be stars, and Herbig-Haro
objects with ages of only a few times 10^5 years are also
found near these clouds. More recently, Grasdalen, Strom,
and Strom (1973) have found a cluster of young O and B type

stars embedded in the Ophiuchus dark cloud region. The association of very young stellar objects with massive dark clouds suggests that these complexes are regions of active star formation.

During the past twenty-five years significant progress has been made in improving our physical understanding of the processes that are important in controlling the collapse of massive dark clouds and the initial stages of star formation. It is currently thought that dynamical forces may, in some cases, initiate cloud collapse, while magnetic fields may alter or significantly impede the gravitational collapse. However, the importance of magnetic fields during the star formation process is, at present, highly uncertain since (1) only upper limits to the strength of the B fields are available and (2) the structure of the fields within the dark clouds are unknown.

In this dissertation we will attempt to investigate from an observational standpoint the role of magnetic fields in the evolution of four massive ($M \geq 10^3 M_\odot$) dark cloud complexes: Rho Ophiuchi, Corona Austrina, NGC 1333, and the NGC 2068 and NGC 2071 regions of Lynds 1630 (M78). Although it is impossible with current technology to derive the magnitudes of the B fields, we may, via linear polarization measurements of stars background to these clouds, map out the magnetic field structures within the clouds.

From comparison of the magnetic field structures with the dark cloud morphologies, we hope to derive a qualitative understanding of the effects of magnetic fields on the cloud evolution. Our observational results will then be compared with the predictions of various dynamical scenarios put forth for the evolution of dark cloud complexes, namely:

1. shock-driven implosion due to a nearby supernova outburst or galactic spiral density wave shock;

2. cloud-cloud collisions;

3. mass accretion via Parker's instability; or

4. quiescent collapse.

Each of the clouds selected for study appears to be a center of active star formation. To determine the extent of star formation in these complexes and to evaluate the possible differences in star formation efficiency, we will map the centers of each of the clouds at a wavelength of 2.2μm to detect embedded stellar associations which may be forming there. These observations will also provide us with the tools to probe the magnetic field geometry within the dark cloud located near Rho Ophiuchi. The magnetic field structure deep within the cloud may be mapped by means of infrared, linear polarization measurements of stars embedded in the cloud.

In the remainder of this chapter we will review previous attempts to study the morphological properties, and the gas, dust, and magnetic field components of dark clouds. While no attempt will be made to give a complete historical survey, the material is intended to provide the reader a background useful in later chapters.

1.1 Morphological Properties of Dark Clouds

Barnard (1927) made the first extensive catalogue of dark nebulae based on his photographic survey of the Milky Way in which 349 objects were listed. Shortly after this study, Lundmark and Melotte (Lundmark 1926) searched the Franklin-Adams plates covering the entire sky and found a total of 1550 dark nebulae. Since that time many other investigators have undertaken photographic surveys of dark clouds. Among these are Khavtassi (1955), Hayden (1952), and most recently Lynds (1962) who lists 1802 condensations found on the National Geographic Society - Palomar Observatory Sky Survey (POSS).

The dark objects listed in these catalogues range from the very small "elephant trunk" structures and globules (surface areas of only a few square minutes of arc), whose importance was first pointed out by Bok and Reilly (1947), to the giant clouds which can cover tens of square degrees of the sky. The smallest globules have estimated masses as small as 0.1 $M_\odot$ and sizes of 0.01 pc, while large clouds

have masses as large as 2×10^4 M$_\odot$ and sizes of 20 pc
(excluding the truly giant complexes like Sgr B2).

In this work we will be concerned only with large
clouds with masses in excess of 1000 M$_\odot$; hereafter we will
apply the term "dark cloud" only to these objects. These
massive clouds are not spherical in shape, but quite irreg-
ular, often bordering on the chaotic in appearance. Most of
the large clouds have central regions which are totally
opaque to visible light having A$_V$'s > 15-40 magnitudes. In
some cases the entire cloud appears opaque and possesses
sharp boundaries. In other cases the edges may be very
ragged, or there may be evidence of foreground or nearby
layers of smaller obscuration. Also seen associated with
some clouds are long streamers of material extending as far
as 30-40 parsecs away from the most dense regions.

Often found near the center of the massive cloud
complexes are groups of very young stars (T Tauri and other
emission line objects). These are almost always associated
with regions of highest obscuration. Many of these clouds
have brightly illuminated reflection nebulae regions.

1.2   The Gas Component

1.2.1 Hydrogen Density

Several authors have shown that in the general
interstellar medium the ratio of neutral hydrogen 21

centimeter emission to total obscuration is approximately

constant for even large values of total obscuration. (See,

for example, Lilley 1955.) However, for dark cloud regions

this relation does not hold, as there is little contribution

to the 21 cm emission from the cloud material, even though

the total obscuration may be very large ($1 \leq A_v \leq 30$). If

it is assumed that the gas to dust ratio in high density

dark clouds is the same as for the general interstellar

medium, then it must be true that either hydrogen is not

present in the clouds, or, more likely, that it is in the

molecular form (H_2). Unfortunately, H_2 has not yet been

observed directly in dark clouds, since all of its spectral

lines originating from the ground state are located in the

ultraviolet. Thus, indirect methods must be employed to

estimate the total hydrogen density.

One method is to combine radio and optical data by

estimating a dust to gas ratio for the cloud, estimating

the extinction, assuming a distance to the cloud, and

assuming a shape for the cloud. This method is rather

uncertain in that (1) the dust to gas ratio may not be the

same for the cloud as for interstellar space, (2) the

extinction is particularly difficult to estimate in dark

regions where few stars are available for star counts,

(3) distances to clouds are uncertain, and (4) the geometry

must be assumed (usually sphericity). From this method one

finds that typically $10^3 < (n_H + n_{H_2}) < 10^4$ (cm^{-3}). This high density is confirmed by several other methods, including (1) using the virial theorem in conjunction with line width as measures of the turbulence and then estimating the density required for stability, (2) comparing radiative de-excitation with collisional excitation rates for observed transitions of different molecules, and (3) measuring CO densities and assuming a cosmic abundance ratio of C/H. It is, indeed, encouraging that all of these methods yield estimates in the range $10^3 < (n_H + n_{H_2}) < 10^4$.

1.2.2 Other Molecules, Temperatures, and Heating and Cooling

The fact that H_2 is prevalent in dark clouds implies low excitation conditions. This suggests that the clouds are likely places to search for other molecules at radio wavelengths. In fact, OH, H_2CO, and CO are all commonly found; and CS, CH, and NH_3 are occasionally found in dark clouds. Zuckerman and Palmer (1974) give a comprehensive review of the detection of radio line emission from interstellar molecules. Observations of molecules are important because they reveal important information about temperatures, motions, internal radiation fields, and, as we have already seen, densities in dark clouds that otherwise would be impossible to obtain.

The kinetic temperature of a gas (assumed in thermal
equilibrium) is determined by the condition that the total
kinetic energy lost per unit time and volume equals that
gained per unit time and volume:

$$\frac{d}{dt} \left(\frac{3}{2} nkT_K\right) = \frac{5}{2} kT_K \frac{dn}{dt} \qquad (1.1)$$

where n = total density of free particles. The kinetic
temperature may be estimated under high density conditions
where the rate of spontaneous decay of a line is smaller
than that of the collision rate for a given line (the con-
dition of thermalization). Under these conditions the
kinetic temperature is approximately the observed excitation
temperature of the line. Penzias et al. (1972) have shown
that the $J = 0 \rightarrow 1$ transition of CO is likely thermalized, and
have derived a typical temperature of $T_K = 6°K$ for dark
cloud regions. Temperature measurements of other molecules
(OH, Heiles 1969; and NH_3, Cheung et al. 1973) yield a
similar value.

The heating of interstellar gas by ionization of
neutral atoms can be due to several processes, including:
ultraviolet radiation, cosmic rays, interstellar currents,
viscously damped gas motions, collisions of clouds, and
shock waves from novae and supernovae. Cooling is due to
inelastic collisions between atoms and electrons. In dark
clouds where gas and dust densities are high, the primary

mechanisms of heating and cooling are ionization by UV
radiation from embedded stars and collision excitation of
C, Fe, and O followed by radiative decay.

The dense dust associated with dark clouds makes
heating of the gas by UV radiation extremely difficult;
· hence molecules with low photodisassociation energies can
survive due to the paucity of UV radiation in·dark clouds
not having embedded stars. Recent work by Encrenaz,
Falgarone, and Lucas (1975) shows that the CO to dust ratio
for the Rho Ophiuchi dark cloud is constant for $2 < A_V < 6$
but is smaller for $A_V < 2$, indicating that UV photodis-
association is effective for only the outermost 2 magnitudes
of absorption. However, Grasdalen et al. (1973) have found
a dense association of OB stars buried at the center of this
cloud, thus providing an intense source of UV radiation
which may significantly affect the ionization and molecular
equilibrium conditions thought appropriate for interiors of
dense dark clouds.

Mapping of the extent and radial velocity structures
of dark clouds can most conveniently be carried out by ob-
serving several well chosen molecules: most notably CO
(see, for example, Dickman 1975 and Milman et al. 1975) and
CH (see, for example, Hjalmarson et al. 1975). From these
observations one can obtain information about radial
velocity gradients across the face of the clouds and radial

velocity dispersions at particular points. For dark clouds radial velocity differences of 1-4 km/s and velocity dispersions of 0.5 km/s are typical. Large scale gas motions can be studied in this manner. Zuckerman and Palmer (1974) provide a good review of this subject.

1.3 The Dust Component

1.3.1 Composition and Size of Grains

Trumpler (1930) was able to demonstrate that interstellar extinction is accompanied by apparent reddening. This results from the fact that the interstellar extinction mechanism is more effective at shorter wavelengths, thus selectively absorbing or reddening star light. Hall (1937) and Stebbins, Huffer, and Whitford (1940) first showed that the "reddening curve" followed roughly a λ^{-1} law in the visible light wavelength region. Since that time it has been found that the reddening curve is modified in the infrared and ultraviolet wavelength regions by various extinction features. A one-component model of the grains is apparently unable to explain all of the observed features. Current fits to the observed extinction require an admixture of grain sizes, typically 0.1μ, with silicate and graphite constituting the majority of the grain mass, and with traces of iron oxides, silicon carbide and other compounds. These

models, though giving a good fit to the extinction curve, may not be unique.

An extinction feature that may have particular importance for dark clouds are the diffuse absorption bands. Thirty-nine of these bands have thus far been identified between 4400 Å and 6850 Å (Herbig 1975). The strength of these lines generally correlates quite well with the total extinction. This suggests that the bands are related to the grains in some way. It is generally thought that the lines are due to as yet unidentified molecular carriers on the surface of the grains. The surfaces of grains are, in fact, excellent places for molecules to form, especially in the dark cloud environment. However, Snow and Cohen (1974) have shown that the band strengths per magnitude of redden-ing seem to decrease in the interiors of dark clouds. This suggests that either the carriers responsible for the lines are not as abundant in the cloud interiors, or that the lines originate in small grains which are coated by mantles in the central regions where grains are thought to be larger than normal in size.

Evidence that grain sizes may be considerably larger in dark cloud environments than for the general interstellar medium came from observations of R, the ratio of total to selective absorption: $R = A_v/E_{(B-V)}$. The value of R is thought to be proportional to the size of the particles

responsible for absorption. Johnson (1968) noted that values of R larger than 3.3, which is typical of the general interstellar medium, seem to occur under very localized conditions, most notably near young clusters and diffuse nebulae. More recently Carrasco, Strom, and Strom (1973) have shown R to be larger than normal for the dark cloud complex located near Rho Ophiuchi on the basis of the color excess ratios E_{V-K}/E_{B-V}. This, plus the fact that this cloud has a flattened ultraviolet extinction curve (Bless and Savage 1972), lead these authors to conclude that particle sizes are larger than normal.

1.3.2 Grain Temperatures

Knowledge of the temperature of grains in dark cloud interiors is important to an understanding of the molecular processes at the grain surfaces and of the formation of mantles on the grains. For the densities characteristic of cloud interiors, the temperature of the grains is controlled solely by heating from radiation absorption and cooling by thermal reradiation. (Collisions with gas are important only for a few very dense clouds.) Grain temperatures estimated for the general interstellar medium are typically 10-20°K, whereas for dark cloud regions they have only cooled to about 5-10°K. This is principally due to poor infrared emissivity of the grains which results from their small size; typically the grains are smaller than the

wavelength of a significant percentage of the emission of a blackbody at 5-10°K. If the grains are larger than normal in dark cloud interiors, this could lead to somewhat greater cooling. However, the grains would be considerably hotter if radiation fields of young embedded clusters are found present.

1.3.3 Polarization and Grain Alignment

The polarization of starlight due to foreground interstellar material was discovered by Hall (1949) and Hiltner (1949). The polarization of starlight may be defined in magnitudes as

$$p = 2.5 \log (I_{max}/I_{min}) \qquad (1.2)$$

where I_{max} and I_{min} are the maximum and minimum intensities of the starlight observed while rotating a linear polarizing analyzer in the light beam; or, alternately, in terms of the degree of polarization by

$$P = (I_{max} - I_{min})/(I_{max} + I_{min}). \qquad (1.3)$$

It was soon recognized that the correlation between the polarization and the reddening of stars,

$$\frac{p}{A_v} \lesssim .065, \qquad (1.4)$$

meant that the polarization was due to interstellar grains. The grains appear to be aligned so that the radiation is

most heavily absorbed when the electric vector is in the direction of maximum extinction efficiency.

Although many mechanisms have been proposed to explain the grain alignment, the best fit to the observations is from that of Davis and Greenstein (1951). The Davis-Greenstein (hereinafter referred to as D-G) alignment mechanism demands the existence of paramagnetic or ferromagnetic dust grains aligned by a magnetic field due to torque being applied to the grain by paramagnetic absorption. This torque opposes the rotation of the grains on an axis perpendicular to that of the magnetic field. The degree to which grains can be aligned by the D-G mechanism depends on several parameters, including: the paramagnetic properties of the grains, grain size, grain temperature, surrounding gas temperature, index of refraction, and the strength of the magnetic field. Calculations by Purcell and Spitzer (1971) show that to reproduce interstellar polarization by the D-G mechanism acting upon elongated grains typical of those in the interstellar medium requires a magnetic field of $B \simeq 10^{-5}$ Gauss. This is almost a factor of 10 larger than the B values typically observed in the interstellar medium (see next section). However, this difficulty could be overcome if the particles have special paramagnetic or additional ferromagnetic properties. Other, more exotic alignment mechanisms have been proposed (for instance,

Harwit 1970, Wickramasinghe 1970, Martin 1971, and Gold 1952); however, these all suffer from major defects.

Greenberg (1968) has shown that the wavelength of maximum polarization, λ_{max}, is proportional to the product $(m-1)r$, where m is the index of refraction and r is the radius of the grain. Serkowski (1973) has shown correlations between λ_{max} and various extinction ratios, a result which is not surprising since grains are responsible for both extinction and polarization. Furthermore, since R is an indicator of particle size, we expect a correlation between R and λ_{max}. Serkowski, Mathewson, and Ford (1975) have empirically demonstrated that

$$R = 5.5 \; \lambda_{max}, \qquad\qquad (1.5)$$

and indicate that λ_{max} may be the best indicator for finding local deviations of R.

We have already discussed the fact that in dark cloud complexes the value of R seems to be larger than normal. Carrasco et al. (1973) have indeed found larger than normal values of λ_{max} in the Ophiuchus dark cloud. The values of λ_{max} found there are consistent with the values of R, thus indicating that in fact grain sizes are larger than normal in dark clouds.

1.4   The Magnetic Field Component

1.4.1   Field Strengths

Several different methods have been employed to measure the strength of the galactic magnetic field. The most straightforward method is to measure the Zeeman splitting of the $\lambda = 21$ cm line of neutral hydrogen. The strong narrow absorption components are observed in front of a bright background source. This method has yielded upper limits to the general galactic magnetic field of $B \simeq (5-10) \times 10^{-6}$ Gauss.

A second method involves the measurement of the Faraday rotation by the galactic B field of the plane of polarization of extragalactic radio sources. The mean galactic B field determined from this method is 3×10^{-6} Gauss, in good agreement with the Zeeman splitting measurements.

Finally, the galactic B field strength may be estimated from measurement of the brightness temperature of synchrotron radiation within our galaxy. This method gives $B \simeq 3 \times 10^{-5}$ Gauss, a factor of 10 larger than the other methods. This discrepancy is not clearly understood at present. Reviews of the techniques and results of galactic field measurements may be found in van de Hulst (1967), Spitzer (1968), Veschur (1970), and Rees and Reinhart (1972).

The strength of B fields may be greatly enhanced under the high density conditions in the internal regions of dark clouds, if the fields are "frozen in" to the gas. This is especially true if the cloud interiors have the high degree of ionization required by embedded star clusters. Large values of the B fields (as high as several times 10^{-4} Gauss) appear necessary to provide the grain alignment observed in the Rho Ophiuchi cloud by Carrasco et al. (1973) under the high density and large grain size conditions found there.

Attempts, however, to measure these predicted strong magnetic fields have thus far proven unsuccessful. Since little neutral hydrogen is found in dark clouds, the Zeeman splitting of other molecules (principally OH) must be used. Crutcher et al. (1975) have set an upper limit of 5×10^{-5} Gauss for the 4C and Taurus dark clouds from OH Zeeman splitting. It is quite possible that these clouds are old and that the B fields which were frozen in during collapse have since separated from the cloud material.

Chaisson (1975), however, has set an upper limit of $B \leq 5 \times 10^{-4}$ Gauss for the central region of the Rho Ophiuchi dark cloud. This limit is in agreement with the field required to produce the polarization observed in that cloud and is consistent with the expected strength of the field frozen into the cloud during collapse under high density

and ionization conditions. The magnetic field in this cloud
could be considerably stronger since the observed Zeeman
splitting could be reduced by a twisted field which reverses
itself along the line of sight. Magnetic field measurements
in other dark clouds give upper limit results similar to
those in Taurus and Ophiuchus above.

1.4.2 Structure of Magnetic Fields

If elongated grains are, indeed, aligned by the D-G
mechanism, they will be forced to spin with their major axes
perpendicular to the direction of the B field, provided that
the temperature of the grains is less than that of the
surrounding gas. (The validity of this condition for the
dark clouds we will observe in this dissertation will be
discussed in the next chapter). For particles of the size
of or smaller than the wavelength of light, extinction will
primarily be due to absorption so that extinction will be
larger in the direction of the grains' major axes. Thus, if
we look across a B field aligning elongated grains, we
notice that the direction of electric vector maximum is the
same as that of the B field. However, if we look directly
down a field line, we find that there is no net polarization.

This property of grain alignment is a powerful tool
in mapping the transverse component of the galactic B field.
Mathewson and Ford (1970) have reported the polarization
and position angle of the electric vector for approximately

7000 stars. This work has revealed many features of the local magnetic field. Local interstellar polarization seems to be produced within a distance of about 400 pc from the sun. The polarizations seem ordered and parallel to the galactic plane at galactic longitude $l^{II} = 140°$ and $l^{II} = 320°$ and rather chaotic at galactic longitudes $l^{II} = 50°$ and $l^{II} = 230°$. This pattern is generally attributed to a local helical B field or a longitudinal field plus a series of supernovae in the local neighborhood.

Until the present time virtually no work has been done in mapping magnetic field structure in individual dark clouds or features of dark clouds by measurement of polarization of background stars. Shain (1955), however, has noted for several dark clouds a tendency for the B field to lie parallel to elongated features protruding from the clouds. It will be a major task of this dissertation to map out in detail the magnetic field structure of several dark cloud complexes via this method in order to better understand their role in cloud collapse.

CHAPTER 2

OBSERVATIONAL METHODS AND CLOUD SELECTION

The discussion of Chapter 1 has provided the
motivation for this work. Our purpose will be to under-
stand, from an observational point of view, the role of
magnetic fields in these respects: (1) in the overall
collapse of massive dark clouds, (2) in determining the
likely sites of star formation in those clouds, and (3) in
the fragmentation processes and star formation efficiency.
In this chapter we will discuss the observations necessary
to obtain the information we require and will select
several candidate clouds for detailed study.

2.1 Observational Methods

In order to carry out our aims it is clear that we
need to gather information about magnetic fields and stellar
populations within the dark clouds.

2.1.1 Stellar Populations of Dark Clouds

Photographs of dark cloud regions often reveal a
number of young stellar or proto-stellar objects (such as
Hα stars, Herbig Ae and Be stars, and Orion population
variables) located along the foreground edge of the cloud.

While it is reasonable to believe that these visible objects are characteristic of the young stellar population recently formed within the cloud, it is not likely that they are the only young objects associated with that cloud. If these objects occur at the periphery of dark clouds, others at the far side of the cloud will be hidden by many magnitudes of visual absorption, while still others may be hidden within the dark cloud itself. Indeed, there is evidence that such hidden objects exist, since bright optical patches and certain Herbig-Haro objects are likely no more than reflection nebulae illuminated by obscured stellar objects (cf. Strom, Grasdalen, and Strom 1974). If we are to understand the nature and spatial distribution of newly formed stars in dark nebulae, it is clear that an attempt to discover possible embedded sources must be made.

If the light from embedded stars is attenuated by 5 to 40 magnitudes of visual absorption, as can be expected if they are embedded in a large dark cloud, the peak of their energy distribution as observed from the earth will fall in the near infrared region. For this reason we will map the interior regions of several dark clouds at a wavelength of 2.2μm (the standard K filter) which falls near the peak of the reddened spectral energy distribution for most of these stars. The choice of this filter has two other advantages. First, it is at a wavelength short

enough to be relatively insensitive to noise from the sky often found at longer wavelengths and it allows the mapping to be carried out through thin layers of cirrus clouds. Secondly, it is at a wavelength long enough that daytime sky background noise is low and thus it allows the mapping to be carried out night and day. Mapping at this wavelength has already proven itself to be an efficient method of discovering embedded stars in dark clouds. Grasdalen et al. (1973) report the discovery of over 40 point sources brighter than K = 9.0 mag while mapping a small region of the Ophiuchus dark cloud complex.

Two technological advances at Kitt Peak National Observatory (K.P.N.O.) have enabled us to carry out the 2.2μm observations using a moderate size telescope. The first involved the implementation of an InSb detector system developed by Dr. Richard Joyce at K.P.N.O. This system allows observations with a signal to noise ratio of 3 for stars of K = 12.0 mag to be made in 100 s of integration time on the 1.3 m telescope of K.P.N.O. When this system is mounted on the 1.3 m telescope (as it was for this survey), it is typically operated with the telescope secondary mirror articulated between two positions on the sky and the signal recovered by a lock-in amplifier. Figure 2.1 schematically shows the detector-telescope system.
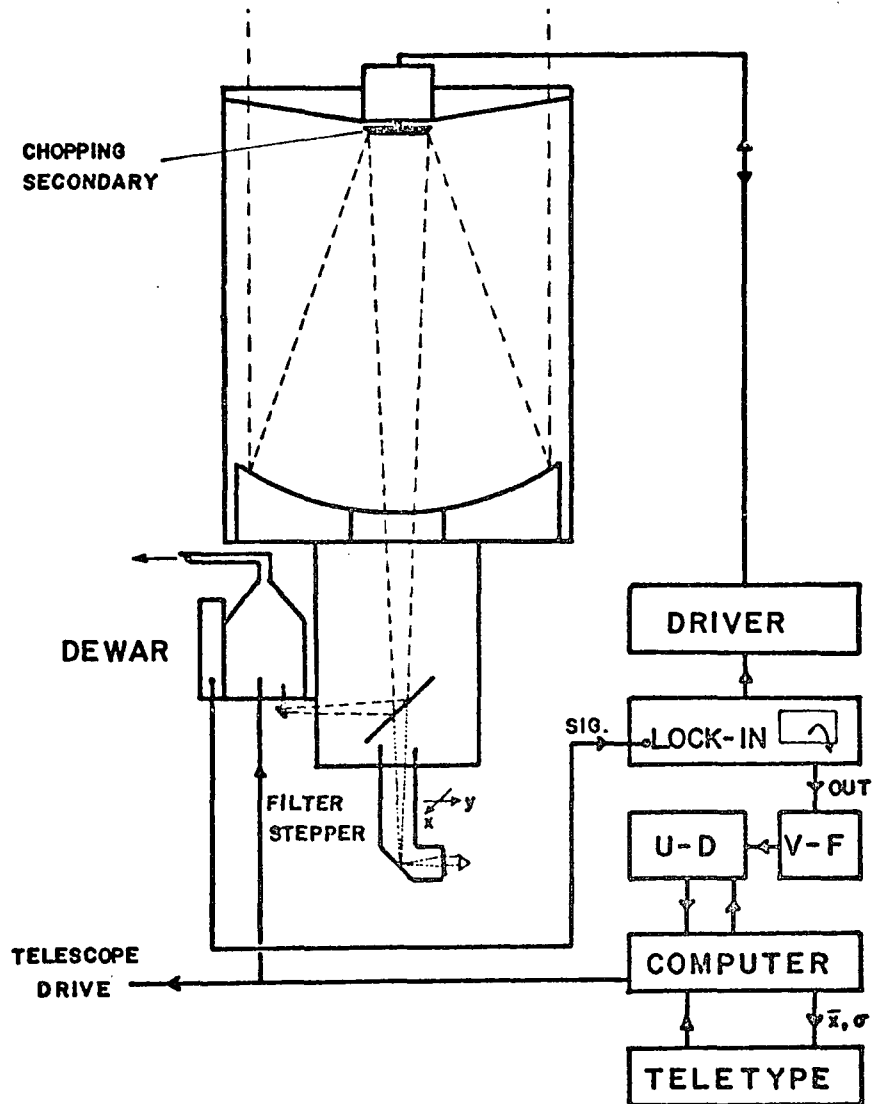
Figure 2.1. Schematic diagram of the detector-
telescope system used to obtain
the 2.2μm dark cloud maps.

The second advance was provided by the adaptation by William Brown of K.P.N.O. of a Varian 620f computer to control telescope motions and to allow real-time presentation of the measured signal strength and an estimate of the measurement accuracy. To map a selected region, we first choose a nearby, bright offset star. A computer instruction then commands the telescope to move from this star to a preselected map center. Next, the telescope, under computer control, executes a series of motions which trace out a grid pattern on the sky. Integrations of a preselected length are carried out at each point in the grid pattern. A series of computer commands then return the telescope to the offset star position, so that the observer can correct for small errors, if any, in the telescope guide rate.

2.1.2 Magnetic Field Measurements

Earlier we outlined several methods to obtain magnetic field strengths, each of which, unfortunately, have drawbacks which make them unacceptable for measuring magnetic fields in dark clouds as we desire. Neutral hydrogen is not abundant in dark clouds and the attempts at measuring Zeeman splitting of various molecules have thus far proven highly unsuccessful, and in any case these methods are limited to restricted regions of certain clouds which contain these molecules. Finally, measurements of the Faraday rotation of extra-galactic radio sources requires that such

a source be positioned directly behind a cloud and only provides information at one position of the cloud. At present there appears to be no way to directly map magnetic field strength in dark clouds.

We can, however, map the magnetic field geometry in the dark clouds by measurement of the linear polarization of background stars whose light is observed through the periphery of the dark cloud material.

As mentioned in the previous chapter, the D-G mechanism (paramagnetic relaxation) seems to offer the best explanation of alignment of grains in interstellar polarization. (Other mechanisms, such as radiation pressure and gas flow relative to the dust grains may play a part in the alignment of grains in the dark cloud environment, but the polarization patterns due to these should be easily recognizable.) Jones and Spitzer (1967) have reconsidered the D-G mechanism and shown that the degree of alignment, F, of prolate spheroid grains is proportional to the magnetic field, grain temperature (T_{gr}), and surrounding gas kinetic temperature (T_{gas}) in the following manner

$$F \propto B^2 \, (T_{gas}^{-1/2}) \, (1 - T_{gr}/T_{gas}).$$
(2.1)

If $T_{gas} > T_{grain}$, F is positive and the alignment is in the normal D-G sense. That is, the spin axis of the grains will be the short axis and it will be parallel to the direction

of the magnetic field. Thus, the linear polarization will
be in the direction of the magnetic field. If T_{gas} = T_{grain}
there will be no alignment. Finally, if T_{gas} < T_{grain}, the
alignment will be in the opposite sense and the polarization
direction will be perpendicular to that of the magnetic
field.

The stars accessible to observations of optical
polarization are found at the periphery of the clouds where
A_V ≃ 2-8, that is, grains neither , the clouds' centers
nor in the interstellar medium. What, then, is the ratio
of gas to dust temperature in these regions?

In the interstellar medium the grain temperatures
are controlled solely by the interstellar radiation field
which can be approximated by a Planck function at 10^4 °K,
diluted by a factor W equal to 10^{-14} (Spitzer 1968), and
the temperature of the grains is given by

$$T_{grain} = 10^4 \cdot W^{1/5} \simeq 16°K. \qquad (2.2)$$

The interstellar gas temperature is much higher than this
and T_{grain}/T_{gas} << 1.

Goldreich and Kwan (1974) have shown that for gas
densities of $n_H \lesssim 2 \times 10^4$ cm^{-3}, collisions of grains with
the gas do not make an important contribution to the thermal
equilibrium of the grains in molecular clouds. The grains'
temperature is thus controlled solely by the radiation field

of any stars embedded in the dark clouds. Radio observa-
tions to be presented in a later chapter show that the
central densities of all but one of the clouds we will
observe are less than 2×10^4 cm^{-3}. At the outer fringes
of the clouds the densities must be much less than this and
we can assume that the grain temperatures are controlled by
the central radiation field. With this assumption Goldreich
and Kwan (1974) show that the grain temperatures are given
by

$$T_{grain} = \frac{24}{[r(pc)]^{2/5}} \left[\frac{L}{10^6 L_\odot} \right]^{1/5} {}^\circ K \qquad (2.3)$$

where r is the distance to the grains and L is the lumi-
nosity of the central stars. In table 2.1 we give in suc-
cession the cloud name, the typical gas kinetic temperature
given by various observers listed in the table footnotes,
the distance to the grains, the central luminosity of
embedded stars, the computed temperatures of the grains
using equation (2.3), and the ratio of grain to gas tempera-
tures. In these calculations the distance to the grains is
the distance from the center of the cloud to a typical path
through which we observe background stars. The central
luminosities in column 4 are based on the embedded source
discoveries of the next chapter, corrected for the undis-
covered faint end of the assumed cluster luminosity func-
tions. In order to place an extreme upper limit on the

Table 2.1. Ratio of dust to gas kinetic temperatures at the
peripheries of dark clouds observed

Cloud Name	T_{gas} (°K)	R (pc)	Central Lum($L_\odot$)	T_{grain} (°K)	T_{gr}/T_{gas}
NGC 133	20^a	0.75	1820	7.6	.38
Corona Austrina	20^b	1.3	190	3.9	.20
Lynds 1630	25^c	11	5390	3.2	.13
Ophiuchus	25^d	3.5	5150	5.1	.20

a. Lada et al. (1974)

b. Loren (1975)

c. Milman et al. (1975)

d. Encrenaz et al. (1975)

grain temperatures, we have assumed each embedded source has a luminosity of 10 $L_\odot$. From the last column we see that in each case $T_{grain}/T_{gas} < 1$. This inequality will remain true for path lengths we chose farther from the clouds' centers as the grains' temperatures become more influenced by the interstellar radiation field and slowly warm to about 16°K. Thus, we may assume that the polarization orientations will be in the same direction as the magnetic fields.

The instrument chosen to make the polarization measurements is a computer-controlled photometer-polarimeter developed by Dr. T. D. Kinman and C. T. Mahaffey of K.P.N.O. This system employs a rotating filter wheel system which, when equipped with a linear polarizer, can be used for polarimetric measurements. Two features of the system allow it to be a fully remote-controlled device when operated at a large telescope, such as the K.P.N.O. 4 m or 2.1 m telescope. The first is a television guider system which allows that the stars we are interested in observing be quickly obtained. The second is the use of a Varian 620f on-line computer, which controls the movement of the filter wheel and provides for real-time data reduction. An interactive control box additionally allows the program variables (integration times, number of times through the filter wheel sequence, etc.) to be changed easily. These features of the system are very attractive to our program, since it requires

many real-time observer decisions and program variations.
Figure 2.2 shows the layout of the TV aquisition system,
photometer, and photomultiplier cold box. A more detailed
description of this system is given by Kinman and Mahaffey
(1974).

2.2   Selection of Clouds Observed

2.2.1   Criteria for Cloud Selection

We require that two criteria be met by the massive
dark clouds we choose for our observations. The first of
these is that the clouds should be as free as possible from
the effects of the intervening interstellar medium. This
requires that the clouds be both nearby and well removed
from the galactic plane. From the standpoint of our mag-
netic field mapping this requirement will reduce the effects
of interstellar polarization of foreground material and the
number of unpolarized foreground interloper stars. It is
even more critical to the infrared mapping program where
proximity will allow us to reach to the fainter end of the
luminosity function of any embedded stellar cluster we may
find, probe more deeply the cloud interior regions, and, of
course, reduce the effects of foreground reddening.

The second criteria is that we require some evidence
that the clouds have recently undergone an episode of star
formation. Although many extremely young dark clouds may be
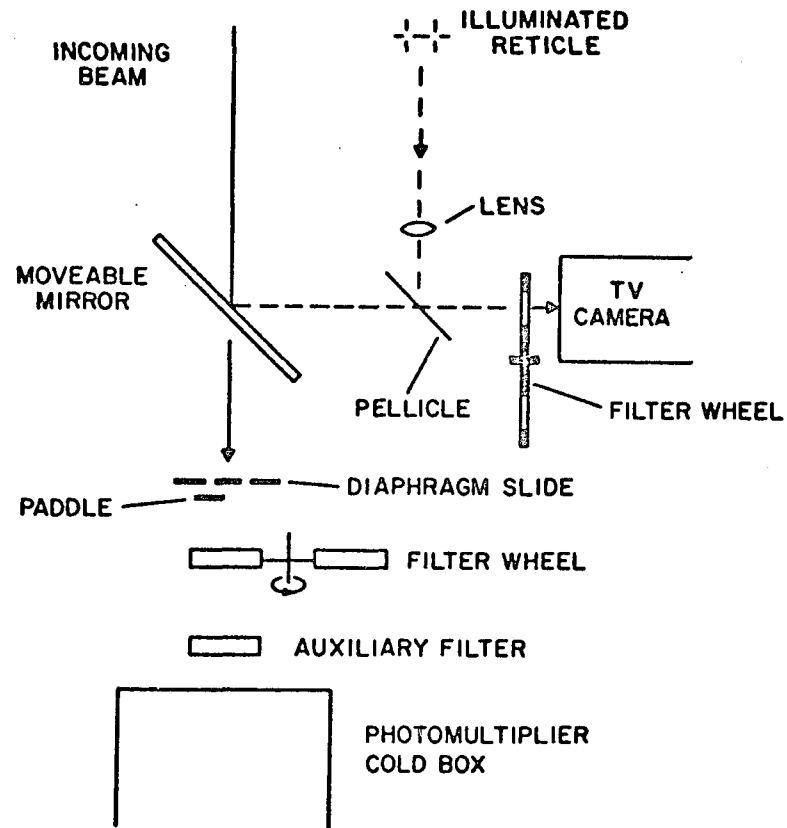
Figure 2.2. Layout of the TV system, photometer, and Kinman photometer-polarimeter.

This system was used to obtain the visual polarization observations.

forming stars and yet show no surface manifestations for it, such evidence will greatly enhance our chances for discovering places where very significant star formation is occurring.

2.2.2 The Dark Clouds Selected

Here we present a brief outline of pertinent background data on each of the four clouds we have selected to investigate.

Rho Ophiuchi Dark Cloud. The large dark cloud complex located near Rho Ophiuchi and centered at $\alpha(1950) = 16^h 22^m$, $\delta(1950) = -24° 21'$ (galactic coordinates $l^{II} = 354°$, $b^{II} = +16°$) seems particularly well suited for our study. Bok and Cordwell (1973) derive an estimated distance of 200 pc from star counts. Garrison (1967) has studied the B stars in the Upper Scorpius complex associated with the dark cloud and estimates a distance of 165 ± 15 pc, while Blaauw (1964) uses the moving cluster method to find d = 170 pc.

There is considerable evidence for recent star formation in the form of a substantial number of early type stars and Hα emission objects embedded in the cloud (Struve and Rudkjøbing 1949, Haro 1949, Dolidze and Arakelyan 1959). More recently Grasdalen et al. (1973) have found over 40 embedded 2.2μm point sources located near HD 147889.

Information regarding the dust content of this cloud is provided by Carrasco et al. (1973), which will prove invaluable in our later discussion of the magnetic field strength in the cloud.

M78: A Region of the Dark Cloud Lynds 1630. M78 (NGC 2068, 2071) is a region of the dark cloud Lynds 1630 centered near $\alpha(1950) = 05^h \, 43^m$ and $\delta(1950) = -01°$ (galactic coordinates $l^{II} = 206°$, $b^{II} = -15°$). This cloud is associated with the Orion OB complex, and thus is at a distance of approximately 500 pc. The entire Orion OB association region is thought to be a region of active star formation since signposts of recent star forming events are abundant: the presence of several dense molecular clouds (Gately et al. 1974; Werner et al. 1974; Tucker, Kutner, and Thaddeus 1973; and Loren, Vanden Bout, and Davis 1973), a Herbig Ae and Be star (V 380 Orionis), and several Hα emission objects (Haro 1953).

In particular, Lynds 1630 seems to be the center of a large CO complex which has within it several CO hotspots centered on NGC 2068; these hotspots are thought to be associated with embedded stars (Milman et al. 1975). The cloud also contains a number of Hα emission stars (Herbig and Kuhi 1963) and irregular variables (Fedorovich 1960, Rosino 1960). Furthermore, a number of Herbig-Haro objects have been discovered in the area 15' south of NGC 2068

(Herbig 1974). Finally, Johansson et al. (1974) have noted the presence of a type I OH maser in the Lynds 1630 complex. This may represent yet another center of active star formation within the complex.

Zellner (1970) and Coyne, Gehrels, and Serkowski (1974) have carried out limited polarization studies of the NGC 2068 area.

Corona Austrina Dark Cloud. The large dark cloud surrounding R Corona Austrina and associated reflection nebula NGC 6729 is centered near $\alpha(1950) = 18^h 59^m$ and $\delta(1950) = -37° 01'$ (galactic coordinates $l^{II} = 0°$, $b^{II} = -18°$). The distance to the cloud is estimated at 150 pc by Gaposchkin and Greenstein (1936) on the basis of star counts. In addition irregular variable TY CrA illuminates the reflection nebula NGC 6726. R, S, and T CrA are Orion population variables and are similar to the extremely young Herbig Ae and Be stars. Several other irregular variables have also been discovered in the vicinity of this group (Hardy and Mendoza 1968). Infrared and optical observations by Knacke et al. (1973) suggest that these stars are less than 10^6 years old. A number of Herbig-Haro objects are known in this area, at least one of which is thought to be illuminated by an embedded point source (Strom, Strom, and Grasdalen 1974; Vrba, Strom, and Strom 1975). Serkowski

(1969) has obtained polarimetric information for several stars near R and T CrA.

NGC 1333. The star BD +30° 549 and an anomalous early type star illuminate the reflection nebula NGC 1333 and are located at approximately $\alpha(1950) = 03^h 26^m$ and $\delta(1950) = +31° 15'$ (galactic coordinates $l^{II} = 159°$, $b^{II} = -20°$). This dark cloud is associated with the Perseus OB2 dust cloud complex (Sancisi et al. 1974). The distance to the cloud has been estimated by Strom, Grasdalen, and Strom (1974) at 500 pc from photometric and spectroscopic observations of BD +30° 549. Several T Tauri and Hα emission stars have been found by Herbig and Rao (1972), while Herbig (1974) has identified a number of Herbig-Haro objects in the vicinity of NGC 1333. An embedded infrared source was found by Strom, Grasdalen, and Strom (1974) near one of the Herbig-Haro objects.

NGC 1333 appears to be the center of a large molecular cloud with identified lines of NH_3, CO, CS, HCN, and H_2CO (Lada et al. 1974), CH (Rydbeck et al. 1975), and OH (Sancisi et al. 1974).

CHAPTER 3

INFRARED MAPPING OBSERVATIONS

The results of the infrared mapping program are presented in this chapter. Additional infrared photometry is included in order to better understand the nature of the sources discovered.

3.1 Rho Ophiuchi Dark Cloud

3.1.1 Observations

The infrared maps obtained for the central region of the Rho Ophiuchi dark cloud were carried out using the technique of section 2.1.1 on the 1.3 meter telescope of K.P.N.O. For a large fraction of the mapped area reported here, the dwell time per grid point was set equal to 16 s; hence, sources brighter than K = 10.0 can be detected at the 4 sigma level. A beam size of 36" and a chopping throw of 38" were typically used; the grid spacing was set equal to 30". The approximate area covered in our survey is indicated by the rectangle inscribed in figure 3.1, a reproduction of the POSS red prints of the Ophiuchus region. We have also indicated in this figure the location of all

Figure 3.1. A plot of the sources observed in the course of the 2μm
            survey of the Ophiuchus cloud.

            Those sources denoted by an "O" were discovered in a
            previous survey by Grasdalen et al. (1973). Those
            plotted with a "+" represent newly discovered sources
            for which colors were obtained; an "x" denotes a new
            source measured only at 2.2μm. The source labeled "A,
            NH₃" is an apparently extended source coincident with
            the NH₃ (1.1) emission peak found by Morris et al.
            (1973). The "Z" symbols represent the locations of
            the 350μm emission peaks observed by Simon et al. (1973).
            The underlying photograph is the POSS red plate. North
            is to the top and east to the left; the scale can be
            estimated from the long dimension of the inscribed
            rectangle (36'). The bright star associated with the
            nebulosity is HD 147889.
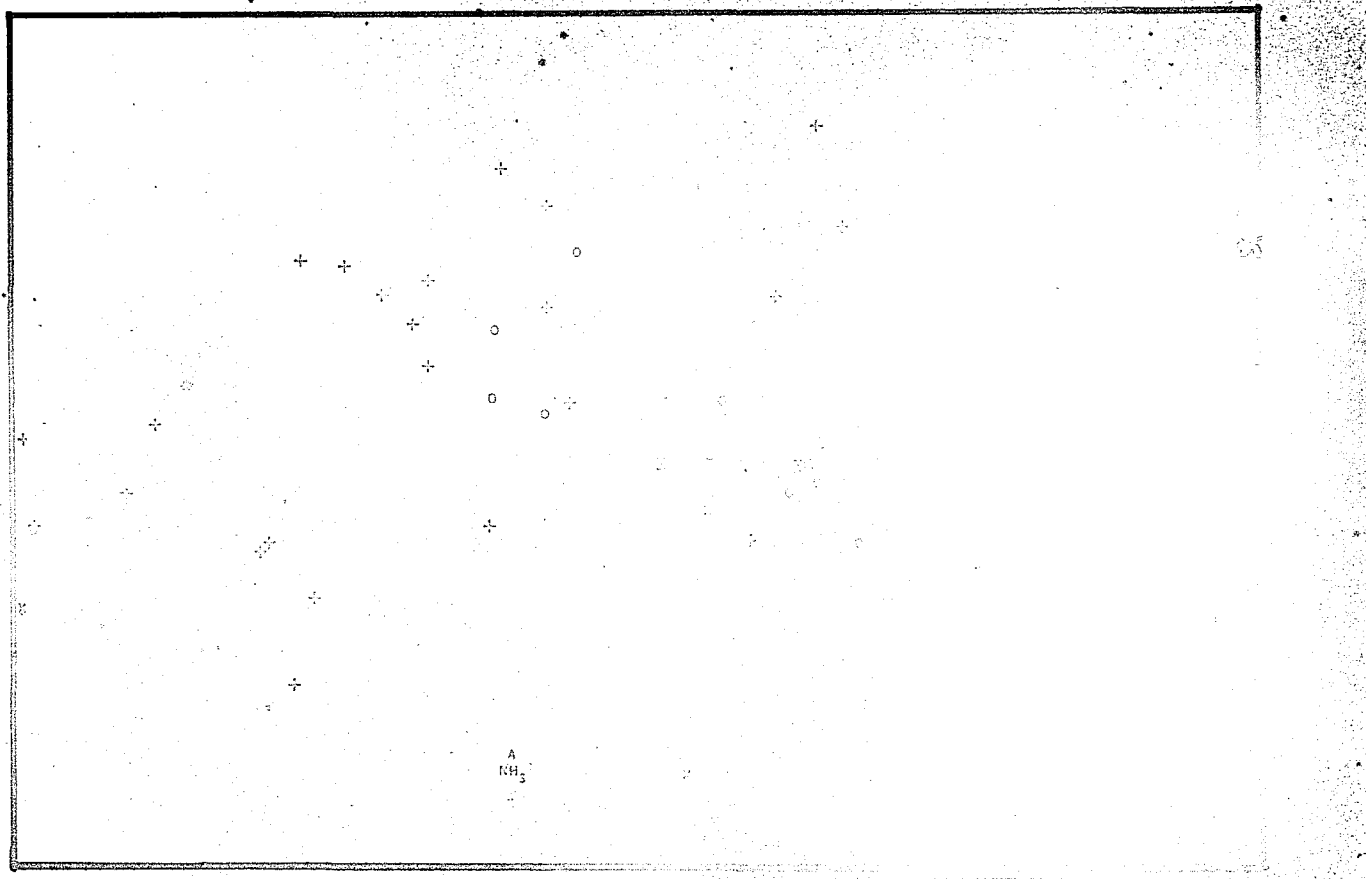
Figure 3.1.   A plot of the sources observed in the course of the 2μm survey of the Ophiuchus cloud.

sources found in this survey along with those found previously by Grasdalen et al. (1973).

In table 3.1, we list a source number, the epoch 1950 positions, the observed magnitudes at $J(1.2\mu m)$, $H(1.6\mu m)$, $K(2.2\mu m)$, and $L(3.5\mu m)$, and an indication of whether the infrared source is apparently associated with a visible star. Sources found in the current survey will be designated by a "VS" number, while those found previously by Grasdalen et al. (1973) are noted by an "S".

In table 3.2 we present the results of longer wavelength photometry carried out for a selected number of sources. These observations were made with a germanium bolometer used at the 1.3 meter telescope.

3.1.2 The Nature of the Observed Sources

We have attempted to estimate visual extinction values for all sources observed in the region mapped. These values were computed under the following assumptions:

1. The infrared color indices are all zero; implicitly this means assuming that stars are earlier than about type F0 and have no intrinsic infrared excesses.

2. The "standard" reddening curve (van de Hulst No. 15) as tabulated by Johnson (1968) provides a proper description of the long wavelength reddening in the Ophiuchus cloud; specifically we compute A_v as

Table 3.1. Infrared photometry of the 2µm sources in Ophiuchus discovered in
this survey

VS No.	α(1950)	δ(1950)	Associated with visible star?	J (1.2µm)	H (1.6µm)	K (2.2µm)	L (3.5µm)	A_v	K_o
1	$16^h23^m16^s.7$	$-24°21'29''$		$11^m.93$	$9^m.86$	$8^m.19$	^{m}	22	0.34
2*	16 23 40.7	-24 13 44		10.52	8.66	7.90		10	0.88
3	16 23 47.0	-24 13 24		11.72	9.59	8.70		12	1.52
4	16 23 36.7	-24 16 22			12.30	10.54		23	2.27
5	16 23 52.0	-24 19 39			11.43	9.84		21	1.78
6*	16 23 52.7	-24 15 44			10.68	9.16		20	1.20
7*	16 23 53.4	-24 13 44			11.65	9.42		28	0.58
8	16 24 00.7	-24 14 54			11.00	9.16		23	0.84
9	16 24 00.7	-24 12 14			11.80	9.90		25	1.45
10	16 23 50.7	-24 08 04			11.40	9.50		25	1.05
11	16 23 42.7	-24 09 44			10.60	9.40		16	1.85
12	16 23 14.8	-24 15 21			11.40	9.80		21	1.70
13	16 24 44.8	-24 16 39		10.54	8.20	7.22	6.56	14	-0.17
14	16 24 48.8	-24 18 54	yes	9.27	7.95	7.32		8	0.52
15	16 25 07.8	-24 16 46		9.51	7.80	7.14		9	0.24
16	16 25 02.8	-24 19 54	yes	8.50	6.96	6.46		7	-0.28
17	16 24 28.8	-24 20 54			11.27	8.58	6.71	40	-1.38
18	16 24 26.8	-24 20 34		≥12.96	10.29	8.97		17	1.32
19	16 22 56.8	-24 11 01	yes		9.55	9.13		5	2.59
20	16 23 06.8	-24 08 01			10.50	9.50		13	2.21

Table 3.1--<u>Continued</u>. IR photometry of 2μm sources in Ophiuchus

VS No.	α(1950)	δ(1950)	Associated with visible star?	J (1.2μm)	H (1.6μm)	K (2.2μm)	L (3.5μm)	A_v	K_o
21	$16^h24^m02^s.8$	$-24°13'24''$		$12^m.30$	$10^m.30$	$9^m.25$	^{m}	13	2.00
22	16 24 20.8	-24 11 24			10.96	9.85		14	2.42
23	16 24 08.0	-24 12 24	yes	9.31	7.98	7.09	6.78	9	0.16
24	16 24 12.8	-24 11 34			10.77	9.63		15	2.16
25	16 24 25.7	-24 24 36		12.31	10.15	9.07		14	1.72
26	16 24 17.0	-24 22 01			10.60	9.16	7.86	25	0.68
27	16 23 28.7	-24 16 14			11.97	9.80		28	1.00
28	16 23 44.7	-24 16 24			11.17	9.94		16	2.35
29**	16 23 24.7	-24 20 14							
30**	16 23 43.0	-24 28 19	possible						
31**	16 24 04.8	-24 22 24	yes						

*2, 6, and 7 are entries 39, 42, and 43, respectively, in the Grasdalen et al. (1973) paper.

**29 to 31 are definite detections at 2.2μm for which no photometry is available.

Table 3.2. Infrared photometry of selected sources from the list of Grasdalen et al. (1973)

Source* (S)	J (1.2μm)	H (1.6μm)	K (2.2μm)	L (3.5μm)	5μm	8.4μm	11.1μm	12.6μm
1	8.70	7.10	6.30	5.80	5.5	5.0	4.9	–
2	11.40	8.20	6.70	5.00	4.6	3.7	3.3	2.6
3	9.60	8.10	7.00	6.30	6.8	5.9	–	–
4	9.10	7.30	6.50	5.90	–	–	–	–
16	9.90	7.90	6.90	5.90	4.8	5.5	–	–
26	11.90	10.57	8.95	6.95	–	–	–	–
28	11.20	8.80	7.80	6.80	–	4.6	4.4	–
29	11.40	9.40	7.30	5.80	4.6	2.4	1.2	0.6

*S-16, S-26, S-28, and S-29 are entries 15, 26, 30, and 31, respectively, in the table of Grasdalen et al. (1973).

43

3.1 E_{BV} and estimate E_{BV} from 4.76 E_{HK}. In practice, the reddening law in this dark cloud complex probably differs from the standard interstellar law since (a) R, the ratio of total to selective absorption, A_V/E_{BV}, is larger than normal, and (b) the slope of the reddening curve in the 1.2 to 3.5μm region is probably steeper. Both effects are expected from the increase in particle size found in dark cloud regions by Carrasco et al. (1973). In practice, these two effects tend to cancel out when A_V is computed according to our procedure.

The results, listed in table 3.1, indicate that $A_V \geq 10$ for most of the observed sources and, moreover, that the large majority are not associated with visible stars. Hence, we must conclude that these sources are either (1) embedded within the cloud, or (2) background to the cloud complex. Explanation (2) seems ruled out for two reasons. First, the spatial distribution of the sources as seen in figure 3.1 suggests a clustering of the sources near the center of the mapped region and avoiding the areas of least obscuration. Secondly, from the distribution of A_V's listed in table 3.1 we find an absorption to the middle of the cloud of about 30 mag. If this is the typical absorption through the cloud over the mapped area, then all sources in or behind the cloud will be obscured by this amount. For a

region located at b^{II} = +17° with an angular size of 36' x 20' we would expect to observe six sources with K brighter than 10.0 mag (i.e., sources which would appear brighter than K = 10.0 observed through a cloud having A_v = 30 or A_k = 3.0 plus foreground sources). This number is clearly much smaller than the 67 sources brighter than K = 10 found in this and the previous survey. It seems most reasonable to conclude that the sources are embedded within the Ophiuchus dark cloud.

In the final column of table 3.1, we list the absolute K magnitudes, corrected for reddening. We have assumed a distance modulus of 160 pc (m-M = 6.0) and estimate the extinction at K as 0.1 A_v. The range of absolute magnitudes listed in table 3.1 suggests that the embedded stars lie between spectral types B3 and F5, if their infrared colors are typical of normal main-sequence stars.

For selected sources, we have obtained long wavelength, infrared photometry (see table 3.2), so that a more certain estimate of their nature could be made. In figure 3.2 we plot the spectral energy distributions for the sources listed in table 3.2. We also indicate on this plot the spectral energy distribution of a 10,000°K blackbody. Except for source numbers 28 and 26, the observed spectral energy distributions appear best interpreted as representing normal early-type stars heavily obscured by dark cloud
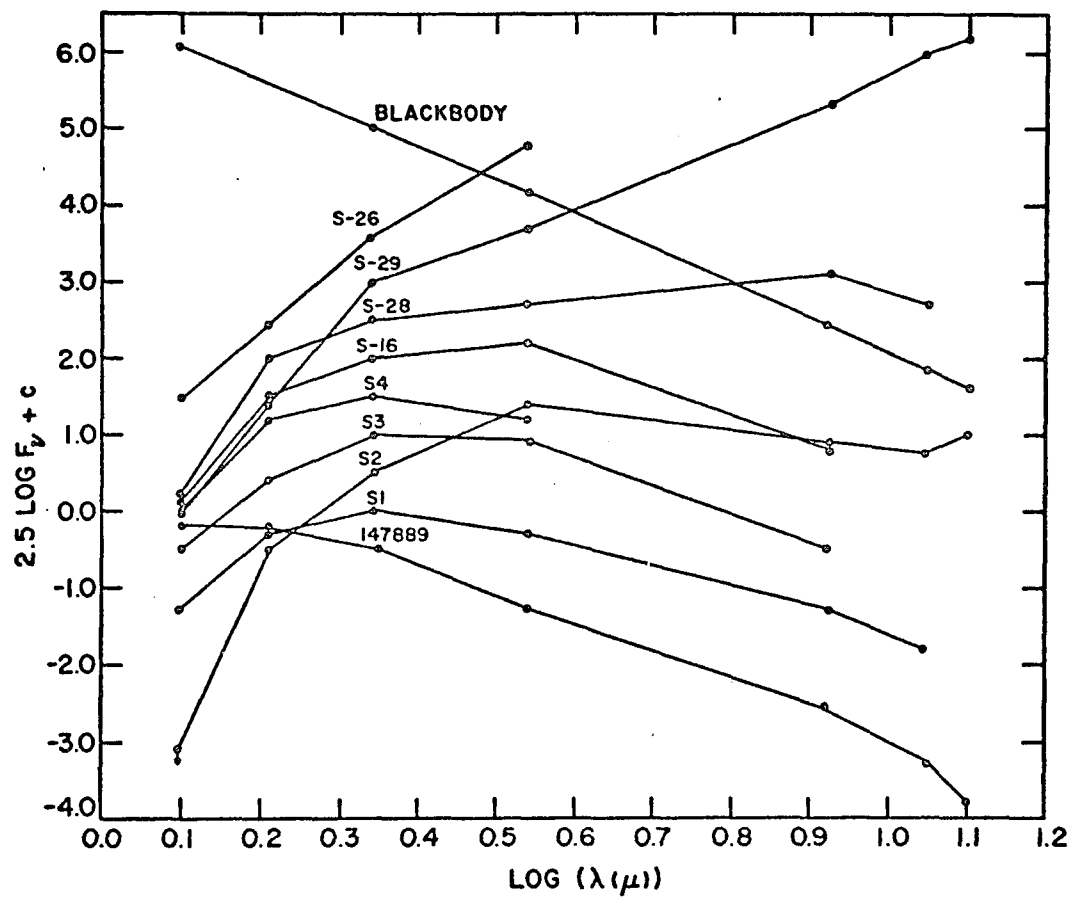
Figure 3.2.   The spectral energy distribution observed for the Ophiuchus sources.

material. S28 and S26 are probably obscured members of the
Orion variable population.

We have also found a source located 30" north of the
peak of (24 GHz) NH_3 (1,1) emission observed by Morris et al.
(1973). Since this source lies well within the estimated
accuracy of the NH_3 position, it seemed worthy of further
investigation. We observed the following colors, using a
36" aperture: K = 9.40, (H-K) = 1.50. A map of this region
made with a 12" beam suggests that this source may be ex-
tended with an approximate size of 20" to 25". Unfortunate-
ly, we did not obtain a detailed measurement of the profile
for the 12" aperture on the nights the NH_3 source was ob-
served; hence, our size estimate may be in error. A map of
a region 1.6' x 1.6' at an effective wavelength of 10µm
revealed no point sources brighter than 4.0 mag. Unfortu-
nately, the method used in making this map discriminated
against detecting a weak, extended, 10-µm source, if any,
associated with the 2µm object. Further observations of
this source at infrared and radio wavelengths would be of
considerable interest.

3.1.3 The Luminosity Function for
       the Embedded Cluster

The arguments presented previously provide compel-
ling evidence to suggest that the Ophiuchus cloud contains
a young cluster obscured from view. It seemed essential to

ask whether this embedded cluster differs significantly from other young clusters previously studied at optical wavelengths.

In table 3.1 we have listed the absolute K magnitudes, M_K, and the estimated visual extinction, A_k. These quantities can be used to derive an estimate of the luminosity function for the upper end of the cluster main sequence. However, because the dark cloud is partially opaque even at 2.2μm, we are forced to correct the raw numbers listed in table 3.1 to take account of the following effects: (1) the variable 2.2μm extinction in the cloud, and (2) the limiting magnitude of our survey. To do this, we are forced to adopt a model for the distribution of dust and stars in the dark cloud. We have assumed a plane-parallel geometry for the cloud with both the dust density and stellar density increasing inward from the cloud boundary. We represent the dust density as

$$\rho_d = \rho_0 x^n \qquad (3.1)$$

and the stellar density as

$$\rho_s(M_K) = \rho(M_K) x^m. \qquad (3.2)$$

Here, ρ_0 is the dust density at the outer edge of the cloud, while $\rho(M_K)$ is the density of stars of absolute magnitude M_K at the cloud boundary. To appear brighter than our

survey limit, M_ℓ, a star of absolute magnitude M_K must be obscured by no more than τ, where

$$\tau < (M_K - m_\ell) - D_m \equiv \Delta(M_K). \tag{3.3}$$

Here D_m is the distance modulus to the Ophiuchus cloud. The optical depth can be expressed in terms of the dust density and the dust opacity, κ,

$$\tau = \int_0^\ell \kappa \rho_d \, dx. \tag{3.4}$$

We should have discovered all sources of absolute magnitude M_K provided that the distance in from the cloud edge, ℓ, is less than the following value:

$$\ell \leq \left(\frac{n+1}{\rho_0 \kappa} \right)^{1/(n+1)} [\Delta(M_K)]^{1/(n+1)} \tag{3.5}$$

The observed number of sources, $N(M_K)$, will be given by

$$N(M_K) = A \int_0^\ell \rho(M_K) x^m \, dx \tag{3.6}$$

where A is the area (pc^2) surveyed. Hence, the true stellar density, $\rho(M_K)$, can be derived from

$$\rho(M_K) = \frac{m+1}{A} \left[\frac{\rho_0 \kappa}{(n+1)\Delta(M_0)} \right]^{(m+1)/(n+1)} N(M_K). \tag{3.7}$$

From our previous discussion, we estimate that A_v reaches a value of $\simeq 30$ mag to the cloud center, or an optical depth $\tau_c = 3.0$ mag at K. With an estimated cloud radius, r (1.4

pc), we can estimate the true luminosity function at the cloud center as

$$\rho_c(M_K) \simeq \frac{(m+1)}{rA} \left[\frac{\tau_c}{\Delta(M_K)} \right]^{(m+1)/(n+1)} \tag{3.8}$$

In table 3.3, we list the observed values of $N(M_K)$ and the values of $\rho_c(M_K)$ derived under the assumption that $m = 4$ and $n = 2$. These values are appropriate for a cloud undergoing spherical collapse at constant velocity and a rate of star formation proportional to the square of the density. A crude check on our model is provided by the observed distribution of optical depth, $N(A_V)$. At an optical depth, τ, we observe all stars with

$$M_K \leq (m_\ell - \tau) - D_m \equiv \Delta(\tau). \tag{3.9}$$

Hence,

$$N(\tau) = x^m \int_{-\infty}^{\Delta(\tau)} \rho(M_K) \, dM_K. \tag{3.10}$$

To derive $N(\tau)$, we have fitted a parabola to our derived luminosity function, $\rho_c(M_K)$, to evaluate the above integral. The resulting $N(\tau)$ is plotted in figure 3.3 and compared with the observed distribution, $N(A_V)$. The agreement is surprisingly good given the crudeness of our model. In figure 3.4, we compare our derived luminosity function with a luminosity function deduced from Walker's (1956) observations of the young cluster NGC 2264; a scale shift has been applied to

Table 3.3. Derived luminosity functions observed
            for the Ophiuchus cluster

M_K	$N(M_K)$	(pc^{-3})
-2.0	0	–
-1.5	2	1.3
-1.0	1	0.7
-0.5	4	3.7
0.0	3	3.4
0.5	5	7.0
1.0	5	9.1
1.5	5	12.3
2.0	5	17.9
2.5	4	23.1
3.0	0	–
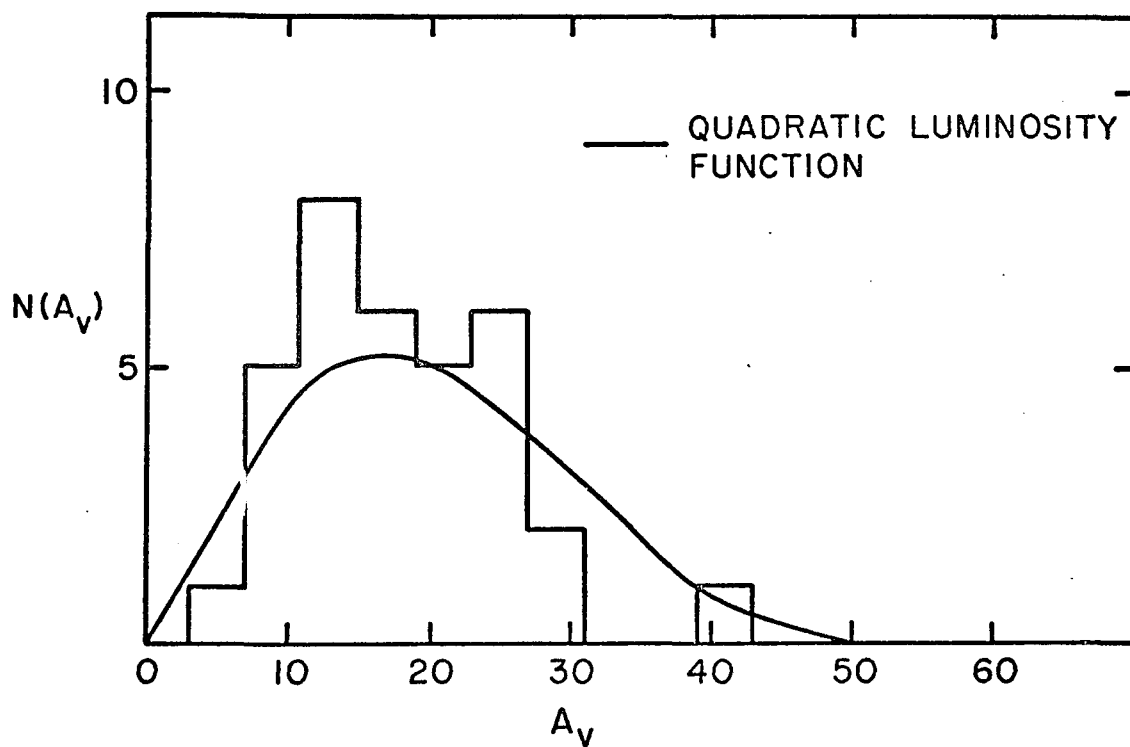
Figure 3.3.   A plot of the observed and predicted
              distributions of extinction values, A_v.

              The predicted curve follows from our
              simple model of the distribution of
              stars and dust in the Ophiuchus cloud.
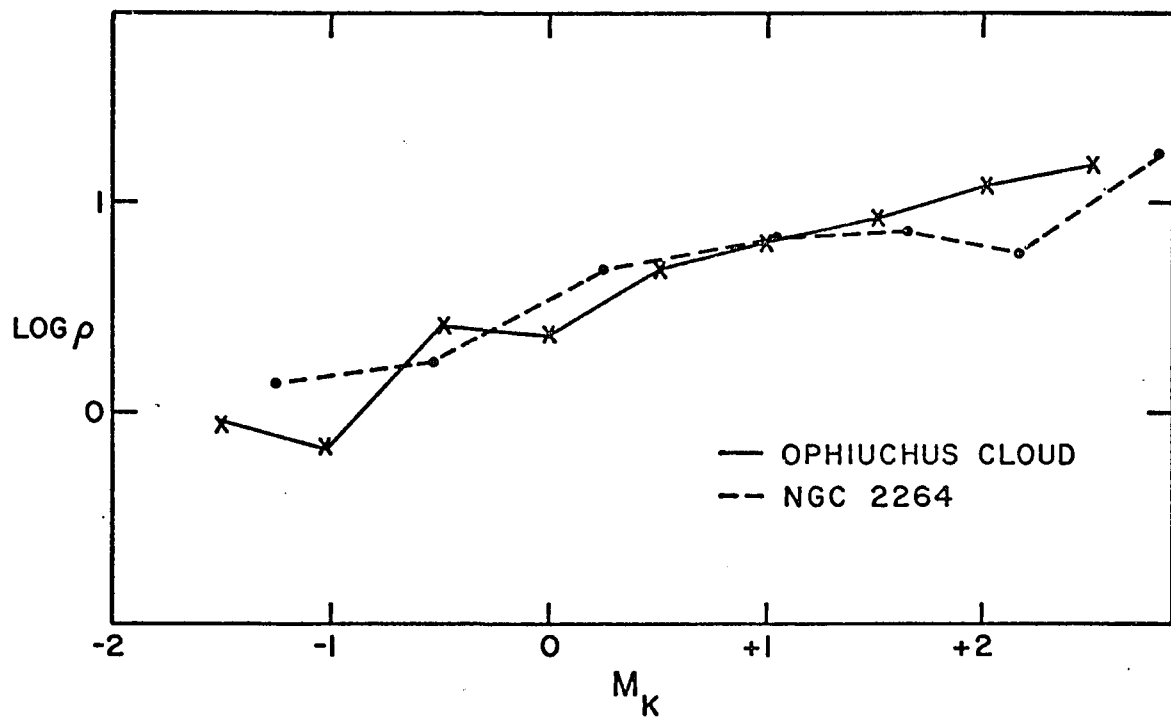
Figure 3.4. A plot of the luminosity function derived for the embedded Ophiuchus cluster compared with the observed luminosity function for NGC 2264 (Walker 1956).

the NGC 2264 data. A similar result is found if our $\rho(M_K)$ is compared with the Salpeter (1953) initial luminosity function. Walker (1957) has demonstrated for three young clusters the coincidence of the observed and initial Salpeter luminosity functions. Thus, these comparisons strongly suggest that the cluster embedded in the Ophiuchus cloud has a luminosity function no different from that characterizing other young clusters.

3.2 M78 Dark Cloud

3.2.1 Previous Work

The region including NGC 2068, NGC 2071, and NGC 2023 comprising Lynds 1630 appears to be replete with young stellar objects including early-type pre-main sequence and main sequence stars, Orion population variables, and embedded sources which have been investigated by Strom, Strom, Carrasco, and Vrba (1975). The important points of their work salient to our investigation may be summarized as:

1. Early type population: The bright stars illuminating NGC 2023, 2068, and 2071 are very young objects ($1-3 \times 10^5$ yr), which appear to represent three distinct regions of star formation.

2. Orion population variables: Infrared and visible photometry suggest that these stars are no different than their Orion counterparts.

3. Embedded populations: A small region of 6' x 6' centered upon NGC 2068 was mapped at 2.2µm to a limiting magnitude of about K = 10. The 13 sources discovered were assumed to be the brightest members of an embedded stellar association.

From their results it was obvious that this area was rich in recent star formation. It thus seemed vital to carry out a more extensive 2.2µm mapping program covering a larger area and to a fainter limiting magnitude to answer several important questions:

1. Observations of the visible, young stars and limited 2.2µm mapping led us to believe that NGC 2023, 2068, and 2071 are distinct sites of star formation. To what extent this is true may be answered by mapping not only the NGC 2068 and 2071 regions, but also the area between them.

2. Mapping to a fainter limiting magnitude allows one to investigate a fainter portion of the luminosity function of the embedded population.

3. Obtaining infrared colors for the embedded sources in the manner of section 3.1.2 allows A_V and $\rho_c(M_K)$ to be estimated.

3.2.2 Observations

The infrared maps obtained for the central region of Lynds 1630 (including NGC 2068 and NGC 2071) employed a

somewhat more sensitive InSb detector than that used in the Ophiuchus cloud. The limiting magnitude of our M78 region survey was approximately K = 10.7. We again used a beam size of 36", chopping throw of 38", and a grid spacing of 30". The approximate area covered by the survey is indicated by the solid outline inscribed in figure 3.5 over a red photograph of the NGC 2068 and NGC 2071 region taken by G. L. Grasdalen using the 24 inch Curtis-Schmidt telescope at Cerro Tololo Inter-American Observatory; a water-hypersensitized 098-02 emulsion and an RG-610 filter define the effective bandpass. Also indicated on the figure is the location of all sources we discovered during the survey.

In table 3.4 we list the epoch 1950 positions of all discovered 2.2μm sources, whether or not they are likely associated with a visible star, and J(1.2μm), H(1.6μm), K(2.2μm), and L(3.4μm) photometry. We also list the visual absorptions in front of the sources which were computed in the same manner as in section 3.1.2. The final column lists the inferred absolute magnitude assuming the calculated A_v and a distance modulus of 8.5 (500 pc).

3.2.3 Nature of Observed Sources

Whether the observed sources are foreground, background, or located within the dark cloud is somewhat more difficult to ascertain than for the Ophiuchus cloud. From the distribution of A_v's listed in table 3.4 we find an

Figure 3.5. A plot of the sources discovered in the course of the 2.2μm
survey of the Lynds 1630 (M78) cloud.

A red photograph of the NGC 2068 and NGC 2071 region taken
by G. L. Grasdalen using the 24 inch Curtis-Schmidt telescope
at Cerro Tololo Inter-American Observatory; hypersensitized
098-02 emulsion, and an RG-610 filter define the effective
bandpass. The solid line shows the approximate area mapped
and we show the positions of all 2.2μm sources we discovered
in this survey.
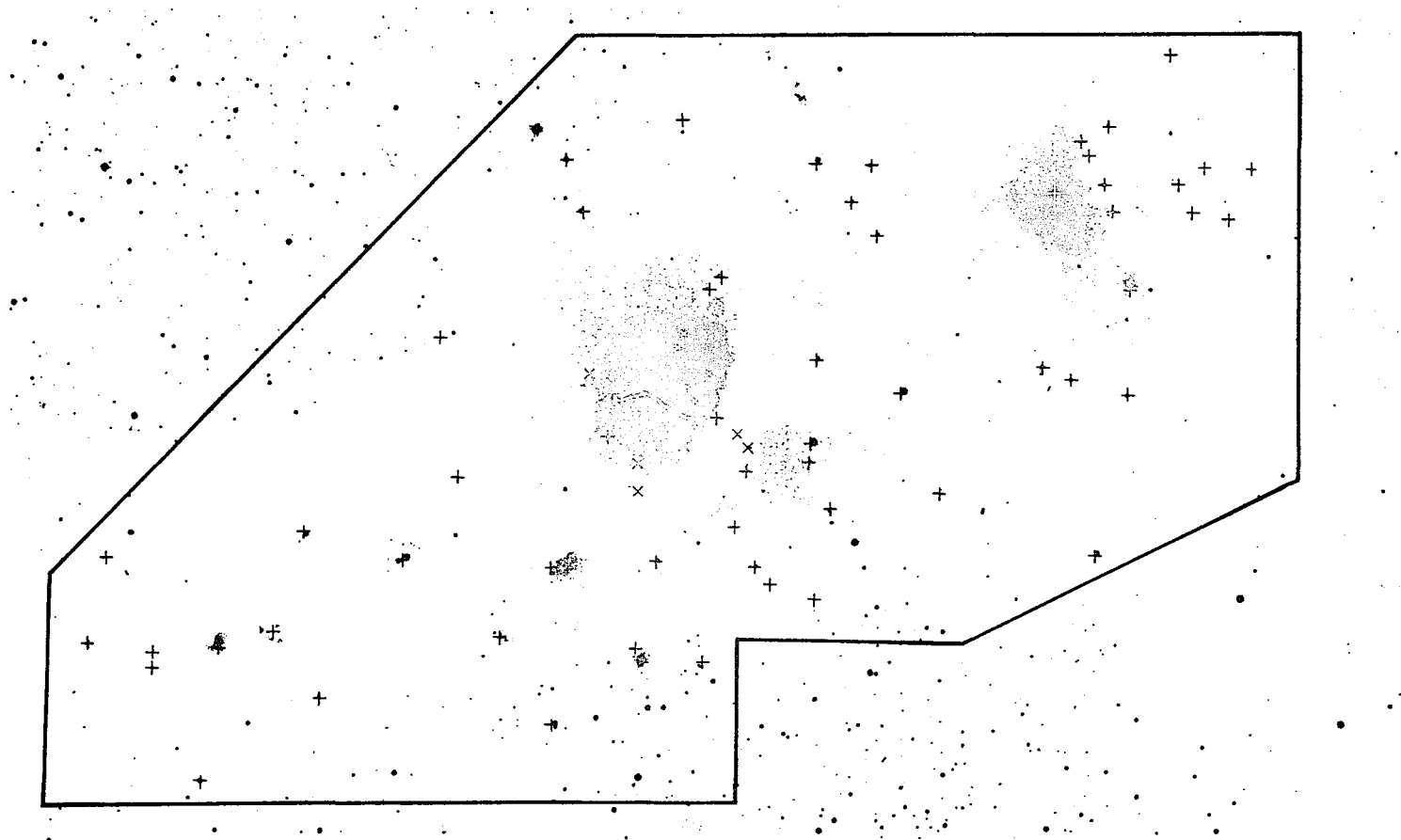
Figure 3.5.   A plot of the sources discovered in the course of the 2.2μm
              survey of the Lynds 1630 (M78) cloud.

Table 3.4. Infrared photometry of the 2μm sources in M78 discovered in this survey

No.	α(1950)	δ(1950)	Associated with visible star?	J (1.2μm)	H (1.6μm)	K (2.2μm)	L (3.5μm)	A_V	K_o
1a	$05^h44^m10^s.9$	$00°04'17''$	yes	$7^m.45$	$7^m.01$	$6^m.72$	$6^m.51$	4	−1.8
2	05 44 02.9	00 05 17			10.35	9.94		6	1.2
3b	05 44 16.9	00 03 32	yes		10.86	10.33		8	1.4
4	05 44 06.9	00 03 52	yes		10.10	9.87		3	1.5
5	05 44 04.9	00 04 40			12.08	10.68		21	0.5
6	05 44 00.9	00 05 47	yes		11.04	10.08		14	0.6
7	05 43 56.9	00 05 47	yes		11.54	10.80		11	1.6
8	05 44 00.9	00 03 17				11.07			
9c	05 44 11.6	00 01 37	yes	9.75	9.12	8.70	7.78	6	0.0
10	05 44 04.9	00 00 47	yes			11.68			
11	05 44 02.9	00 00 32		11.41	10.20	9.64		8	0.7
12	05 44 15.6	00 01 17	yes			11.28			
13	05 43 58.9	00 01 47	yes		10.59	9.91		10	0.8
14	05 44 12.9	00 08 12	yes			10.66			
15d	05 44 01.6	00 07 47	yes		10.79	10.09		10	1.0
16	05 43 58.9	00 07 47	yes			10.81			
17	05 44 24.9	00 04 37	yes	11.01	10.01	9.58		6	0.9
18	05 44 22.9	00 04 17	yes			10.80			
19	05 44 09.6	−00 00 13	yes		10.82	8.73	6.52	31	−2.5
20	05 44 30.9	00 10 17	yes			12.21			

Table 3.4--<u>Continued</u>. IR photometry of 2μm sources in M78

No.	α(1950)	δ(1950)	Associated with visible star?	J (1.2μm)	H (1.6μm)	K (2.2μm)	L (3.5μm)	A_v	K_o
21e	$05^h44^m33^s.2$	$00°18'17''$	yes	$11^m.11$	$9^m.70$	$8^m.76$	$8^m.63$	14	-0.7
22	05 44 31.2	00 17 32	yes	11.55	10.08	9.75		5	1.2
23f	05 44 40.2	00 08 02	yes	10.66	9.59	8.44	7.02	17	-1.4
24	05 44 35.6	00 09 17	yes	10.94	10.82	10.27	10.47	8	1.4
25	05 44 33.9	00 16 47	yes	6.91	6.49	6.25	6.17	4	-2.2
26g	05 44 37.6	00 18 07	yes	13.00	10.23	9.12		16	-0.6
27	05 44 37.2	00 16 57	yes	11.61	10.33	9.76		8	0.9
28	05 44 41.2	00 17 32			11.33	9.86		22	-0.4
29	05 44 45.6	00 18 22			11.37	10.38		15	0.8
30	05 44 43.6	00 17 27				10.49			
31	05 44 40.9	00 10 47			11.15	10.19		14	0.7
32	05 44 55.2	00 12 22			11.01	10.10		13	0.7
33h	05 44 08.6	00 11 07	yes			10.99		7	2.2
34i	05 44 11.6	00 15 47	yes	11.28	9.95	9.45		7	0.7
35	05 44 10.6	00 16 52	yes		10.58	10.35		3	2.0
36	05 44 53.9	00 19 47			11.15	9.83	8.56	20	-0.3
37	05 44 36.9	00 20 17				10.79			
38j	05 44 23.6	00 18 57	yes	9.63	9.46	9.18		4	0.7
39	05 44 08.6	00 19 07	yes			10.28			
40	05 44 30.6	00 22 12			10.80	9.32		22	-1.0

Table 3.4--Continued. IR photometry of 2μm sources in M78

No.	α(1950)	δ(1950)	Associated with visible star?	J (1.2μm)	H (1.6μm)	K (2.2μm)	L (3.5μm)	A_V	K_o
41	$05^h44^m31^s.4$	$00°20'57"$		^{m}	$10^m.95$	$8^m.80$	$6^m.86$	32	-2.5
42	05 44 38.9	00 21 17			11.46	10.47		15	0.9
43	05 44 39.0	00 23 37				10.81			
44k	05 43 40.6	00 22 57	yes		10.41	10.21		3	1.8
45	05 44 46.6	00 02 57				10.48			
46l	05 44 32.9	-00 00 13	yes		10.77	9.99		12	0.7
47m	05 44 40.4	-00 00 53	yes		9.48	8.95		8	0.1
48	05 43 44.9	-00 01 23	yes		10.25	9.09	7.81	17	-0.7
49n	05 43 44.9	00 02 22	yes		9.49	8.38	7.46	16	-1.3
50	05 43 32.9	00 01 07			9.36	9.49			
51o	05 43 31.2	00 03 42	yes	10.74	9.99	9.26	8.19	11	0.1
52	05 43 50.9	00 04 37			12.15	10.53		24	0.0
53	05 43 42.9	00 06 07			11.47	10.86		9	1.9
54	05 43 44.9	00 05 57	yes		10.92	10.06		13	0.7
55	05 43 52.4	00 08 17	yes			12.04			
56	05 43 40.4	00 07 47				11.66			
57	05 43 34.9	-00 03 13	yes	11.15	10.08	9.38	8.31	10	0.3
58	05 43 22.6	-00 01 23	yes	10.04	9.80	9.44		5	0.8
59	05 43 31.6	-00 15 23		12.67	9.97	8.69	8.07	19	-1.3
60	05 43 34.2	-00 15 23							

Table 3.4--<u>Continued</u>.   IR photometry of 2µm sources in M78

No.	α(1950)	δ(1950)	Associated with visible star?	J (1.2µm)	H (1.6µm)	K (2.2µm)	L (3.5µm)	A_v	K_0
61	$05^h43^m34^s.9$	$-00°12'58''$	yes	m	m	m	m		
62	05 43 34.2	-00 17 33	yes						
63	05 43 35.6	-00 11 03	yes						
64p	05 43 45.6	-00 06 33	yes						
65	05 43 26.9	-00 09 23	yes						
66q	05 43 15.3	-00 13 45	yes						
67	05 43 54.9	-00 04 58		11.44	9.58	8.62		14	-0.9
68	05 43 48.9	-00 10 03	yes	11.45	10.41	10.11		4	1.6
69	05 43 48.6	-00 16 13			11.23	10.94	4	4	2.4
70	05 44 16.6	-00 04 48		11.09	10.08	9.78		4	1.3

a.   HD 38563N
b.   Lk Hα 306
c.   HD 38563C
d.   polarization star #4 of Table 4.5
e.   Lk Hα 308
f.   Lk Hα 314, polarization star #37 of Table 4.5
g.   Lk Hα 310
h.   polarization star #3 of Table 4.5
i.   Lk Hα 305

Table 3.4--Continued. IR photometry of 2μm sources in M78

j. polarization star #1
k. polarization star #36
l. Lk Hα 309, polarization star #19
m. Lk Hα 312-313
n. Lk Hα 300
o. Lk Hα 298
p. Lk Hα 301, polarization star #17
q. Lk Hα 295

absorption to the middle of the cloud of about 23 mag. If this is the typical absorption through the cloud over the mapped area, then all sources in or behind the cloud will be obscured by this amount. For a region located at b^{II} = +15° and of area 720 square minutes we would expect about 16 sources with K brighter than 10.7 (i.e., sources which would appear brighter than K = 10.7 observed through a cloud having A_K = 2.3 plus foreground sources). This number is 20 percent of the 70 sources discovered in our survey. Furthermore, about two thirds of the observed sources appear to be associated with visible stars.

However, most of the sources we expect to observe are faint foreground stars due to the cloud's relatively large distance (500 pc) and our faint limiting magnitude. Thus, while it is clear that our observed source list is contaminated by sources not associated with Lynds 1630 (perhaps 20% contamination) most of the sources must be associated with the cloud material. The fact that many more of them are seen in visible light than those in Ophiuchus indicates that either Lynds 1630 has lower average opacity or that stars are able to form closer to the cloud boundaries.

We have been able to form the 2.2μm luminosity function for the discovered sources in the same manner we did in section 3.1.3. In this case we estimate that

$\tau_c \simeq 2.3$ mag at K to the cloud center and the cloud radius, r, as 1.8 pc. The area mapped is 720 square minutes of arc and the cloud distance is taken at 500 pc. In table 3.5 we list the observed values of $N(M_K)$ and the values of $\rho_c(M_K)$ derived under the assumption that m = 4 and n = 2. In figure 3.6 we compare our derived $\rho_c(M_K)$ again with the results for NGC 2264 from Walker's (1956) observations. The comparison suggests that the cluster embedded in Lynds 1630 has a 2.2μm luminosity function identical to that character- izing other young clusters. It is certainly possible that some of the embedded sources are Orion population stars due to the fact that optically visible stars of this sort are numerous in this area. Unfortunately, we were not able to obtain longer wavelength infrared photometry of any of our sources to determine the nature of circumstellar shells which may surround some of these stars.

3.2.4 Spatial Distribution of Discovered Sources

The distribution of the sources on the plane of the sky as seen in figure 3.5 seems to rule out the possibility that NGC 2068 and NGC 2071 are isolated centers of star formation. Rather, it indicates that the nebulae are regions where an episode of star formation took place at a somewhat earlier time than the rest of the dark cloud and strong stellar winds have been able to develop to clear away

Table 3.5. Derived luminosity functions observed
for the M78 cluster

M_K	$N(M_K)$	(pc^{-3})
-3.0	0	-
-2.5	2	0.1
-2.0	2	0.1
-1.5	3	0.2
-1.0	2	0.1
-0.5	5	0.4
0.0	4	0.4
0.5	10	1.4
1.0	9	1.7
1.5	6	1.6
2.0	4	1.7
2.5	1	0.9
3.0	0	-
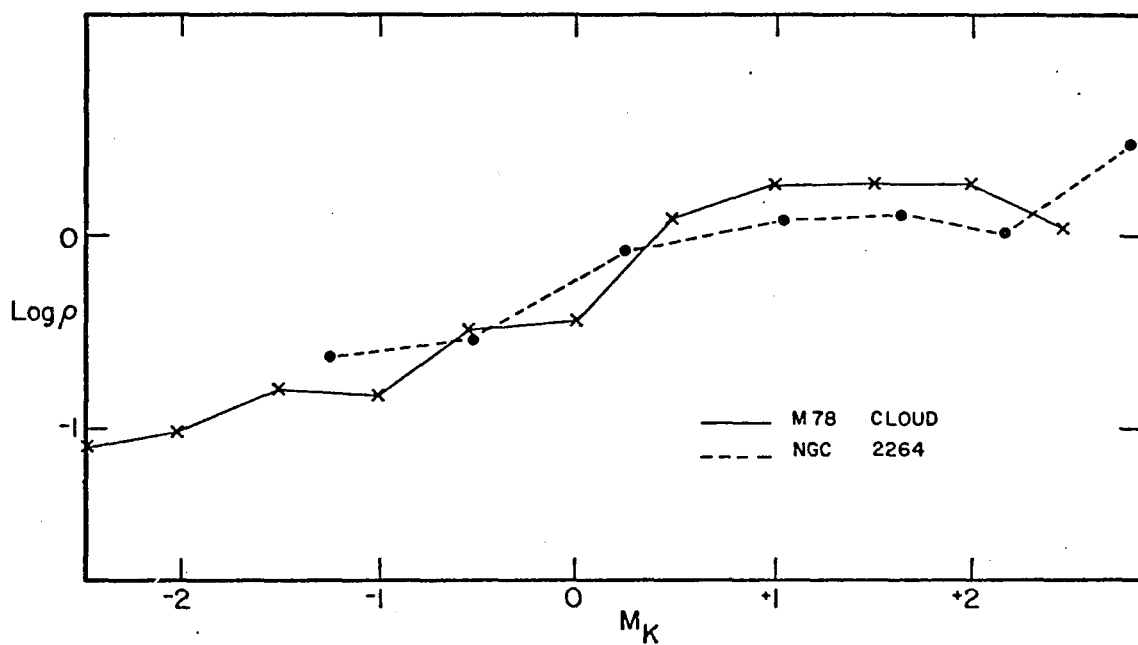
Figure 3.6. A plot of the luminosity function derived
for the sources discovered in the Lynds
1630 2.2μm survey.

This is compared with the observed lumi-
nosity function for NGC 2264 (Walker 1956).
A scale shift has been applied to the
NGC 2264 data.

obscuring material. Alternatively, NGC 2068 and NGC 2071 are regions where stars were able to form systematically closer to the near edge of the cloud.

Comparison of tables 3.3 and 3.5 shows that while the luminosity functions of the Ophiuchus and Lynds 1630 clouds are very similar, the spatial density of sources is approximately 10 times larger for Ophiuchus than for Lynds 1630.

3.3   Corona Austrina Dark Cloud

3.3.1   Observations

The mapping at 2.2μm of the Corona Austrina dark cloud was carried out with the same system used to map the Ophiuchus cloud. The maps were carried out to a limiting magnitude of K = 10.0 using a 36" chopper throw, and 30" spacing between mapping points. An area of 364 square minutes of arc was covered and is approximately outlined by the rectangle inscribed in figure 3.7, which is a POSS red print. Also indicated on this figure by "+" signs are the approximate positions of all sources discovered in this region. In table 3.6 we list the source number, epoch 1950 position, whether or not the sources are likely associated with a visible star and J(1.2μm), H(1.6μm), K(2.2μm), and L(3.5μm) magnitudes.

Figure 3.7. A POSS red photograph of the region of the
             Corona Austrina dark cloud mapped at 2.2μm.

             The inscribed rectangle approximates the
             area mapped and the "+" symbols indicate the
             approximate positions of the discovered
             sources. There is no difference in meaning
             between the black and white "+" symbols.
             Several bright stars are marked by their
             variable star designation. Stars 1 and 2
             refer to Anon. 1 and Anon. 2 discussed by
             Knacke et al. (1973).
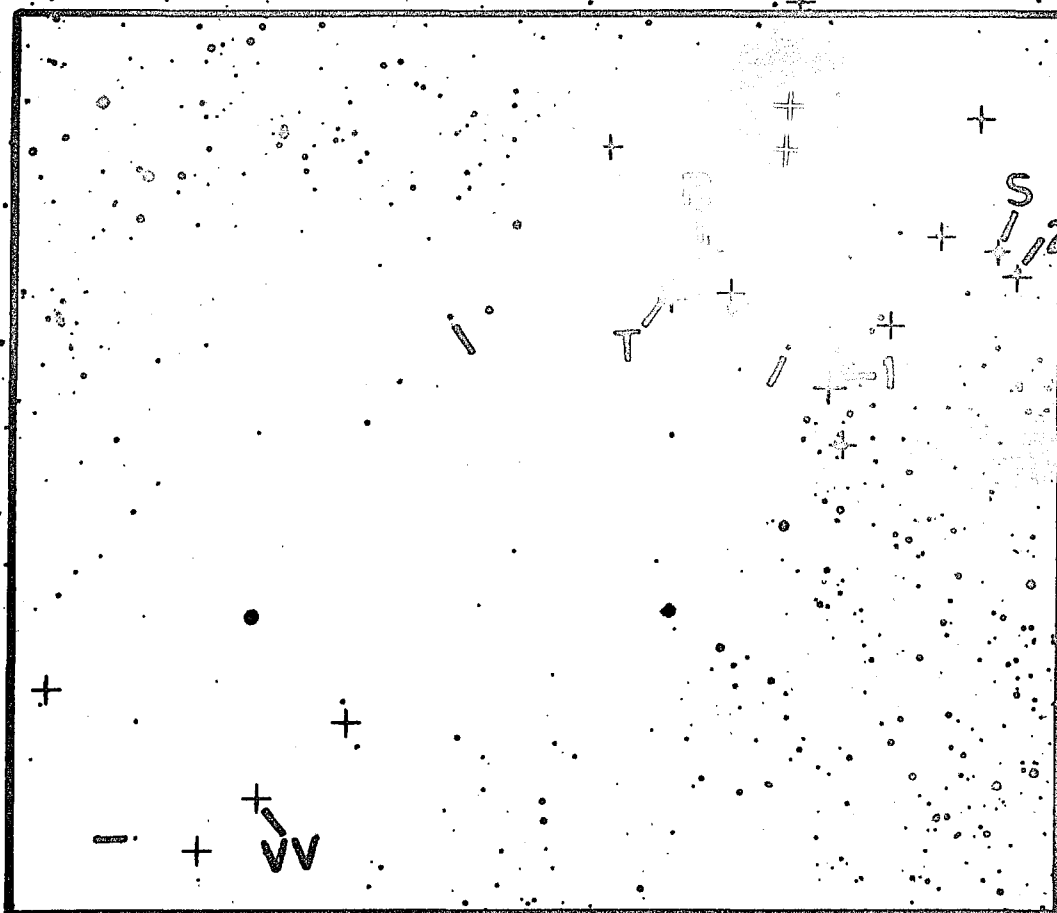
Figure 3.7.   A POSS red photograph of the region of the
              Corona Austrina dark cloud mapped at 2.2μm.

Table 3.6. Infrared photometry of the 2μm sources in Corona Austrina
discovered in this survey

No.	α(1950)	δ(1950)	Associated with visible star?	J (1.2μm)	H (1.6μm)	K (2.2μm)	L (3.5μm)
1a*	$18^h58^m31^s5$	$-37°01'22''$	yes	^{m}	5^m4	3^m7	1^m8
2b*	18 58 36.5	-37 02 10	yes		7.6	6.4	4.8
3c*	18 57 46.2	-37 01 36	yes		7.1	6.5	4.7
4d*	18 59 44.1	-37 17 14	yes			6.1	4.5
5e*	18 58 16.6	-36 57 45	yes		7.0	6.8	6.4
6	18 57 48.2	-36 57 36		11.82	9.75	8.77	
7	18 58 45.2	-36 57 34	yes	9.3	·7.41	6.74	6.08
8	18 58 15.5	-36 53 22			8.5	8.13	
9	18 58 19.5	-36 55 35			7.14	7.01	
10	18 59 54.1	-37 18 29	?	11.19	10.02	9.09	
11	18 59 30.1	-37 14 14	yes	10.75	9.65	9.01	
12	19 00 16.1	-37 13 54	yes			10.32	
13 *	18 58 12.4	-37 05 13	yes		7.9	7.8	6.7
14 *	18 57 44.5	-37 02 16	yes		7.6	7.2	6.8
15f	18 58 28.3	-37 02 27		>12.0	10.2	6.8	4.5
16	18 58 12.4	-37 07 17	yes		10.05	9.9	8.2
17	18 57 56.2	-37 01 06	yes				
18	18 58 04.2	-37 03 36	yes				
19	18 58 33.5	-37 03 02					

Table 3.6—Continued. IR photometry of 2μm sources in Corona Austrina

  a. R CrA

  b. T CrA

  c. S CrA

  d. VV CrA

  e. TY CrA

  f. Herbig-Haro 100 source (photometry from Strom, Strom, and
      Grasdalen (1974)

  *   photometry from Knacke et al. (1973)

3.3.2 Nature of Observed Sources

Most of the sources discovered in this survey appear to be associated with a visible star (13 of 18). Furthermore, many of these stars are members of the young association of stars which posses T Tauri characteristics and are likely no older than 10^6 years, which have already been studied by Knacke et al. (1973). It is also likely that the invisible sources are embedded members of this same family.

One of the embedded sources (number 15) has been shown by Vrba et al. (1975) to likely be the illuminating source for Herbig-Haro object number 100. Strom, Strom, and Grasdalen (1974) and Strom, Grasdalen, and Strom (1974) have argued that the illuminating sources for such objects are extremely young members of the Orion population variables embedded in dark cloud material. Another source (number 16) may have a connection with Herbig-Haro No. 101, the center of which lies within 35" of the IR source.

Thus, we see that most of the discovered sources are associated with young, visible stars that are illuminating nearby reflection nebulae. Little further star formation appears to have taken place in the form of embedded sources and, therefore, the visible picture of star formation in this cloud is not far from the total picture. This indicates that (1) the cloud has a rather low total opacity, or that (2) the episode of star formation which formed these

objects has ended, the formed stars having been able to remove the foreground dark cloud material.

Two things may be noted about the spatial distribution of the discovered sources. The first is that most of the sources lie near the region of R CrA, which is located at the tip of the dark cloud material which lies closest to the galactic equator. The second is the low number of sources in this cloud per square parsec surveyed, as compared to other clouds we have surveyed. This indicates that the CrA dark cloud is a region where recent, limited star formation has occurred.

3.4 NGC 1333 Dark Cloud

3.4.1 Observations

The 2.2μm mapping of the NGC 1333 dark cloud was carried out with the same detector as was used to map the Ophiuchus cloud (to a limiting magnitude of K = 10.0). As with the other clouds, we have used a beam size of 36", chopper throw of 38", and a spacing between mapped points of 30". Table 3.7 lists the source number, epoch 1950 coordinates, whether or not the source is associated with a visible star, and photometry of the sources at J(1.2μm), H(1.6μm), K(2.2μm), and L(3.4μm). The last two columns of this table give the inferred visual absorptions to the sources as obtained by the method outlined in section 3.1.2

Table 3.7.   Infrared photometry of the 2µm sources in NGC 1333 discovered in
this survey

No.	α(1950)	δ(1950)	Associated with visible star?	J (1.2µm)	H (1.6µm)	K (2.2µm)	L (3.5µm)	A_v	K_o
1a	$03^h26^m14^s.1$	$31°14'33''$	yes	$8^m.90$	$8^m.57$	$8^m.44$	^{m}	2	-0.3
2b	03 26 12.1	31 12 13	yes	9.71	8.69	7.93	6.63	11	-1.7
3c	03 26 04.8	31 11 33	yes	9.02	7.74	6.96	5.19	11	-2.6
4d	03 26 20.1	31 16 13	yes	11.30	10.32	9.43		13	-0.4
5e	03 26 15.1	31 08 03		11.60	10.91	9.75		17	-0.4
6f	03 26 22.1	31 16 33	yes	11.76	10.37	10.08		4	1.2
7	03 26 04.1	31 12 33	yes	11.04	10.83	9.55		19	-0.8
8g	03 25 58.8	31 12 03	yes	11.80	10.34	8.85		22	-1.8
9h	03 25 38.1	31 07 03	yes	11.70	10.00	8.75		19	-1.6
10i	03 25 46.1	31 08 03	yes	11.50	10.26	9.74		8	0.4
11	03 25 51.8	31 08 03			10.80	9.59		18	-0.7
12j	03 25 56.1	31 09 48			11.50	9.44		30	-2.1
13	03 25 58.1	31 05 33		12.85	10.74	9.08		25	-1.9
14k	03 26 00.1	31 06 18			11.29	9.85		21	-0.7
15	03 25 51.1	31 06 03	yes	11.92	9.80	8.30		22	-2.4
16	03 25 53.7	31 05 26			12.65	9.81	7.66	42	-2.9
17	03 25 42.1	31 06 43	yes			10.80			
18	03 25 48.1	31 06 33	yes			10.76			
19	03 25 52.1	31 04 03	yes						
20l	03 26 16.1	31 05 03	yes		10.44	9.56		13	-0.2

Table 3.7--<u>Continued</u>. IR photometry of 2μm sources in NGC 1333

No.	α(1950)	δ(1950)	Associated with visible star?	J (1.2μm)	H (1.6μm)	K (2.2μm)	L (3.5μm)	A_V	K_o
21m	$03^h25^m40^s.1$	$31°06'03''$	yes		$11^m.32$	$10^m.86$		7	1.7
22	03 26 24.1	30 58 28	yes	13.29	11.57	11.21		5	2.2
23	03 26 02.1	31 00 23	yes		≥13.00	11.11		>28	<-0.3
24	03 25 40.1	30 59 08	yes	12.10	10.54	9.97		8	0.7
25	03 26 21.4	30 57 33		11.96	10.66	10.01		10	0.5

a. +30° 549
b. Lk Hα 270
c. polarization star 5
d. polarization star 2
e. possible source for Herbig-Haro Nos. 4 and 17
f. polarization star 1
g. polarization star 31
h. star at tip of fan nebula
i. Lk Hα 352
j. Z shaped nebula source (Herbig-Haro No. 12)
k. source for emission knot and Herbig-Haro Nos. 7 through 11
l. Lk Hα 271
m. Lk Hα 351

and the K absolute magnitude deduced from the observed K magnitude, computed A_k, and assuming a distance modulus of 8.5. Figure 3.8 shows the approximate positions of all sources discovered in this survey by "+" symbols which are overlayed onto a portion of the POSS red photograph of this region. There is no difference in meaning between the black and white "+" symbols. The inscribed black outline shows the approximate area covered by the survey.

3.4.2 Nature of the Sources

It is not difficult to demonstrate that most of the sources discovered in the survey are associated with the dark cloud material. For an area of 380 square minutes of arc at $b^{II} = +20°$ and assuming an average total absorption through the cloud of $A_k = 2.3$ mag (from inspection of table 3.7), we would expect to find about 5 sources of $K \leq 10.0$. The volume integrals which derive this number show that all of these should be foreground stars. Secondly, we note that many of the sources we observe are associated with visible stars that illuminate nearby reflection patches and are therefore clearly part of the cloud. Finally, the unusual pattern that the sources display in figure 3.8 is one that would not be expected from foreground stars. The pattern which clearly follows the string of nebulosity from northeast to southwest, and then turns abruptly to the southeast, seems to form a boundary that contains all but one of the

Figure 3.8.   A POSS red photograph of the region of the
               NGC 1333 dark cloud mapped at 2.2µm.

               The inscribed rectangle approximates the
               area mapped and the "+" symbols indicate
               the approximate positions of the discovered
               sources. There is no difference in meaning
               between black and white "+" signs.

Figure 3.8. A POSS red photograph of the region
            of the NGC 1333 dark cloud mapped
            at 2.2μm.

sources. Several of the sources appear to be the illuminating objects for reflection nebulae and, thus, are clearly part of the cloud. Our sources 12 and 14 appear to be coincident with the two infrared sources discussed by Strom, Grasdalen, and Strom (1974) as the illuminating sources for Herbig-Haro No. 12 and Herbig-Haro Nos. 7 through 11 respectively. Source 9 lies at the tip of a fan-shaped nebulae and thus may be its illuminating source. Therefore, it seems likely that most of the sources are indeed associated with the dark cloud.

Unfortunately, we were not able to obtain long wavelength photometry for the sources and thereby directly confirm the nature of the sources not associated with visible stars. We must therefore do this by indirect means. A number of early type Hα emission line stars exist in the NGC 1333 region, probably members of the Orion variable population. Several of our sources (Nos. 2, 10, 20, and 21) appear to be members of this population, and there is no reason to believe that the embedded sources are any different. The computed range of absolute K magnitudes in table 3.7 suggests a range of spectral types from O to early A. Thus, NGC 1333 appears to be a region populated by a small cluster of stars with ages no more than a few times 10^5 years.

CHAPTER 4

POLARIZATION MEASUREMENTS

We now turn to the linear polarization measurements from which we hope to map the magnetic field structure within the dark clouds selected in Chapter 2. The polarimeter described in section 3.1.2 was used in making all the observations reported here. Since the measurements for any cloud took several nights of observation, a number of different apertures were employed ranging from 10" to 20", depending upon seeing conditions and sky brightness. Also dependent upon these conditions and the brightness of the star observed were the times of integration chosen for each position of the polaroid wheel and the number of rotations of the wheel. Since all of these parameters were changed many times during the course of observation of any one cloud, we make no attempt to list them for observations of individual stars. We expect these changes had no effect on our individual results.

All error estimates discussed in connection with visual polarization measurements below refer to those expected from photon statistics alone and do not take into account any systematic error. We have, however, attempted

to take into careful account any linear polarization due to the instrument itself by measurement of unpolarized standard stars. The polarizations listed below have had the instrumental polarization removed by observations of several unpolarized standard stars (from the list of Dr. T. D. Kinman of K.P.N.O.) which were of sufficient faintness to be observed with the 4 meter telescope.

In order to measure the magnetic field structure of the clouds we need to know the position angle of linear polarization of individual stars to about $\pm 10°$. The uncertainty in the position angle, $\varepsilon(\theta)$, is given by

$$\varepsilon(\theta) = 28.6° \left[\frac{\varepsilon(P)}{P} \right] \qquad (4.1)$$

where $\varepsilon(P)$ is the uncertainty in the polarization and P is the polarization. From equation (4.1) it can be seen that to achieve $\varepsilon(\theta) = \pm 10°$ requires varying degrees of precision in $\varepsilon(P)$ depending upon P. Thus, we have made no attempt to measure stars to a given $\varepsilon(P)$.

The polarization position angles used in this work refer to the equatorial coordinate system with North being at zero degrees and position angle increasing West of North. The zero-point of position angle of our system was calibrated by the observation of several highly polarized standard stars (also from the list of Dr. T. Kinman).

We were also able to obtain estimates of the
foreground absorption to a significant fraction of the back-
ground stars by measurement of near infrared colors. This
allowed us to form P/A ratios for these stars and thus to
better ascertain the nature of the polarization mechanism.
Finally, we obtained 2.2μm linear polarimetry of several of
the Ophiuchus embedded sources in order to measure the B
field structure deep within the cloud.

4.1   Rho Ophiuchi Dark Cloud

4.1.1   Visual Polarization Observations

There is no way to select stars which one knows a
priori are background to dark cloud material. We can only
adopt selection criteria which minimize the number of fore-
ground interlopers. We chose two criteria:

1. The stars must be seen through (or against) at least
   some dark material. The reason for this criterion
   is obvious, as otherwise the star would not be
   polarized by the field of the dark cloud.

2. The stars must lie in a limited range of apparent
   visual magnitudes ($10 \leq m_v \leq 16$). Stars brighter
   than the upper brightness limit (chose by inspection
   of the brightness distribution of field stars) are
   most likely to be foreground stars for clouds in the
   distance range encompassed by our sample. (Also,

stars much brighter than $m_V \simeq 10$ could be damaging

to the photoelectric detector at the focus of the

4 meter telescope.) Stars fainter than the lower

brightness limit could not be observed in a

reasonable time.

The stars selected for observation were chosen by

Mr. M. S. Snowden of K.P.N.O. by inspection of the POSS red

photograph. Accurate coordinates for each of the selected

stars were obtained by measurement of the star's position

on the POSS red plate on the two-coordinate Grant measuring

engine of K.P.N.O.

Table 4.1 lists the results of the measurements of

stars behind the Ophiuchus cloud. The columns list, in

succession, a star identification number, the linear polari-

zation in percent, the computed error in polarization,

position angle of polarization, and the error in position

angle as computed from equation (4.1). Figures 4.1 and 4.2

display the polarization results (for the western and

eastern portions of the cloud respectively) inscribed over

a print of the POSS red photograph. In these figures the

length of the lines is proportional to the amount of

polarization, and they are oriented in the direction of

polarization position angle. The numbers in these figures

refer to the identification numbers of table 4.1. These

figures may be used for identification of the stars observed

Table 4.1. Ophiuchus background star polarizations

I. D. Number	P(%)	ε_P(%)	θ(°)	ε_θ(°)
1	0.19	0.20	24	5
2	0.34	0.05	116	4
3	1.00	0.19	30	5
4	2.07	0.38	34	5
5a	0.68	–	150	–
6	1.00	0.03	155	1
7	0.52	0.31	123	17
8	2.91	0.53	63	5
9	0.52	0.07	171	4
10	4.26	0.20	176	1
11	0.18	0.25	37	41
12	4.19	0.38	136	3
13	0.30	0.04	39	4
14	1.10	0.10	158	3
15	5.11	0.26	146	2
16	6.32	0.54	42	2
17	0.95	0.30	160	9
18	0.54	0.29	139	15
19	0.53	0.03	40	2
20	3.11	0.31	38	3
21	2.23	0.09	38	1
22	3.50	0.66	32	5
23	1.92	0.51	162	8
24	3.70	0.12	38	1
25	2.83	0.27	13	3
26b	7.54	0.47	24	2
27	3.78	0.10	39	1
28	1.03	0.06	23	2
29	0.85	0.06	53	2
30	0.68	0.31	45	13
31	2.49	0.17	20	2
32	1.87	0.26	15	4
33	0.14	0.11	65	22
34	5.23	0.42	56	2
35	7.09	0.26	52	1

Table 4.1--<u>Continued</u>. Ophiuchus background

I. D. Number	P(%)	ε_P(%)	θ(°)	ε_θ(°)
36	3.62	0.16	38	1
37	5.17	0.51	42	3
38	6.33	0.82	106	4
39	5.30	0.50	103	3
40	5.12	0.33	31	2
41	4.89	0.28	58	2
42	4.57	0.13	60	1
43	2.67	0.09	51	1
44	0.13	0.06	55	14
45	0.76	0.02	88	1
46	3.15	0.10	65	1
47	7.69	0.58	44	2
48	2.80	0.50	48	5
49	3.22	0.05	21	1
50	1.92	0.03	47	1
51	0.01	0.15	128	429
52	4.46	0.23	16	1
53	2.36	0.12	68	1
54	4.30	0.53	16	4
55	4.67	0.31	16	2
56	1.17	0.14	87	3
57	2.53	0.52	106	6
58	1.33	0.34	90	7
59	0.60	0.36	2	17
60	0.24	0.30	109	36
61	3.69	0.31	82	2
62	1.25	0.50	65	11
63	0.50	0.26	57	15
64	0.31	0.09	35	8
65	8.67	0.50	52	2
66	2.39	0.14	61	2
67	1.89	0.15	67	2
68	1.86	0.08	36	1
69	2.00	0.07	44	1
70	5.76	0.64	108	3

Table 4.1--Continued. Ophiuchus background

I. D. Number	P(%)	ε_P(%)	θ(°)	ε_θ(°)
71	0.28	0.02	17	2
72	0.18	0.11	84	17
73	4.12	0.19	65	1
74	7.44	0.48	59	2
75	1.25	0.04	90	1
76	5.92	0.40	1	2
77	0.17	0.03	70	5
78	4.80	1.30	64	8
79	5.00	0.60	63	3
80	3.65	0.05	57	1
81	4.53	0.08	66	1
82	2.65	0.02	163	1
83	7.48	0.74	132	3
84	5.28	0.45	142	2
85	2.65	0.10	44	1
86	5.56	0.50	48	2
87	4.35	0.14	150	1
88	1.22	0.22	90	4
89	0.21	0.11	63	15
90	1.12	0.03	72	1
91	3.65	0.34	46	3
92c	4.06	0.10	172	1
93d	4.93	0.26	179	2
94	4.86	0.23	139	2
95	5.28	0.26	153	2
96	3.64	0.61	156	5
97	2.29	0.08	5	2
98	5.27	0.45	53	2
99	3.52	0.19	59	1
100	3.35	0.63	68	4
101	3.34	0.89	56	7
102	6.82	0.40	58	2
103	0.66	0.32	100	12
104	5.22	0.32	59	1
105	4.14	0.22	59	1

Table 4.1--Continued. Ophiuchus background

I. D. Number	P(%)	ε_P(%)	θ(°)	ε_θ(°)
106	8.51	0.28	56	1
107	4.16	0.76	49	5
108	0.50	0.07	70	2
109	6.65	0.70	60	3
110	9.84	0.40	46	1
111	9.73	0.40	55	1
112	11.05	2.40	22	6
113	5.65	0.55	57	3
114	4.59	0.51	52	3
115	3.51	0.39	46	3
116	4.13	0.34	52	2
117	3.96	0.43	57	3
118	3.64	0.69	42	5
119	7.44	1.00	58	4
120	3.90	0.80	51	6
121	2.74	0.30	17	4
122	2.48	0.13	169	2
123	1.14	0.45	42	11
124	2.91	0.53	63	5
125	4.37	0.07	60	1
126	1.61	0.07	96	8
127a	4.10	–	176	–
128a	2.70	–	50	–
129a	3.10	–	60	–
130a	3.70	–	55	–

a. from Carrasco, Strom, and Strom (1973)

b. source 1, Grasdalen, Strom, and Strom (1973)

c. No. 3 from list of Struve and Rudkjøbing (1949)

d. No. 21 from list of Dolidze and Arakelyan (1959)

Figure 4.1.   Polarization data for the western region of the
              Ophiuchus cloud.

              The polarization data of table 4.1 presented in
              pictorial form on a POSS red photograph of the
              western region of the Ophiuchus dark cloud.
              The numbers represent the identification numbers
              in table 4.1. The lines are in the direction of
              polarization of the stars indicated and their
              lengths are proportional to the amount of linear
              polarization. Circled stars have no significant
              polarization, while those with number only did
              not have statistically significant measurements
              obtained (see text).
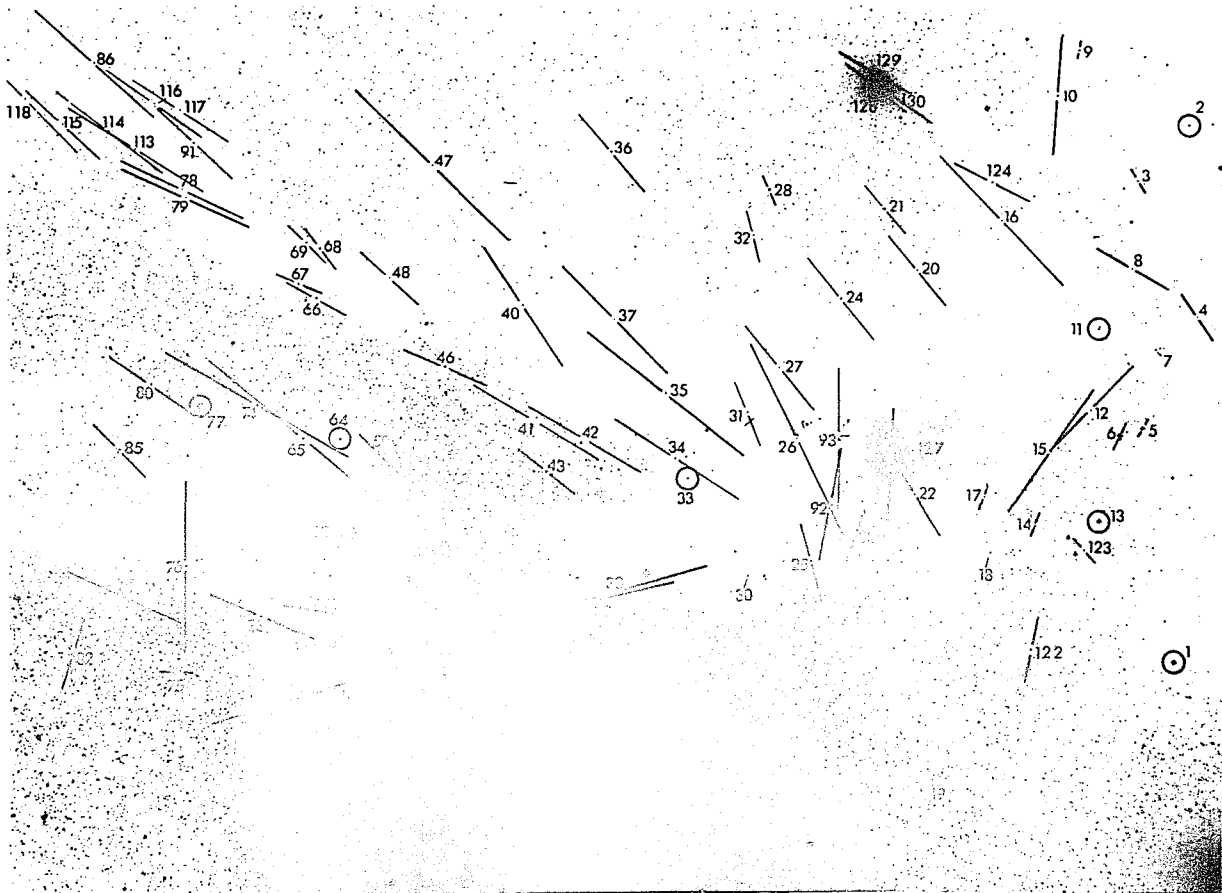
Figure 4.1. Polarization data for the western region of the Ophiuchus cloud.

Figure 4.2. Polarization data for the eastern region of the Ophiuchus cloud.

The polarization data of table 4.1 presented in pictorial form on a POSS red photograph of the eastern region of the Ophiuchus dark cloud. (See the caption of figure 4.1 and text.)
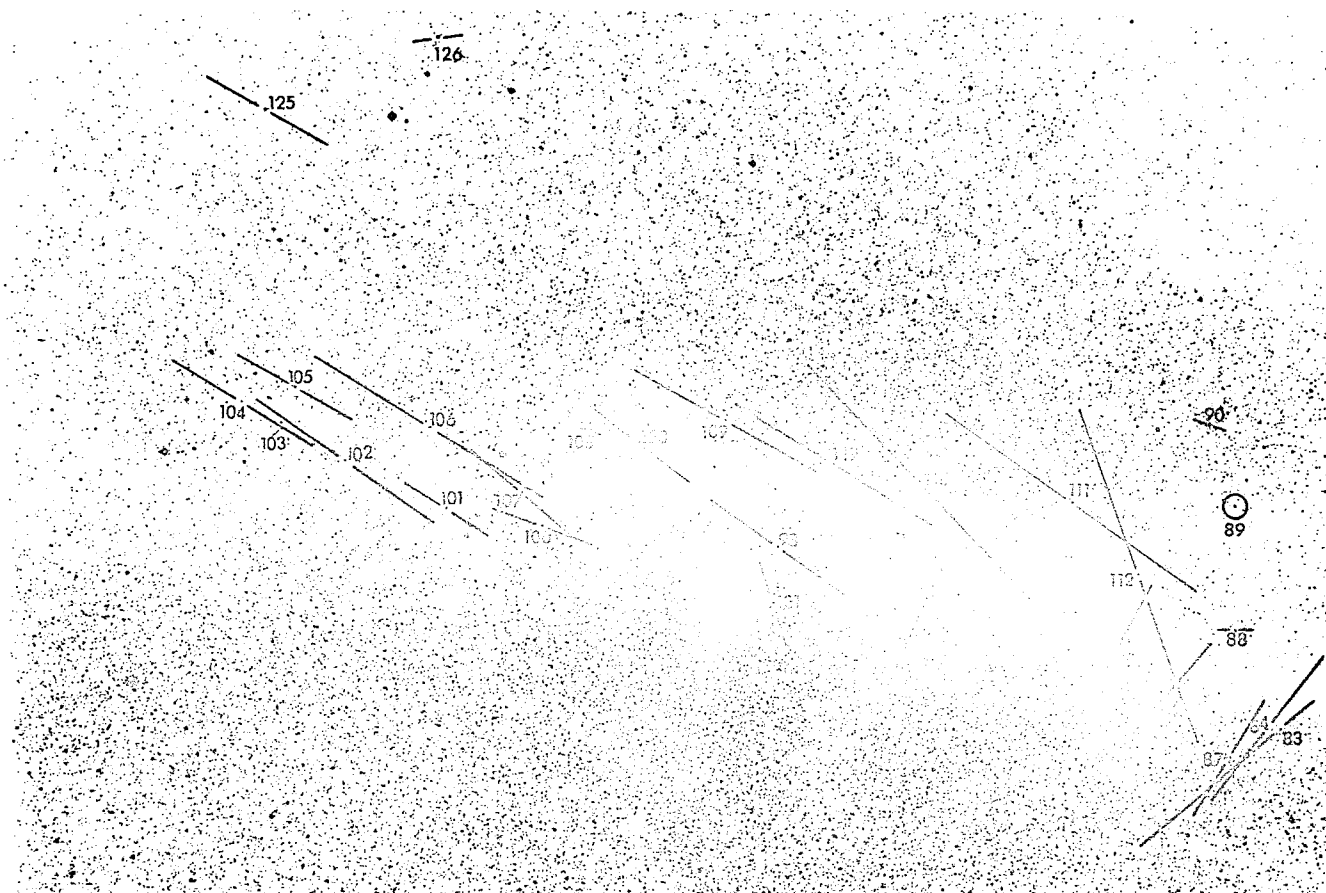
Figure 4.2.   Polarization data for the eastern region of the Ophiuchus cloud.

since the polarization vectors are open in the middle and point to the stars. Three classes of observed stars may be noted in these figures: (1) stars which have polarization vectors drawn--these stars have polarizations larger than 0.50 percent and the results are at least to the $3(\varepsilon_p)$ level (i.e., approximately $\pm 10°$); (2) stars which are encircled-- stars which have polarization less than 0.50 percent which has been measured at least to the $3(\varepsilon_p)$ level; and (3) stars which are identified only by a number--the observational errors preclude assignment of a polarization value to better than the $3(\varepsilon_p)$ error level.

Figure 4.3 is a summary of the information contained in figures 4.1 and 4.2 overlaid upon a POSS red photograph of the entire cloud region. This figure is intended to give the reader an overview of the polarization structure for the entire cloud.

4.1.2 Polarization to Absorption Ratios

It is impossible to know with absolute certainty that all of the polarization values measured in section 4.1.1 result from traversal of starlight through dark cloud grains aligned by a magnetic field. Two points, however, lead one to believe that this is generally the case. First, the background stars are general field stars, a large majority of which are on the main sequence. Very few of these stars will have intrinsic polarizations (or infrared

Figure 4.3.   Complete Ophiuchus polarization data.

A combination of the data presented
in figure 4.1 and 4.2 superimposed
over a POSS red photograph. The
symbols have the same meaning as
those described in figure 4.1 and
in the text.

Figure 4.3.   Complete Ophiuchus polarization data.

excesses) due to circumstellar shells. Secondly, we know of no mechanism other than paramagnetic relaxation that is capable of producing grain alignment over as large a distance as even a few parsecs (the size of our clouds). Thus, we believe that the most likely mechanism for producing the observed polarization is no different from that operating throughout the general interstellar medium.

There is, however, one check which can be made upon this conclusion. As discussed in chapter 1, many authors, beginning with Hiltner (1956), have pointed out that the ratio of the amount of polarization, p, to the amount of visual extinction, A_v, both in magnitudes, has a maximum value of .065, equation (1.5), (or a maximum value of 3.0 when P is in percentage and A_v is in magnitudes). If we can form this ratio for a significant fraction of the stars for which we have obtained polarization data, we can determine whether or not they fall within the bounds predicted by paramagnetic alignment of interstellar grains.

The polarizations for Ophiuchus were obtained with an unfiltered S-20 photocathode which has an effective wavelength of about 5000 Å and a bandpass of about 1000 Å. The effective wavelength is thus near that of a V filter. Furthermore, the wavelength of maximum polarization for a given ratio of total to relative absorption given by equation (1.5) is about 5000 Å for R = 3.1 (typical for the

general interstellar medium) ranging to about 7000 Å for

R = 4.0 (a maximum value found by Carrasco et al. (1973) for

the interior regions of the Ophiuchus cloud). Thus, we may

make the approximation $P_{s-20} \simeq P_V$.

The most direct and therefore the most accurate

method of deriving A_V values for the stars of interest is

to determine their spectral classification (and hence the

intrinsic B-V colors), obtain B and V photometry, form the

color excesses E_{B-V}, and assume a value of R to find A_V.

We were able to obtain the necessary B and V photometry for

a large number of the background stars by use of the Kinman

photo-polarimeter at the 2.1 meter telescope of K.P.N.O.

Unfortunately, we did not have sufficient time to obtain the

necessary spectrograms ourselves. Dr. N. Sanduleak of the

Warner and Swasey Observatory, however, was kind enough to

provide us with spectral classifications for a few of the

stars. His classifications are based on two sets of objec-

tive prism plates taken with the Curtis-Schmidt telescope

at Cerro Tololo on 3-4 August, 1967. The specifications

for the two sets of plates are:

1. 4.5 prism, 580 Å/mm at Hγ, Kodak IIa-O, 11^m exp,
    0.2 mm widening;

2. 4 prism, 1000 Å/mm at Hγ, Kodak 103a-F +GG 14 filter,
    9^m exp, 0.15 mm widening.

Table 4.2 gives in order the stellar I. D. numbers from table 4.1, spectral classifications from Sanduleak, B-V colors based on the spectral classifications, the B-V colors observed, the B-V color excess, the foreground absorption, A_V, based on E(B-V) and R = 3.1, and the ratio p/A in magnitudes. Other than star no. 135 we have assumed that all stars are luminosity class V. Although Sanduleak was able to supply spectral information on many more stars than listed in table 4.2, we have included only those for which a classification to a numerical division is given. The fact that his classification plates surveyed only the brightest of the background stars is reflected in the small A_V values listed in column 6. We note the p/A ratios are all smaller than the .065 upper limit.

In order to determine A_V for the apparently fainter background stars (and therefore statistically more highly reddened), we must turn to a less direct method. The (H-K) color indices are almost independent of spectral type for normal stars earlier than type K. [(H-K) $\simeq$ -.15 for B2, (H-K) $\simeq$ +.10 for K0]. Thus, if we assumed that all of the background stars have an intrinsic (H-K) = 0.0 color, the observed infrared colors will give us A_V in the same manner as we found for the embedded sources [that is, from (H-K) $\simeq$ E(H-K), E(B-V) = 4.76 E(H-K), and A_V = 3.1 E(B-V)]. Inspection of table 4.2 shows that most of the stars are later

Table 4.2.   Ophiuchus p/A ratios from spectral
             classification

STAR I. D.	CLASS	$(B-V)_{sp}$	$(B-V)_{obs}$	E_{B-V}	A_v	p/A_v (mag)
Anon.	G8	0.74	0.82	0.08	0.25	.032
3	M6	1.72	2.59	0.87	2.70	.008
5	A2	0.06	0.66	0.60	1.86	.008
6	B9	−0.06	0.40	0.46	1.43	.015
9	K3	1.00	1.15	0.15	0.47	.024
15	M4	1.56	2.48	0.92	2.85	.039
28	G5	0.66	1.42	0.76	2.36	.009
36	M2	1.52	2.52	1.00	3.10	.025
49	G5	0.66	1.24	0.58	1.80	.039
50	B9	−0.06	1.00	1.06	3.29	.013
69	A0	0.00	1.85	1.85	5.74	.008
75	G8III	0.95	1.21	0.26	0.81	.033
87	K0	0.82	2.06	1.24	3.84	.025
90	G0	0.59	0.72	0.13	0.40	.061

than AO, which might be expected at a large distance from the galactic equator and in the direction of the galactic center ($1^{II} \simeq 354°$). Thus, our estimate of A_V from this method will be slight overestimates and the P/A ratios will be consequently overestimated as well. Estimates of A_V from the (J-K) color index are also useful, although the index is much more sensitive to the spectral type of the star. Comparison of A_V from (J-K) with A_V from (H-K) will at least tell us if the assumed reddening law is reasonable and will disclose stars with circumstellar shells.

Table 4.3 gives in order the stellar I. D. numbers from table 4.1, J, H, and K magnitudes, A_V from (H-K), A_V from (J-K), and the ratio p/A in magnitudes based on the A_V derived from (H-K). Figure 4.4 displays the combined results of tables 4.2 and 4.3, wherein the polarization in percentage is plotted against the calculated foreground visual absorptions. The line P(%) = 3.0 A_V(mag) is identical to the line p(mag) = .065 A_V(mag). We notice that only three of the stars clearly do not fit the inequality P(%) $\leq$ 3.0 A_V. Each of these stars have large p/A ratios due to small and thus uncertain values of A_V. Figure 4.4, thus, is clearly consistent with grains of the dark cloud aligned by a magnetic field via the D-G mechanism.

The spatial distribution of p/A over the face of the cloud is shown in figure 4.5, where we have plotted

Table 4.3. Ophiuchus p/A ratio from infrared
          photometry

STAR I. D.	J	H	K	A_v (H-K)	A_v (J-K)	p_v/A_v (mag)
4	9.0	8.0	7.5	6.5	6.0	.007
7	9.9	9.0	8.7	3.9	4.8	.003
8	9.9	9.5	9.4	1.3	2.0	.049
10	4.2	2.7	2.2	7.3	8.0	.012
11	7.9	6.6	6.2	5.2	1.7	.001
12	10.0	9.1	8.9	2.5	4.4	.036
14	8.5	7.8	7.5	3.9	4.0	.006
15	7.3	6.0	5.5	5.7	6.4	.019
16	9.0	7.6	7.2	5.3	6.4	.026
17	10.2	9.3	8.9	5.2	5.2	.004
20	9.8	9.0	8.6	4.7	4.8	.015
21	8.8	8.2	7.9	3.9	3.6	.012
22	10.8	9.8	9.2	7.8	6.4	.010
23	9.9	8.8	8.3	6.5	6.4	.006
24	7.5	7.6	8.6	1.3	3.6	.061
25	8.9	8.0	7.7	3.9	1.2	.016
27	9.7	8.4	7.6	10.4	8.4	.008
30	11.2	10.2	9.6	0.6	1.6	.002
31	8.8	7.7	7.0	9.1	7.2	.006
34	8.6	7.2	6.5	7.9	8.4	.014
35	10.2	9.3	8.5	10.1	6.8	.015
37	10.6	9.6	9.0	7.7	6.4	.014
38	8.2	6.5	5.8	8.3	9.6	.017
39	11.1	10.5	10.2	3.9	3.6	.030
40	9.2	7.9	7.5	5.5	6.8	.020
41	10.1	9.2	8.8	5.2	5.2	.020
42	7.4	6.3	5.9	5.2	6.0	.019
46	9.1	8.2	8.0	2.6	4.4	.026
47	–	9.0	8.5	6.5	–	.026
52	10.5	9.3	9.2	2.3	5.2	.043
53	9.2	8.6	8.4	2.6	3.2	.020
54	10.3	9.3	8.9	5.2	5.6	.018
55	8.7	7.3	7.0	3.4	6.8	.029
61	10.1	9.4	9.0	5.2	4.4	.015
65	9.8	9.3	9.0	2.7	3.2	.029

Table 4.3--<u>Continued</u>. Ophiuchus p/A ratio from IR

STAR I. D.	J	H	K	A_v (H-K)	A_v (J-K)	p_v/A_v (mag)
66	8.7	7.7	7.4	3.9	5.2	.013
73	7.9	6.8	6.4	4.6	6.0	.019
74	9.6	8.7	8.5	1.8	4.4	.089
76	10.0	9.5	9.2	3.5	3.2	.037
78	10.3	8.9	8.1	10.1	8.8	.010
79	10.2	9.3	8.6	8.6	6.4	.013
80	8.9	8.2	7.8	5.2	4.4	.020
81	7.9	6.9	6.7	2.2	4.8	.045
83	10.7	9.8	8.8	11.8	7.6	.013
85	7.8	6.8	6.5	3.9	5.2	.015
86	10.2	9.4	8.6	10.1	6.4	.012
87	6.1	5.1	4.8	4.0	5.2	.023
95	10.4	10.1	9.2	8.8	4.8	.012
96	7.5	6.6	6.2	5.1	5.2	.016
98	7.4	6.1	5.6	6.9	7.2	.016
100	8.9	7.7	7.3	5.2	6.4	.014
101	10.4	9.4	9.0	1.3	5.6	.056
102	9.9	9.0	9.1	1.0	3.2	.150
104	-	10.0	9.8	3.4	-	.033
105	8.9	8.1	7.9	2.6	4.0	.035
106	9.1	8.3	8.2	1.0	3.6	.180
107	10.6	9.4	9.0	5.2	6.4	.017
109	8.7	7.5	7.2	3.9	6.0	.037
111	8.5	7.3	6.9	5.2	6.4	.041
112	-	10.0	9.7	4.2	-	.057
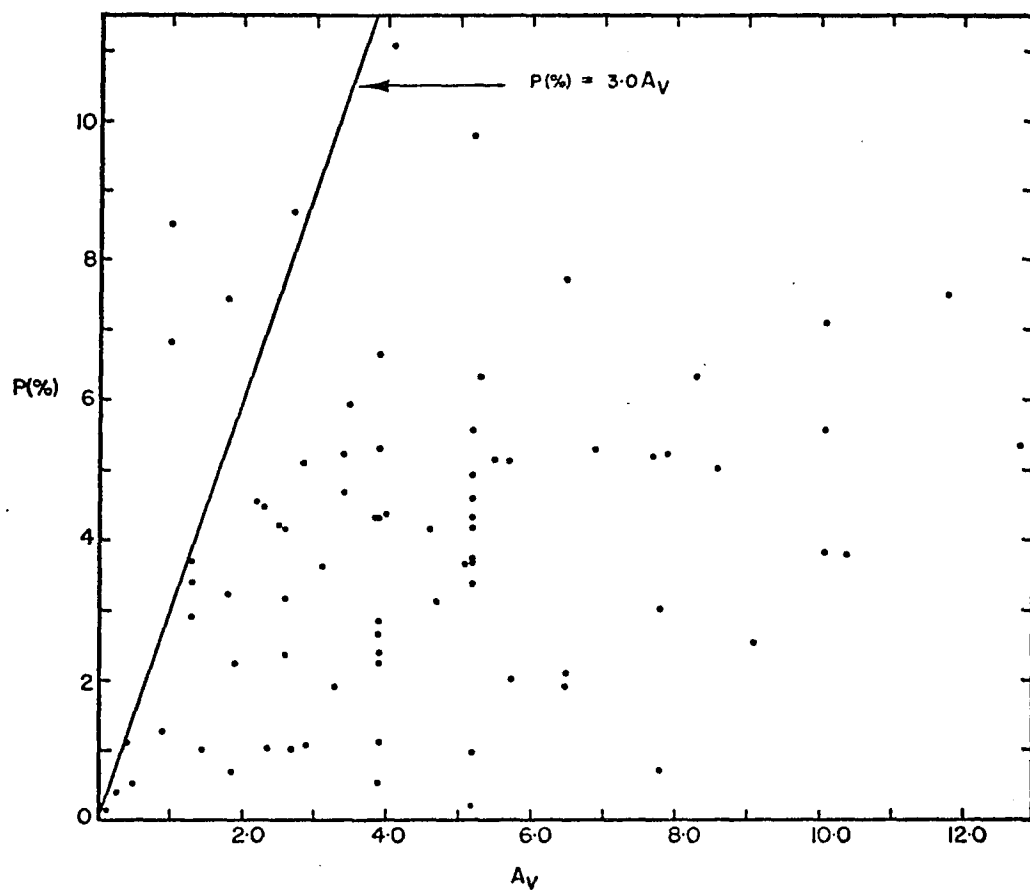
Figure 4.4.   Polarization versus absorption of
             Ophiuchus background stars.

             The combined results of tables 4.2 and
             4.3 are displayed as polarization in
             percentage plotted against computed
             visual absorption in magnitudes. The
             line P(%) = 3.0 A_V is equivalent to
             the line p(mag) = .065 A_V (mag).

Figure 4.5. Polarization to absorption ratios of Ophiuchus background stars.

Circles have been plotted around stars whose diameters represent
one of three p/A ratio ranges: smallest circles .000 - .020,
medium circles .020 - .040, and largest circles .040 and larger.
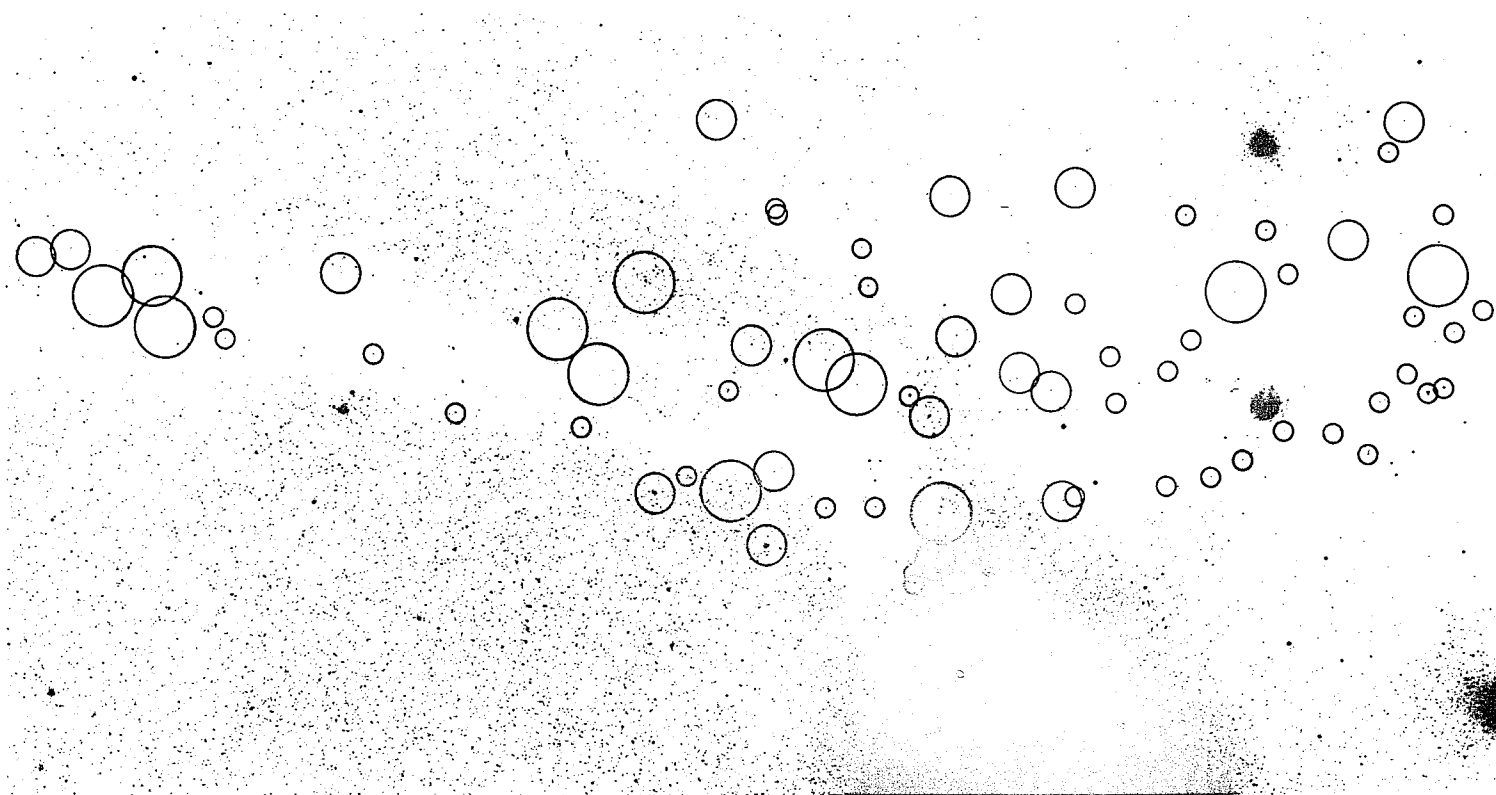
Figure 4.5. Polarization to absorption ratios of Ophiuchus background stars.

around each star a circle, whose diameter represents one of three p/A ratio ranges: smallest circles .000 - .020, medium circles .020 - .040, and largest circles .040 and larger. It can be seen that the smallest p/A ratios systematically occur in the western portion of the cloud where the main mass and embedded IR point sources are located. It also should be noted that the two large and two medium size circles in this region represent p/A ratios whose values barely place them in their respective categories.

The p/A values seen along the long arms extending to the northeast from the main body of the cloud are as large as the maximum values of p/A seen in the general interstellar medium.

From tables 4.2 and 4.3 it can be seen that we have penetrated only the first few magnitudes of cloud material, which is a natural consequence of the choice to observe background stars which are visible through the edges of the cloud. In spite of this, we can investigate variations in grain alignment as we penetrate denser regions of the cloud.

Figure 4.6 is a plot of the p/A ratio (in magnitudes) versus the calculated foreground absorption. p/A appears to decrease rapidly as we approach the denser cloud region.
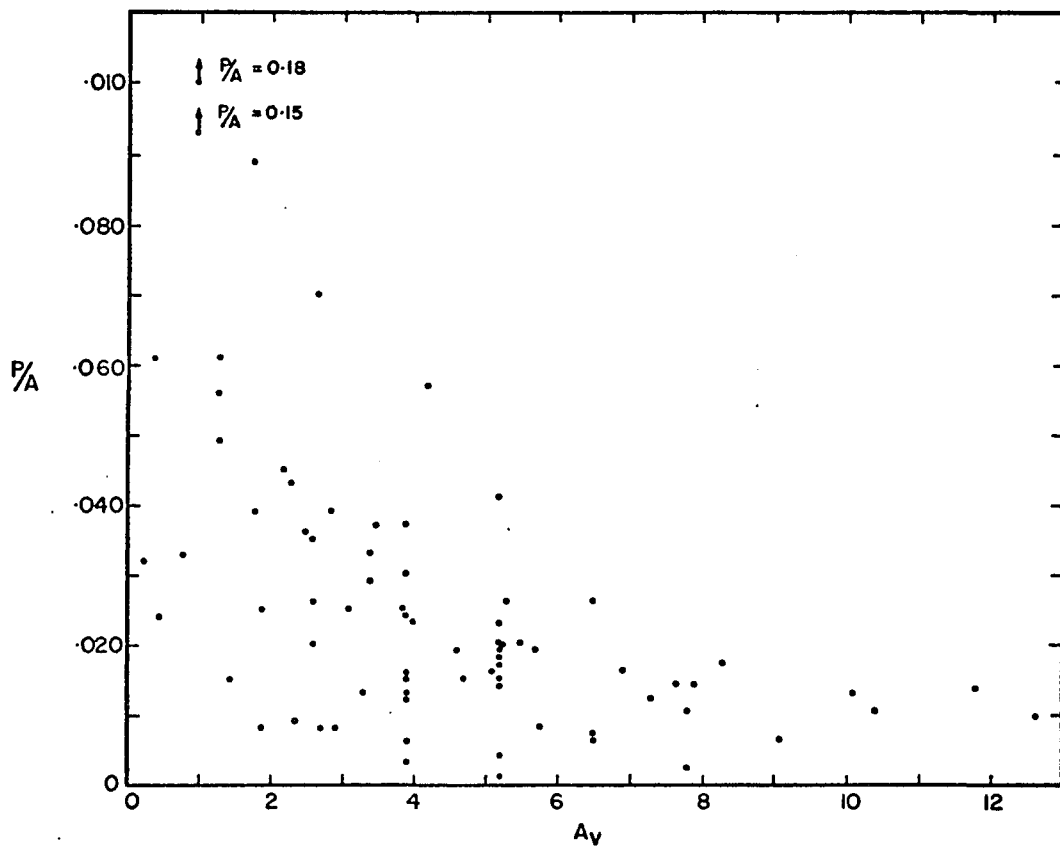
Figure 4.6. p/A$_v$ versus A$_v$ for Ophiuchus background stars.

A plot of p/A (in magnitudes) versus computed A$_v$ for the stars listed in tables 4.2 and 4.3. Two stars which have p/A of 0.15 and 0.18 respectively do not fit on the graph and are so indicated.

4.1.3 Infrared Polarization Measurements

In order to deduce the magnetic field structure deep within the cloud where star formation is taking place, we have made 2.2μm polarimetric observations of several of the brighter embedded sources. To obtain these observations we used Polaroid "HR" polarizer which was rotatable to eight thumbwheel positions and placed before the InSb detector at the focus of the 1.3 meter telescope at K.P.N.O. The instrumental polarizations were taken into account by measuring several unpolarized standard stars. The zero point of position angles was calibrated both by observing the highly polarized infrared source NML Cygnus and by observing unpolarized standard stars with an identical piece of "HR" polaroid placed over the light baffle of the telescope.

We were only able to observe those sources with K $\leq$ 7.5 in a reasonable observing period at the 1.3 meter telescope. In table 4.4 we list in order the source name, 2.2μm polarization, polarization error bars, position angle, position angle errors, computed foreground absorption, and resultant p_V/A_V ratio in magnitudes. In computing p_V we have assumed that ratio of $p_V/p_{2.2\mu m}$ observed for HD 147889-- where we have the visual polarization measurement of HD 147889 of Carrasco et al. (1973)--applies to all IR sources. The resultant p/A ratios are very small.

Table 4.4. 2.2 micron polarimetry of embedded sources

Source	$P(\%)$	$\varepsilon_P(\%)$	$\theta(°)$	$\varepsilon_\theta(°)$	$A_v(mag)$	p_v/A_v
HD 147889	1.41	.38	162	8	3^c	.010
Source 1^a	2.28	.55	33	7	12	.004
Source 2^a	3.83	.64	3	5	22	.004
Source 3^a	4.28	1.27	55	8	16	.006
Source 4^a	1.66	.83	45	14	12	.003
DO-AR-24E	1.09	.46	176	12	–	–
Source 16^a	.40	.48	52	34	15	.000
16^b	1.83	.38	46	6	7	.006
13^b	3.32	1.30	73	11	14	.005

a. refers to source numbers in the list of
    Grasdalen et al. (1973)

b. refers to identification numbers in table 4.1

c. A_v from Carrasco et al. (1973)

In figure 4.7 is shown the same POSS red photograph
as seen in figure 3.1. Inscribed on this photograph are
lines whose lengths are proportional to the 2.2μm polariza-
tion and which are drawn in the direction of polarization
position angle. The circle represents the unpolarized
source number 16 from the list of Grasdalen et al. (1973).
Although there is considerable uncertainty in the position
angles, it can be seen that they tend to lie in one of two
directions: about 0° or 50°. This is simmilar to the pat-
tern seen in visual polarized light from the background
stars and shows that the background stars provide an accu-
rate picture of the magnetic field pattern deep within the
cloud.

4.2 M78 Dark Cloud

4.2.1 Visual Polarization Observations

The results of the visual linear polarization obser-
vation of stars background to the Lynds 1630 cloud are
listed in table 4.5 where we have listed an identification
number, percentage of linear polarization, uncertainty in
polarization, polarization position angle, and uncertainty
in position angle. Those results are also graphically dis-
played in figure 4.8 where we have drawn, for all stars
displaying 3 sigma polarizations of 0.50 percent or larger,
lines whose lengths are proportional to the polarization
amount and drawn in the direction of polarization. Stars

Figure 4.7. Infrared polarization of Ophiuchus embedded sources.

The results of table 4.4 shown on the same POSS red
photograph as in figure 3.1. The line lengths are
proportional to the amount of 2.2µm linear polari-
zation and are drawn in the same direction as the
polarization position angle. The circled source
represents the unpolarized source 16 of Grasdalen
et al. (1973). It should be noted that the line
to the northwest of the ^{12}CO emission peak is due
to an asteroid.
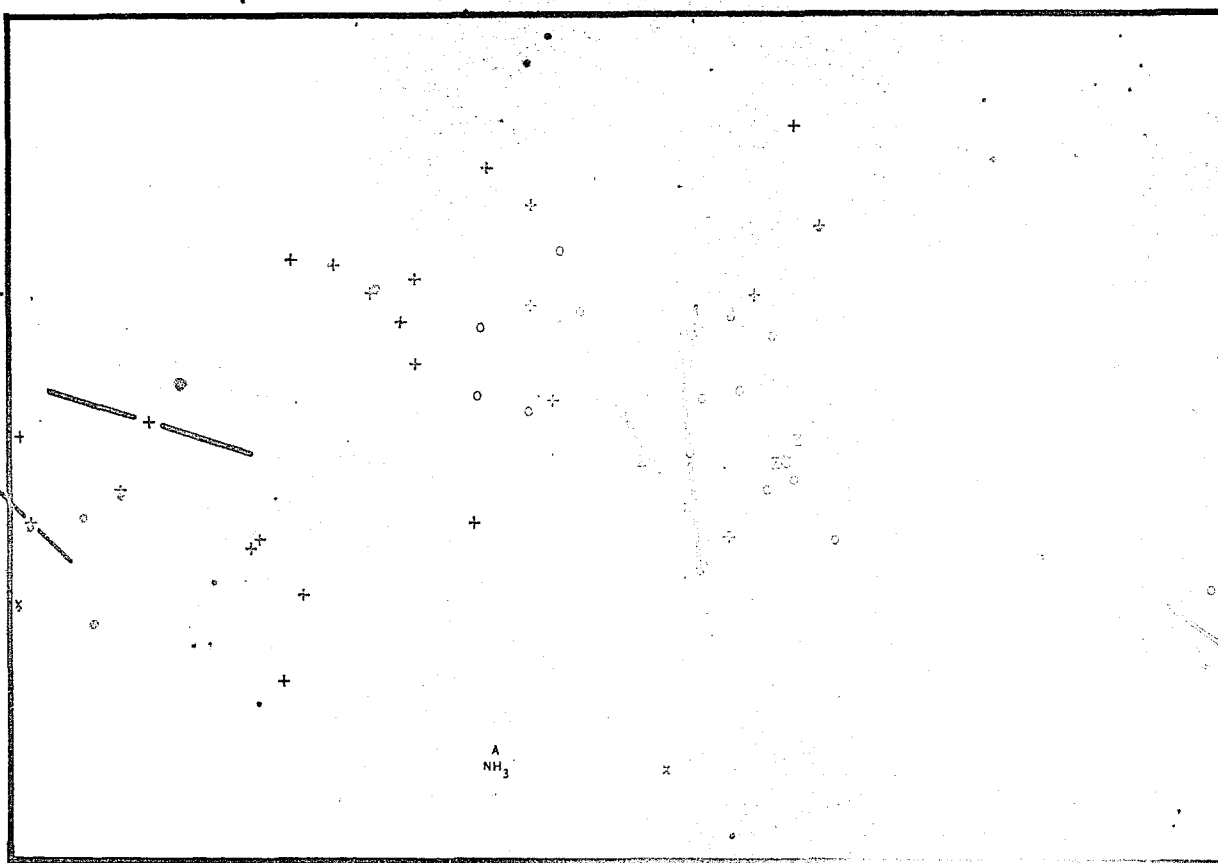
Figure 4.7. Infrared polarization of Ophiuchus embedded sources.

Table 4.5. M78 background star polarizations

I. D. Number	P(%)	ε_P(%)	θ(°)	ε_θ(°)
1	0.20	0.04	179	6
2	1.85	0.08	4	1
3	0.12	0.16	61	38
4	0.17	0.19	168	32
5	0.12	0.15	144	36
6	2.85	0.24	63	2
7	5.11	0.49	6	3
8	0.07	0.05	1	22
9	4.68	0.21	0	1
10	0.21	0.34	33	46
11	0.50	0.30	65	17
12	0.40	0.46	58	33
13	0.98	0.31	32	10
14	0.25	0.33	165	37
15	4.76	0.26	162	2
16	0.26	0.26	36	28
17	2.98	0.42	170	4
18	0.45	0.64	141	42
19	2.29	0.45	109	6
20	0.08	0.09	122	30
21	0.33	0.36	100	31
22	0.65	0.14	31	6
23	3.09	0.44	105	4
24	0.62	0.47	125	22
25	0.41	0.25	114	18

Table 4.5--<u>Continued</u>. M78 background

I. D. Number	P(%)	$\varepsilon_P(\%)$	$\theta(°)$	$\varepsilon_\theta(°)$
26	0.32	0.17	107	15
27	2.96	0.55	85	5
28	1.09	0.58	65	15
29	0.52	0.47	118	26
30	0.46	0.35	132	22
31	2.43	0.34	25	4
32	0.22	0.41	13	52
33	0.39	0.28	14	20
34	0.64	0.26	36	11
35	1.21	0.28	123	6
36	0.40	0.24	56	17
37	2.51	0.59	88	7

Figure 4.8.   The optical polarization results for the
              Lynds 1630 cloud displayed graphically.

              The numbered stars refer to the identifi-
              cation numbers in talbe 4.5.   (See text
              for further explanation.)

Figure 4.8. The optical polarization results
for the Lynds 1630 cloud displayed
graphically.

with polarizations less than 0.50 percent are encircled, and those for which statistically meaningful observations were not obtained are merely numbered. All observations were carried out with the same equipment used for the Ophiuchus cloud.

4.2.2 Polarization to Absorption Ratios

Although we have not made any systematic effort to investigate polarization to absorption ratios for this cloud, several of the background polarization stars correspond to sources detected in the infrared survey which have visual absorption estimates in table 3.1. The polarization to absorption ratios deduced in this way are listed in table 4.6. The p/A ratios are very small and certainly not in conflict with the polarizations expected from grains aligned by a magnetic field.

4.3 Corona Austrina Dark Cloud

4.3.1 Visual Polarization Observations

The stars background to the Corona Austrina dark cloud used for visual polarization observations were chosen in a manner similar to those for the Ophiuchus cloud, and all observations were carried out with the same equipment. The results are presented in table 4.7 where we have listed an identification number, linear polarization, polarization uncertainty, polarization position angle, and position

Table 4.6.   Lynds 1630 polarization to absorption
             ratios

Polarization Star I. D. Number	A_V(mag)	p_V(mag)	p_V/A_V(mag)
1	4	.004	.001
3	7	.003	.0004
4	10	.004	.0004
19	12	.049	.004
23	17	.006	.004
36	3	.008	.002

Table 4.7. Optical polarizations of Corona
            Austrina background stars

I. D. Number	P(%)	ε_P(%)	θ(°)	ε_θ(°)
1	0.03	0.16	17	152
2	0.79	0.14	5	5
3	0.78	0.53	14	19
4	2.44	0.40	11	5
5	1.97	0.77	154	11
6	2.83	0.24	116	2
7	0.45	0.36	10	23
8	0.38	0.27	33	20
9	0.17	0.65	76	109
10	1.45	0.06	157	1
11	0.77	0.40	112	15
12	1.22	0.11	171	3
13	1.81	0.17	95	3
14	2.66	0.18	102	2
15	2.04	0.17	105	2
16	0.72	0.15	96	6
17	0.42	0.39	122	27
18	3.27	0.38	94	3
19	0.54	0.27	112	14
20	1.49	0.29	91	6
21	1.48	0.38	103	7
22	1.40	0.10	88	2
23	1.10	0.33	100	9
24	0.47	0.27	6	16
25	1.19	0.18	30	4
26	0.84	0.46	98	16
27	0.31	0.18	131	17
28	2.32	0.06	148	1
29	0.46	0.13	119	8
30	1.32	0.07	126	2

Table 4.7--<u>Continued</u>.   Corona Austrina background

I. D. Number	P(%)	ε_P(%)	θ(°)	ε_θ(°)
31	1.65	0.21	156	4
32	1.73	0.25	98	4
33	0.64	0.89	117	40
34	0.88	0.11	98	4
35	0.85	0.34	51	11
36	1.19	0.12	49	2
37	0.88	0.08	57	3
38	0.52	0.17	68	9
39	0.55	0.84	173	43
40	0.55	0.07	50	4
41	3.12	0.35	46	3
42	2.08	1.79	127	25
43	1.06	0.03	54	1
44	0.94	0.03	73	1
45	1.76	0.37	60	6
46	2.03	0.17	29	3
47	0.37	0.06	129	6
48	2.63	0.27	51	3
49	0.53	0.05	137	2
50	1.07	0.09	175	2
51	2.52	0.50	70	6
52	1.78	0.17	30	3
53	3.00	0.91	63	9
54	1.97	0.13	80	2
55	1.61	0.19	49	4
56	1.68	0.09	74	2
57	1.46	0.23	167	4
58	1.32	0.13	162	3
59	1.16	0.12	147	3
60	0.49	0.08	29	5

Table 4.7--<u>Continued</u>.   Corona Austrina background

I. D. Number	P(%)	ε_P(%)	θ(°)	ε_θ(°)
61	0.34	0.11	173	8
62	0.99	0.05	180	1
63	0.27	0.05	114	5
64	0.33	0.41	169	30
65	1.00	0.06	120	2
66	0.90	0.07	110	2
67	0.79	0.04	102	1
68	3.09	0.05	69	1
69	0.47	0.05	40	4
70	0.31	0.07	79	7
71	0.98	0.18	58	6
72	1.37	0.15	82	3
73	1.66	0.21	81	4
74	0.68	0.23	71	11
75	1.67	0.40	103	7
76	1.18	0.12	63	3

uncertainty. The results are also displayed graphically in
figure 4.9 where we have drawn lines proportional to the
amount of polarization and in the direction of polarization
for all observed stars with 3 sigma polarization of 0.5 per-
cent or larger. Stars with polarization less than 0.5
percent are encircled, while those for which statistically
significant observations were not obtained are merely num-
bered. The identification numbers refer to those of table
4.7. We had no opportunity to obtain polarization to
absorption ratio information. Figure 4.9 shows that the
field pattern closely follows the outline of the dark cloud
material.

4.4 NGC 1333 Dark Cloud

4.4.1 Visual Polarization Observations

The stars background to NGC 1333 chosen for visual
linear polarization measurements are listed according to
identification numbers in table 4.8 where we also list the
polarizations, polarization uncertainty, position angle of
polarization, and position angle uncertainty. The measure-
ments were obtained with the same equipment as for previ-
ously discussed clouds. The results are also displayed
graphically in figure 4.10 where we have drawn lines whose
lengths are proportional to the amount of polarization and
oriented in the direction of polarization for stars with

Figure 4.9.   The optical polarization results for the Corona Austrina
dark cloud displayed graphically.

The numbered stars refer to the identification numbers
in table 4.7.   (See text for further explanation.)
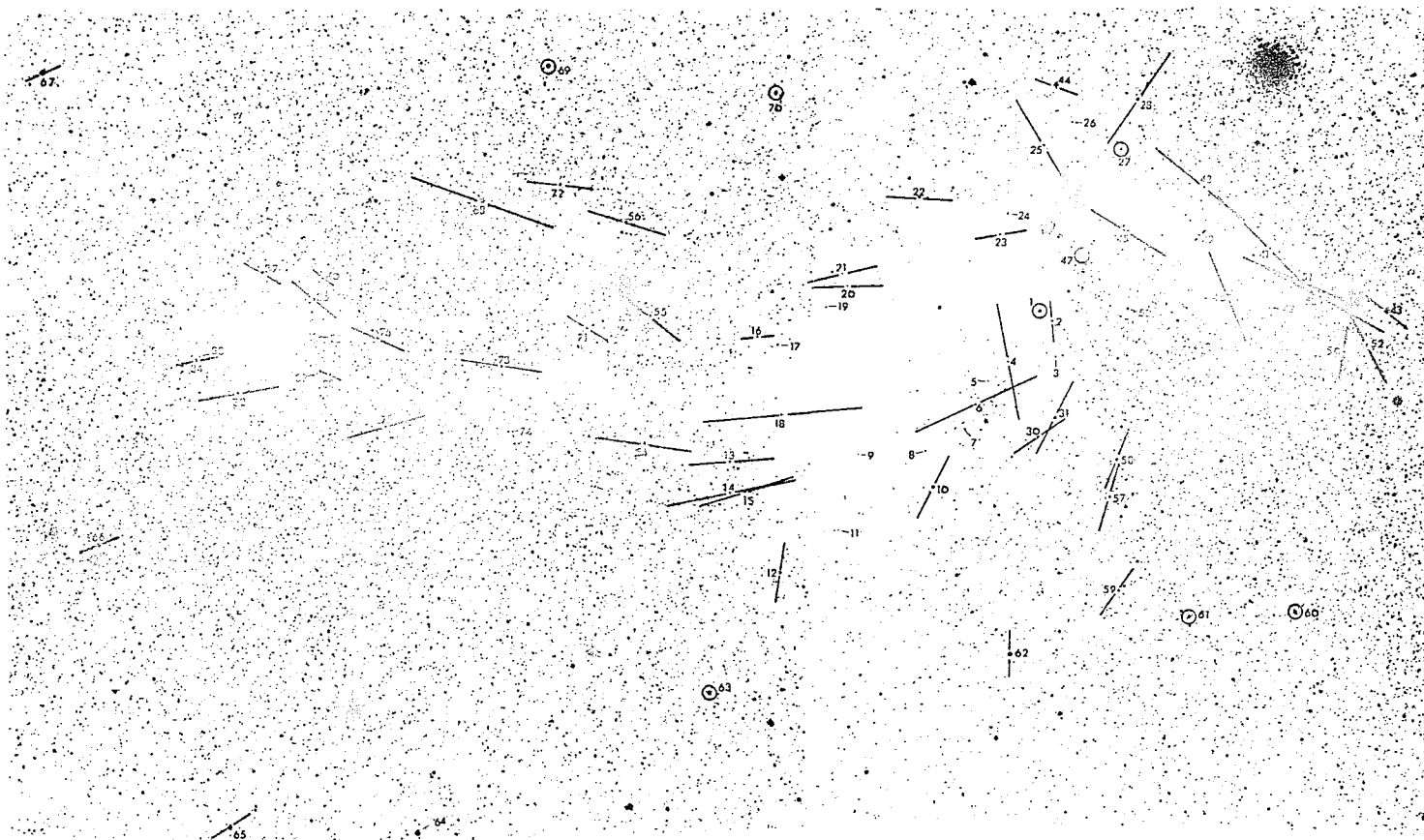
Figure 4.9. The optical polarization results for the Corona Austrina dark cloud displayed graphically.

Table 4.8. NGC 1333 background star polarizations

I. D. Number	P(%)	ε_P(%)	θ(°)	ε_θ(°)
1	1.47	0.69	91	13
2	0.96	0.57	106	17
3a	1.63	0.09	105	2
4b	2.03	0.55	95	8
5	7.02	0.65	124	3
6	1.06	0.10	55	3
7	2.33	0.60	32	7
8	0.23	0.09	14	11
9	0.98	0.05	59	1
10c	0.11	0.12	21	31
11	1.23	0.13	74	3
12	1.14	0.11	72	3
13	1.36	0.08	62	2
14	2.03	0.33	98	5
15	2.53	0.16	93	2
16	1.93	0.43	47	6
17	0.28	0.24	77	33
18	2.22	1.19	64	15
19d	1.60	0.78	103	14
20	0.64	0.54	89	24
21	1.28	0.59	106	13
22	0.11	0.64	133	166
23	1.62	0.55	27	10
24e	2.65	0.64	90	7
25f	1.41	0.79	105	16
26	1.16	0.59	44	15
27g	1.16	0.38	78	9
28	1.14	0.30	53	8
29	1.07	0.37	87	10
30	0.57	0.54	122	27
31	3.28	0.46	123	4
32	2.06	0.51	144	7
33	3.51	0.63	123	5
34	2.26	0.36	107	5
35	0.69	0.33	27	14

Table 4.8—Continued. NGC 1333 background

I. D. Number	P(%)	ε_P(%)	θ(°)	ε_θ(°)
36	0.84	0.70	23	24
37	1.18	0.29	95	7
38	1.12	0.31	67	8
39	0.32	0.31	155	28
40	1.04	0.42	114	12
41	3.49	0.48	117	4
42	1.74	0.33	128	5
43	0.58	0.38	25	19
44	2.10	0.49	128	7
45	3.51	0.26	12	2
46	3.65	0.51	153	4
47	1.60	0.73	2	13
48	5.65	0.60	176	3
49	2.46	0.47	89	6
50	0.50	0.20	78	11
51	0.78	0.37	172	14
52	1.30	0.44	91	10
53	0.09	0.34	112	112
54	0.91	0.70	115	22
55	2.18	0.32	99	4
56	2.31	0.36	102	4
57	2.69	0.19	99	2
58	4.37	0.57	127	4
59	0.49	0.27	172	16
60	2.42	0.45	155	5

a. +30 549   e. Lk Hα 351

b. Lk Hα 270   f. Lk Hα 352

c. +30 547   g. Lk Hα 271

d. Lk Hα 351

Figure 4.10. The optical polarization results for the
NGC 1333 dark cloud displayed graphically.

The numbered stars refer to the identifi-
cation numbers in table 4.8. (See text
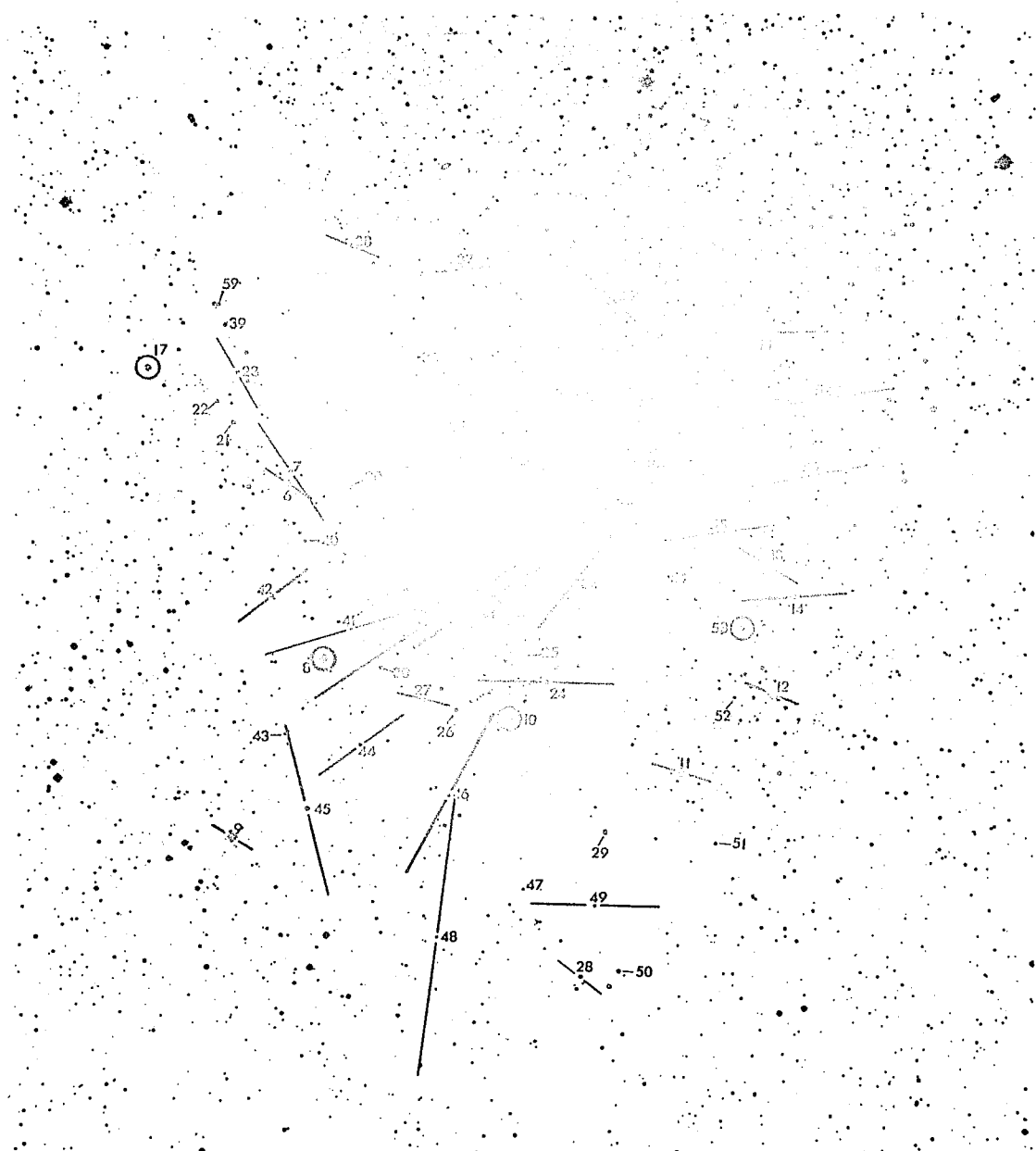for further explanation.)

Figure 4.10.   The optical polarization results for the
              NGC 1333 dark cloud displayed graphically.

3 sigma polarizations of 0.5 percent or larger. Unpolarized stars are encircled, while those with statistically insignificant measurements are merely numbered.

Several of the stars for which we obtained optical polarization measurements are associated with nebulous material from NGC 1333 or are otherwise members of strings of young objects near the center of the cloud. Although it might be expected that these objects would produce spurious magnetic field geometries due to possible intrinsic polarizations, we note that they all have approximately the same position angle of polarization, which is highly unlikely for stars strongly influenced by an intrinsic polarization component.

4.4.2 Polarization to Absorption Ratios

Again we have made no systematic effort to investigate p/A ratios for this cloud. However, we did make visual polarization measurements of a few sources detected in the 2.2μm survey of Chapter 3. Using the foreground absorptions computed in table 3.7 and the polarizations of table 4.8 we estimate the p/A ratios in table 4.9. All of these stars are located near the cloud center where the cloud could be clumpy due to fragmentation, and other depolarization effects could be important. Indeed, the p/A ratios are quite small.

Table 4.9.   NGC 1333 polarization to absorption
            ratios

Polarization I. D. Number	p_v(mag)	A_v(mag)	p/A(mag)
1	.032	4	.008
2	.021	13	.002
5	.152	11	.014
31	.071	22	.003

CHAPTER 5

INFLUENCE OF MAGNETIC FIELDS
IN CLOUD EVOLUTION

In this chapter we investigate the role of magnetic
fields in cloud evolution from the standpoints of observed
field geometries, comparison of magnetic with dynamic
pressures, and proposed scenarios for star formation. By
necessity a large fraction of this chapter will be devoted
to the Rho Ophiuchi cloud for which we have obtained p/A
ratios in addition to polarization and infrared data.

5.1 Rho Ophiuchi Cloud

5.1.1 Field Geometry and Polarization
to Absorption Ratios

The magnetic field geometry of the Rho Ophiuchi
cloud is displayed in figures 4.1, 4.2, and 4.3. The most
striking feature of these figures is the degree to which
the magnetic field aligns with the two long "streamers" of
material extending to the northeast from the main body of
the cloud. Not only are the polarizations observed through
these arms the largest seen in the cloud, but the p/A ratios
are as large as seen anywhere in the general interstellar

medium. All of these results indicate a uniform field that is aligned with the arms.

The motions of gas perpendicular to the direction of a uniform magnetic field will tend to be inhibited by the presence of the field, while motions along the field will not be affected. Thus, we cannot expect that these arms were formed by a collapse which was perpendicular to the present direction of the arms and parallel to a magnetic field perpendicular to the orientation of the arms. It is much more likely that the field-cloud alignment indicates that material is either streaming into or away from the main cloud along these arms.

In the western regions of the cloud where the majority of the mass is likely concentrated and active star formation is implied by our infrared observations, the magnetic field structure is considerably less organized. The polarization directions seem to be randomly scattered, although there is an indication that near the embedded cluster the orientation is near zero degrees. Also, in these regions the polarizations and p/A ratios are smaller than in the "streamer" regions. These facts imply that the regions of the cloud where star formation (and thus fragmentation) occurs gives small p/A ratios due to the "clumpy" nature of the material and twisted magnetic fields. It is also possible that radiation pressure and stellar winds from

the embedded stellar cluster produces grain alignment patterns which reduce the net polarization seen at the cloud boundary. However, observations by Dieter (1975) of this region of the 4830 mHz rotational line of H_2CO show a line width of $\Delta V = 1.3$ km/s, which is comparable to dust clouds with no embedded stars or stars so young as to not have had enough time to disturb the surrounding material.

As pointed out in the previous chapter, the position angles of polarization at 2.2μm of the embedded sources appear to lie in one of two directions (0° or 50°), similar to the background star position angle distribution in this area. This bimodal distribution of position angles suggests two field directions which are most likely associated with two cloud components. However, there does not appear to be any convincing relationship between polarization or position angle and total visual absorption for either the embedded or background stars. Thus, the actual cloud-field is more complicated than two overlying clouds with different magnetic field directions.

5.1.2 Scenario for Cloud Formation

Recently several authors have discussed the possibility that since young stars and dark clouds are found along spiral arms, the same mechanism responsible for producing the spiral arms triggers star formation. Lin, Yuan, and Shu (1969) developed the spiral density wave theory of

galactic structure. Roberts (1969), Shu et al. (1972), Shu, Milione, and Roberts (1973), and Woodward (1975) have shown that for moderately large amplitude stellar spiral waves, shocks develop in the interstellar medium which trace out the spiral pattern. These shock fronts could produce the compression necessary to form massive dark clouds and to initiate star formation.

Recently Woodward (1976) has been able to follow the evolution for 6×10^6 years of an essentially standard cloud of 500 $M_\odot$ immersed in an intercloud medium which is hit by a typical galactic shock at a speed of 18 km/s. The effects on the initially spherical cloud of the resultant high pressures of the intercloud medium and the dynamic pressure from the motion of the shocked gas relative to the cloud are extremely interesting, as they provide, for the first time, observational consequences available only from such a detailed two-dimensional calculation. We outline here the main points of the evolutionary history of such a cloud and its observational consequences.

As the shock front passes through the cloud, ripples appear along the edges which are amplified by a Kelvin-Helmholtz instability. At about 1.7×10^6 years the shock front has passed through the cloud. The various sections of the shock front meeting at the back of the cloud produce very high pressures there, which resist downstream motion of

cloud material and force the backside of the cloud inward.
Thus, high pressures at the front and back of the cloud
cause it to be flattened in a direction perpendicular to the
direction of shock passage. By 3×10^6 yr this flattening
has progressed far enough that the ripples caused by the
original Kelvin-Helmholtz instability can be greatly ampli-
fied by Rayleigh-Taylor instability. Thus, large amplitude
perturbations of the cloud are produced, resulting in long
tongues of dense gas projecting from the main cloud body.

Near the symmetry axis the instability grows slowly,
but has enough time before the shock front passes through
the cloud to develop. By 5.6×10^6 yr the original front
boundary of the cloud near the symmetry axis can only be
effected by one unstable mode--the largest mode which can
fit between the tongues of material which now extend from
the cloud. The result is that at this point a very dense
($\rho \simeq 10^3$ cm^{-1}) clump of material forms with a mass of about
30 to 35 $M_\odot$. At 5×10^6 yr gravitational forces in this
clump are already about one-third of the pressure forces.
The clump is about 90 percent of the way to gravitational
collapse, even though the computations did not take into
account self-gravity. Thus, with the addition of gravita-
tional forces, the model predicts that a shocked cloud of
only 500 $M_\odot$ should easily be able to produce 30-35 $M_\odot$ of
star formation.

The evolution of the cloud subsequent to 6×10^6 yr is controlled by the fact that the shock fronts coming from the back and front of the cloud very soon collide and produce two reflected shocks, between which is a dense slab of material moving at about 1 km s. However, the front shock is considerably stronger than the back shock, so that the speed of the backward reflected shock is fast. The result is that both the dense slab and the flattened main cloud are quickly accelerated downstream and away from the star formation region. Under the proper shock conditions this material will flow downstream in the form of a bow-shock with an angle from the symmetry axis of $\psi \simeq \sin^{-1}(1/M)$, where M is the Mach number. The density of this region will be of the order 1-10 cm^{-1}.

In the meantime the dense region where star formation occurs will have been essentially left untouched, although it will have been accelerated somewhat downstream. This region will, of course, begin to re-expand. However, the time scale for this to occur is 2×10^7 yr (the time necessary for it to encounter its own mass of interstellar gas), whereas the time scale for gravitational collapse will be only 4×10^6 years. Thus, star formation should be able to occur in this region.

A problem with Woodward's model is that due to the very computer-time-consuming nature of the calculations,

only one set of initial cloud parameters has been attempted
(the one listed above). Thus, it is difficult to generalize
the results of this particular calculation to other cases
where the difference in cloud mass or initial asymmetry may
be important. Woodward argues that certain features of the
calculations important for star formation will hold for
clouds of different masses, namely: the flattening of the
initially spherical cloud, the implosion and confinement of
the back part of the cloud, and the formation and gravita-
tional binding of the dense clump of star formation material
near the front surface of the cloud. It is suggested that
the shock-driven implosions of clouds more massive than
500 $M_\odot$ could be responsible for the more dramatic examples
of star formation, as the effect of greater initial masses
is to increase the mass trapped in the star formation
region.

The effects of a galactic magnetic field has been
purposefully avoided in Woodward's work due to computational
difficulties. The equipartition field strength for the
shocked intercloud gas for the computed case is 2.7×10^6
Gauss, which is comparable to estimates of the galactic mag-
netic field strength. In crudely estimating the effects of
a field parallel to the direction of the shock front
Woodward concludes that the instability will not be as
effective in clumping material in the star formation region,

but the overall picture of cloud evolution and star formation will not be changed. However, if the initial magnetic field direction is perpendicular to the shock front direction, for the high densities and for the star formation to proceed as in the computed example, the field strength would have to be significantly less than 1×10^{-6} Gauss.

Some of the most important observational consequences predicted by this model are:

1. Stars form in a small, high density region near the front edge of a much more massive cloud. Our infrared mapping has revealed an embedded cluster of young stars which occur in a high density region of small size (diameter about 2 pc) in a considerably larger cloud complex. This cluster is near the southwestern edge of the cloud complex, indicating that if indeed this cloud was struck by a shock front, the shock velocity was in a northeastward direction.

2. In order for star formation to be possible, the initial field geometry should be parallel to the shock front velocity. We have obtained polarization measurements of several background stars which are at an angular distance of one to three degrees from the cloud boundaries. These measurements show that the galactic magnetic field direction in the area

of the cloud is parallel to the cloud "streamers".
Inspection of the polarization maps of Mathewson and
Ford (1970) in this area also show the same field
direction. Thus, the ambient field direction in
this area is oriented with respect to the assumed
shock direction such that star formation should not
be greatly inhibited.

3. The area near the star formation region should
become flattened perpendicular to the shock velocity
direction. There is no direct visual evidence of
cloud elongation in this manner due to considerable
surrounding dark cloud material. However, the
polarization measurements of the area show that the
field direction is rotated almost perpendicular to
the shock velocity direction. If the magnetic field
is frozen into the cloud material and if the field
is not much stronger than the equipartition strength
during collapse, the field could be twisted into the
orientation by the cloud flattening.

4. The efficiency of star formation in the star forma-
tion region should be very high. This point will be
discussed in the next section where it will be shown
that, indeed, it is very high.

5. After about 2×10^7 years the gas left over from
star formation will be swept away. This is a

particularly attractive feature, since observations of young, open clusters show little evidence for leftover material. It is otherwise hard to understand how any gravitational collapse process could be 100 percent efficient, and Strom, Strom, and Grasdalen (1975) have pointed out that stellar winds and expanding H II regions are insufficient to clear away the remaining cloud material. It is not surprising that the Ophiuchus stars are still embedded, as their ages must not be any older than nearby OB stars in Scorpio-Centarus $(3-6 \times 10^6$ years) (Carrasco et al. 1973).

6. Some of the cloud material not used in star formation should be seen downstream in the direction of the shock. This feature of Woodward's model neatly explains the "streamers" which are oriented in the downstream direction for a shock striking the cloud from the southwest. If this is the case, we would expect that the "streamers" material will have a different radial velocity than the main part of the cloud, unless the shock velocity is in the plane of the sky. To investigate this and other mass motions of the Rho Ophiuchi cloud, we have been able to obtain $^{12}C^{16}O$ (115 GHz) radio radial velocity observations of different parts of the cloud through the

generosity of Drs. R. Loren and C. Gottlieb. These observations are summarized in table 5.1 and are displayed graphically in figure 5.1; and as they were obtained with a variety of different equipment, such equipment will not be discussed here.

Many features of radial velocity structure can be seen from this map and a further discussion of these points will be taken up in the next section. Here we will discuss only the relative motions of the "streamers" with respect to the main cloud body. The measurements of V = 2.76, 2.9 km/s show that the area of star formation has a radial velocity associated with it of about 2.8 km/s, while the northern and southern "streamers" are at approximately 1.5 and 4.6 km/s respectively. We have no way of knowing what the orientation of the streamers is in azimuth with respect to the plane of the sky. If we crudely assume that both streamers lie at a 45° azimuthal angle, the transverse component of downstream flow will be the same as the radial component. If we interpret the radial velocity differences between the star formation region and the streamers as the transverse component of the downstream flow, we can then estimate the age of the "streamers", since the transverse length of the "streamers" is the same as the radial length for an azimuthal angle of 45°. (The radial velocity measurement at 2.05 km/s is somewhat disconcerting to our interpretation of

Table 5.1. $^{12}C^{16}O$ (115 GHz) radial velocity observations of Rho Ophiuchi dark cloud

α(1950)	δ(1950)	V_{lsr}(km/s)	Obs.
16 25 58	−24 10 00	2.76 ± .05	G
16 29 33	−23 48 20	1.40 ± .05	G
16 31 00	−23 33 11	1.57 ± .05	G
16 35 11	−24 16 03	2.05 ± .03	G
16 24 15	−24 04 00	2.9 ± .3	L
16 38 20	−24 05 23	4.5 ± .3	L
16 41 45	−23 56 52	4.8 ± .3	L
16 29 10	−24 34 00	4.5 ± .3	L
16 29 10	−25 10 10	4.5 ± .3	L
16 24 13	−24 44 55	4.1 ± .3	L
16 21 02	−24 06 21	1.9 ± .3	L

Observers: G = Dr. C. Gottlieb, L = Dr. R. Loren

Figure 5.1. CO observations of Ophiuchus cloud.

The $^{12}C^{16}O$ (115 GHz) radial velocity
radio observations of Drs. C. Gottlieb
and R. Loren are plotted at their
approximate positions over a POSS red
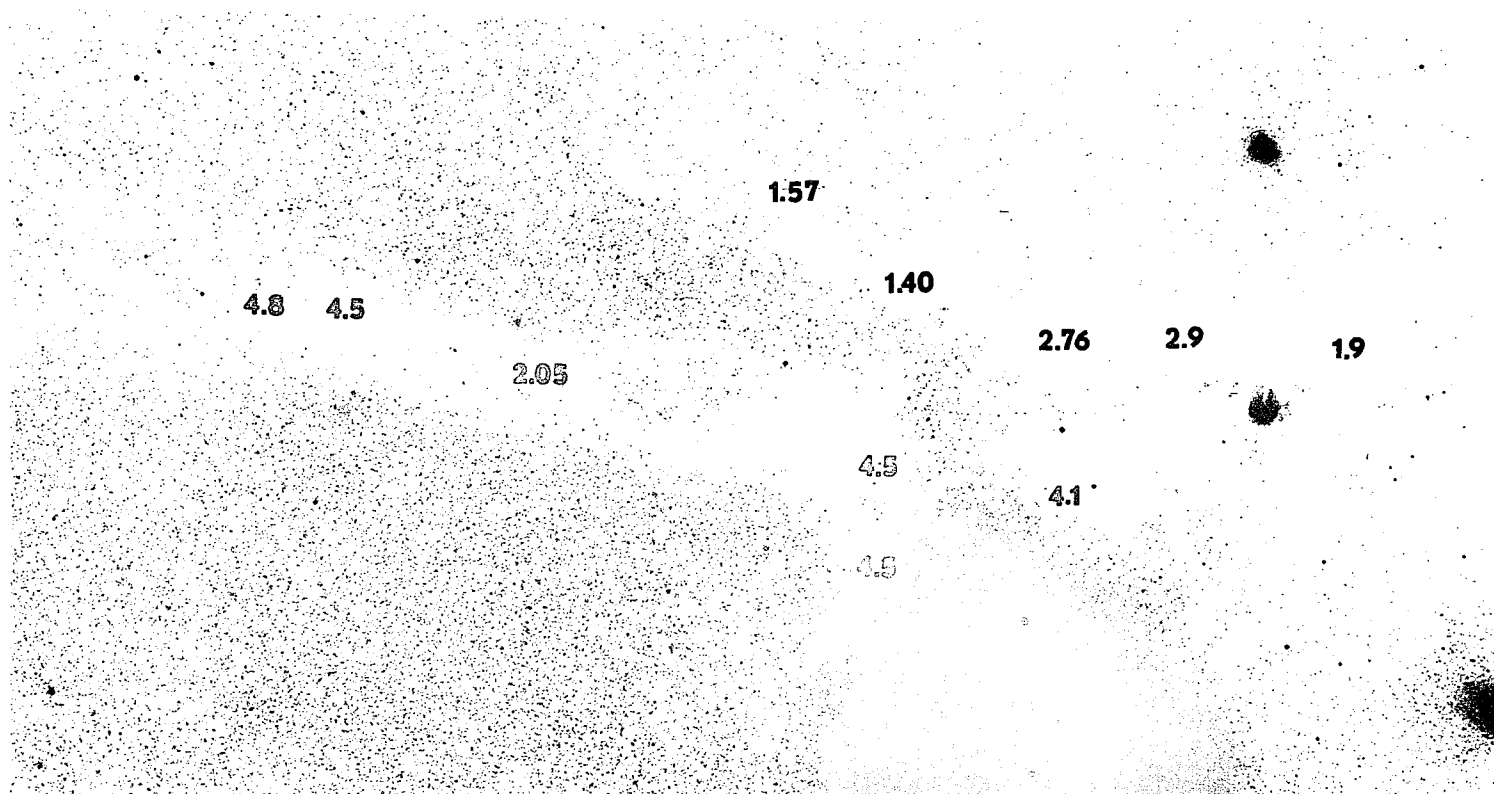photograph of the Rho Ophiuchi cloud.

Figure 5.1. CO observations of Ophiuchus cloud.

the southern "streamers" as downstream flow from the star formation region. However, this measurement is taken in a rather confused area and this radial velocity may well be a velocity component associated with the main cloud.) We take the "streamer" length to be from the tip of the "streamers" to the star formation region and assume a distance to the cloud of 150 pc and determine:

$$\text{North "streamer" age} \simeq 7 \times 10^6 \text{ yr}$$
$$\text{South "streamer" age} \simeq 5 \times 10^6 \text{ yr}$$

Thus, the ages of the streamers are identical (to within the wide limits placed upon the ages by our crude geometric assumptions), which is consistent with the idea that they are material flowing downstream from the region of star formation. This also places an upper limit on the age of the embedded stars of $5\text{-}7 \times 10^6$ years, which is consistent with estimates by Carrasco et al. (1973) of nearby stars of $(3\text{-}6) \times 10^6$ years. For a density of $\rho = 5 \times 10^3$ (see next section) for the star formation region, the free-fall time, given by

$$t_{ff} = \frac{3\pi}{32G\rho_o}^{1/2} \tag{5.1}$$

(where G is the universal gravitational constant) is 7×10^5 years. However, the actual collapse time may be considerably longer, as the collapse will be inhibited by magnetic

fields, which will be shown to be important in the next section.

The calculations of Woodward (1975, 1976) were motivated by the spiral density wave theory. However, the results of the calculations are just as applicable to a cloud being hit by a much more local shock front such as that produced by the explosion of a nearby supernovae. Ögelman and Maran (1976), for instance, have proposed that OB associations are products of a supernovae cascade process. In this scheme massive stars are formed as the shock wave from a supernova propagates through the medium. These massive stars, themselves, later become supernovae and the cascade thus proceeds. Such a process for the formation of large associations is suggested by the subclustering of stars in associations and the positive total energies of the systems. Whatever the origin of the shock, we have presented considerable evidence which indicates that this cloud and the stars within it have been formed by a shock driven implosion.

5.1.3 Role of Magnetic Field in Cloud Evolution

Spitzer (1968) has shown that the time scale for diffusion of a magnetic field from a cloud is given by

$$t_D = 5.3 \times 10^{13} \, n_i/n_H \text{ years} \qquad (5.2)$$

(where n_i is the ion number density) for a gas temperature of less than 50°K. Carrasco et al. (1973) have shown that $t_D \simeq 10^6$-10^7 yr for the central region of the Ophiuchus cloud and, since the relative ion density should be less in the "streamers", the time scale should be longer there. Furthermore, there will be some electric charge on the grains of any dark cloud which alone will be able to maintain a magnetic field for a short time (Spitzer 1963). Thus, the magnetic field should not have had time to diffuse out if our estimates of the cloud age in the previous section are correct.

Our strategy will be to compare the pressures due to magnetic fields (P_B), dynamics (P_D), and thermal motions of gas (P_G) given respectively by

$$P_B = \frac{B^2}{8\pi} \tag{5.3}$$

$$P_D = \rho V^2 \tag{5.4}$$

$$\text{and} \quad P_G = \frac{\rho k T}{\mu} \tag{5.5}$$

(where B is the magnetic field strength, ρ is the gas mass density, V is the gas velocity, T is the gas temperature, and μ is the mean atomic weight) in order to assess the relative importance of magnetic fields. However, even for magnetic field strengths and densities that might be found in dark clouds (10^{-4} Gauss and $n \simeq 10^4$ cm^{-3}), the

equipartition of gas and magnetic pressures requires gas temperatures of 100°K. Thus, for dark cloud calculations we can ignore the gas pressure.

Unfortunately, there have been no direct detections of a magnetic field in the Ophiuchus cloud, although Chaisson (1975) has estimated the B field strength as $\simeq$ 5 x 10^{-4} Gauss from Zeeman splitting microwave observations of OH and from the polarization to absorption ratios of Carrasco et al. (1973). Additionally, Carrasco et al. (1973) have estimated B at several 10^{-4} Gauss by assuming that $n_H \simeq$ 5 x 10^3 and that the field is frozen into the gas. In this case the magnetic flux per unit mass must be conserved so that $B \propto n^{2/3}$. Thus, we can estimate the magnetic field strength at the center of the cloud as $B \simeq$ 5 x 10^{-4} Gauss and $P_B \simeq$ 1 x 10^{-8}.

Encrenaz, Falgarone, and Lucas (1975) have estimated the total mass of the central region of the Rho Ophiuchi dark cloud as 2000 $M_\odot$ via ^{13}CO observations, which imply a density consistent with the $n_H \simeq$ 5 x $10^3/cm^3$ found by Carrasco et al. (1973). However, much of the gas may be in the form of H_2. Using the standard gas to dust law, $n_{(H+H_2)}$ = 2 x 10^{21} [A_v(mag)]/[ℓ(cm)] cm^{-3}, with A_v = 50 and ℓ = 2.8 pc, we obtain $n_{H_{TOTAL}} \simeq$ 1.2 x 10^4 cm^{-3}. Thus we can estimate the mass density of the central region as $\rho \simeq$ 3.2 x 10^{-20} gm/cm^3.

The ^{12}CO radial velocity observations listed in table 5.1 show a radial velocity gradient of about 1.7 km/s, which also appears as a smaller gradient of 0.5 km/s in H_2CO (Myers and Ho 1975). These appear to be the first detection of overall mass motions in the central Ophiuchus region. Turbulent motions within the cloud may be estimated from the line widths of various molecules: H_2CO, $\Delta V = 0.7$ km/s (Heiles 1973), $\Delta V = 1.3$ km/s (Dieter 1975); OH, $\Delta V = 1.4$ km/s (Cudaback and Heiles 1969); ^{13}CO, $\Delta V = 0.7$ km/s (Encrenaz 1975); and ^{12}CO, $\Delta V = 1.4$ km/s (Gottlieb 1974). Thus, all turbulent velocities seem to be smaller than the 1.7 km/s mass motion velocities we have detected, and we may use this as the maximum dynamic velocity near the central region.

The turbulent velocities, themselves, are wholly inadequate to prevent the collapse of the cloud as, too, is rotation of the cloud. Larson (1972) has shown that the rotational velocity required to stabilize a cloud is given by

$$V_{rot} > 5^{1/2}[0.42(GM/R) - R_g T_K]^{1/2} \qquad (5.6)$$

where R_g is the gas constant. For the Ophiuchus cloud this implies $V_{rot} > 4.6$ km/s. No velocity gradient of order $2V_{rot}(9.2$ km/x$)$ is seen across Ophiuchus. However, if the 1.7 km/s velocity gradient is due to cloud rotation, this

could help retard the collapse, especially if the rotational inclination is large.

Using 3.2×10^{-20} gm/cm^3 as the mass density of cloud material, 1.7 km/s as the maximum dynamic velocity, and the magnetic field strength as 5×10^{-4} Gauss, we calculate $P_B/P_D \simeq 11$. Thus, the magnetic field is important in the evolution of this part of the cloud and will be a major pressure to resist cloud collapse. The magnetic field needed to completely resist the gravitational collapse of a cloud of radius R and density ρ is given by (Spitzer 1968)

$$B \gtrsim (4\pi/\sqrt{5})G^{1/2}R\rho. \qquad (5.7)$$

The initial density can be determined as the sum of the present gas density and the gas density lost due to star formation (the embedded source mass density corrected for the undetected low luminosity stars, which is discussed in the next chapter), for which we find $\rho = \rho_{gas} + \rho_{stars} = 4.8 \times 10^{-20}$ gm/cm^3. The radius of the star formation region is 1.4 pc. With these values we find $B \gtrsim 3 \times 10^{-4}$ Gauss. This value is consistent with the field estimates by Chaisson (1975) of $B \lesssim 5 \times 10^{-4}$ Gauss. However, since the cloud did collapse, the actual field strength must be somewhat less than 3×10^{-4} Gauss.

Estimating the relative effects of magnetic pressure in the "streamer" region is more difficult, as there are no

estimates of the gas density or B field strengths. Let us consider the larger, southern "streamer". The average width of this "streamer" is 1.5 pc and, assuming a cylindrical cross section, the ratio, A_V/pc, may be determined from five stars for which we have estimated A_V in Chapter 4. The results are listed in table 5.2 where we list the star number and optical depth in magnitudes from table 4.3, the path length in parsecs through the streamer, and the individual A_V/pc ratios. The resultant value of $A_V/pc = 2.69 \pm .48$ mag/pc when combined with the standard gas to dust ratio law, $n_{H_{TOTAL}} = 2 \times 10^{21} [A_V(mag)]/[\ell(cm)]$ cm^{-3}, gives a mean density to the "streamers" of $n_{H_{TOTAL}} \simeq 2 \times 10^3$ cm^{-3}. With the low optical depth of the "streamer" material as seen in table 5.2 most of the gas will be in the form of hydrogen atoms and the mass density is then $\rho_{H_{TOTAL}} \simeq 3.5 \times 10^{-21}$ gm/cm^3.

The strength of the magnetic field can be estimated if we assume that the field is "frozen" into the gas whereby

$$B = \left[\frac{n_{H_{TOTAL}}}{n_{interstellar}} \right]^{2/3} \times 7 \times 10^{-6} \text{ Gauss,} \qquad (5.8)$$

where 7×10^{-6} Gauss is taken to be the field strength in the interstellar medium. From this we determine $B = 2 \times 10^{-4}$ Gauss and $P_B \simeq 1.6 \times 10^{-9}$. The dynamic velocity can be taken as the difference in radial velocity between the "streamer" and the star forming region. We obtain $P_B/P_D \simeq$

Table 5.2. Determination of A_v/pc for southern "streamer" of Ophiuchus dark cloud

Star No.	A_v(H-K)	Depth (pc)	A_v/pc
95	2.6	1.40	1.86
110	3.4	1.25	2.72
96	6.5	1.40	4.64
106	2.3	1.30	1.77
108	2.6	1.05	2.48
		Average, in mag pc =	2.69 ± .48

15. Thus, it appears that cloud material is constrained to follow the magnetic field lines as it flows downstream from the cloud.

5.2 Corona Austrina Cloud

5.2.1 Field Geometry

The magnetic field geometry of the Corona Austrina cloud is displayed in figure 4.9. It can be seen that the field very smoothly follows the outline of cloud material. There are no places of apparent position angle confusion, indicating twisted fields, multiple clouds, or alignment due to other mechanisms. Furthermore, there are no regions of especially large or small polarizations, indicating a uniform degree of alignment throughout the cloud. All of these facts indicate that the cloud material and the magnetic field have become locked into one another.

The only sharp twist in the field and cloud is in the region of star formation centered upon R and T CrA. Here the cloud makes a rather sharp 90° turn and the polarization position angles change from near 30° west of R and T to near 120° east of them. It is interesting to note that this region of star formation is the point of the cloud nearest the galactic plane. This is illustrated in figure 5.2, where the orientation of the galactic plane is drawn with respect to the cloud. It is also apparent that the

Figure 5.2.   Orientation of galactic plane with respect to
              the Corona Austrina dark cloud.

              The orientation of the galactic plane is
              superimposed over a photograph of the Corona
              Austrina dark cloud (see caption for figure
              4.9).   The galactic plane is approximately
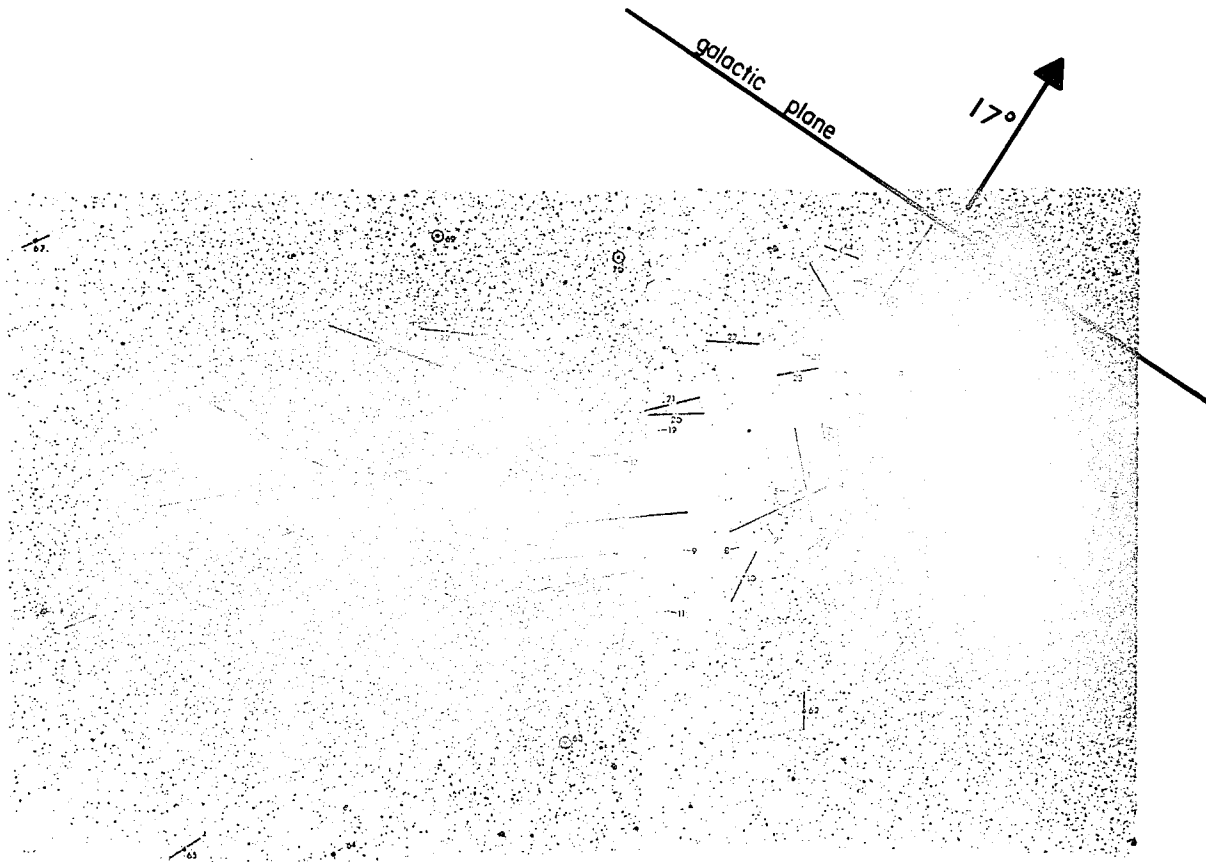   17° away in the direction of the arrow.

Figure 5.2. Orientation of galactic plane with respect to the Corona Austrina dark cloud.

region of star formation has the highest visual obscuration
and probably gas density. These facts imply that material
is either leaving the star formation along the field lines
or, more likely, is falling along the field lines into the
region of star formation.

5.2.2 Scenario for Cloud Formation

Parker (1966) investigated the effects on gas of the
force of the gravitational field of stars in the galactic
disk opposing the forces due to magnetic field pressure,
cosmic ray pressure, and gas pressure. The result is that
a magnetic Rayleigh-Taylor instability is set up whereby the
weight of a heavy fluid (thermal gas) is used to hold down
light fluids (magnetic field and cosmic rays). The gas
cannot move along the magnetic field lines because of the
gravitational field and cannot expand across the field lines
without expending energy. A schematic diagram of this
instability may be seen in figure 2 of Parker (1966). This
instability, which traps the gas into clouds, has been in-
vestigated for several simple geometries, all of which have
proven to be unstable. Shu (1974) has investigated the
influence of galactic rotation by examining Parker's insta-
bility for differentially rotating disks. He finds that
no amount of differential rotation can completely suppress
this instability. However, shear will suppress wavelengths
that are long in the plane of the galaxy, and the typical

distance between clumps of gas along the field lines is of the order 1 kpc. Linear perturbation calculations by several authors (Parker 1967; Lerche and Parker 1967, 1968) indicate scales of several hundred parsecs along the field lines and down to 1 parsec or less perpendicular to the field terminating only in gravitational instability. Thus, Parker's instability seems more likely to form very large cloud complexes and OB associations rather than individual clous.

Field (1970) has pointed out the observational consequences of such a model in the region of the magnetic well where the gas is trapped: "The polarization vectors of stars shining through a cloud should rotate systematically from one side of the cloud to the other. The edges of the clouds should be sharp and should be correlated with the direction of the polarization vectors." These predictions seem to be well fit by our observations. Thus, we may list observational evidence which indicates that the Corona Austrina cloud is the product of a Parker instability:

1. The overall geometry of the cloud is identical to the idealized geometry of a Parker instability with the bottom of the magnetic trap being the point of the cloud closest to the galactic plane.

2. The highest total obscuration and star formation occur in the magnetic well.

3. The polarization vectors are smooth and parallel to the sides of the cloud.

4. The polarization vectors rotate in the expected manner across the star formation region.

5. The diameter of the star formation region and typical width of the cloud is about 1 pc, comparable to the scale of the Parker instability perpendicular to the field.

Recently Loren (1975) investigated ^{12}CO emission from the star formation region of this cloud. He found that the broadest CO profiles ($\Delta V = 5.1$ km/s) are centered near R CrA and gradually become narrower until reaching a background of 1.5-2.0 km/s. The variations of ΔV are not fit by turbulent models but are consistent with a cloud undergoing non-homologous ($V \propto r^{-1/2}$) collapse or expansion. If the cloud is collapsing, $V(r)$ is that expected for a collapsing proto-star (Larson 1972). However, an expanding stellar wind model cannot be ruled out, since Strom, Strom, and Grasdalen (1975) have shown that stellar winds can effect a region as large as the enhanced line width region of this cloud.

Inspection of figure 4.9 shows that much dark cloud material exists outside of the star formation region but confined to the magnetic channels. This material must be falling into the star formation region along the field lines.

Thus, it is more likely that the star formation region is in a state of collapse. Additionally, the free-fall time for the cloud, $t_{ff} \simeq 6 \times 10^5$ yr (obtained using equation (5.1) and $n_{H_{TOTAL}} \simeq 4600$, see next section), is comparable to the maximum age of 10^6 years determined for TY and R CrA by Knacke et al. (1973). This indicates that the cloud is not old enough to have begun re-expansion.

5.2.3 Role of Magnetic Field in Cloud Evolution

Strom, Strom and Grasdalen (1974) have estimated the density near the center of this cloud as $n \simeq 2 \times 10^5$ cm^{-3} on the basis of visual absorption estimates to an embedded IR source. This is in good agreement with the densities inferred by Black and Fazio (1973) from the observed flux of γ-rays of energy >100 Mev. ^{12}CO observations by Loren (1975) suggests that $n_{H_2} \simeq 4400$ cm^{-3}. However, if the carbon abundance is depleted somewhat in this cloud, Loren's estimate could be too small. We will assume $n_{H_{TOTAL}} \simeq 2 \times 10^5$ cm^{-3}.

The variations of ^{12}CO line widths across the face of the cloud are so smooth as to eliminate turbulent models. Also, Loren's ^{12}CO maps show no measurable radial velocity differences anywhere in the cloud. Thus, turbulence and cloud rotation are not important in the prevention of cloud collapse while magnetic fields play a dominant role.

However, since the cloud has apparently collapsed, equation (5.7) may be used to set an upper limit on the field streng strength of $B \lesssim 4.3 \times 10^{-3}$ Gauss, assuming $\rho = 6.8 \times 10^{-19}$ gm/cm^3 and $R = 1.3$ pc (the radius of the ^{12}CO cloud). This is in excellent agreement with $B = 5 \times 10^{-3}$ Gauss derived from equation (5.8) assuming the field is frozen in. We adopt $B \simeq 4 \times 10^{-3}$ Gauss at the cloud center. The dynamic velocity at the cloud center is determined from the maximum line widths of ^{12}CO observed there ($\Delta V \simeq 5.1$ km/s). With these values we obtain $P_B / P_{D(\text{cloud center})} \simeq 3$.

For regions away from the cloud center the number density of particles must decrease. Since the grain alignment is good in the outer regions, we can assume $n_{H_{\text{TOTAL}}} <$ 2×10^4/cm^3 (Goldreich and Kwan 1974). If the field is frozen in, $B \lesssim 1 \times 10^{-3}$ Gauss. The background ^{12}CO line widths (Loren 1975) are approximately 1.7 km/s. Thus, away from the region of star formation $P_B/P_D \gtrsim 20$. These results are then consistent with material being well confined as it flows into the magnetic trap, whence gravitational instability becomes dominant.

5.3 NGC 1333

5.3.1 Field Geometry and Scenario for Cloud Evolution

The magnetic field geometry of NGC 1333 is displayed in figure 4.10. The most outstanding feature of this

diagram is that there appear to be two components to the magnetic field. One component covers the western and central regions and is at position angles 90 to 120 degrees. The other component is to the east and is at position angles 0 to 30 degrees. This geometry suggests that there may be two clouds, each with a uniform magnetic field at different position angles superimposed upon one another.

This picture is strongly reenforced by recent observations by Loren (1976) of NGC 1333 where he finds two velocity components (one at 6.0 ± 0.3 km/s and another at 8.3 ± 0.3 km/s), which are both seen in ^{12}CO and ^{13}CO. The 6.3 km/s component dominates the western and southern regions and corresponds well with the region of the cloud where polarization position angles are near 90 degrees. The 8.3 km/s component dominates the eastern and northern regions of the cloud where the polarization position angles are near 20 degrees.

The two velocity components overlap in a rather narrow strip that coincides with the line of visible stars, Herbig-Haro objects, CS and H_2CO emission (Lada et al. 1974), and the strip of infrared sources discussed in this dissertation in section 3.4. This region also appears at a single (no line-splitting) velocity of 7.5 km/s.

In combining the infrared observations of this thesis with observations of other authors there appears to

be an age and obscuration sequence along the strip of star formation which may be roughly broken up in the following manner:

1. At the northeast end of this strip are the visible stars BD +30° 549 and BD +30° 547, which are obscured by A_V < 5 mag. Strom, Grasdalen and Strom (1974) have estimated the age of BD +30° 549 as $\simeq 10^6$ years.

2. Further to the southwest is a region of embedded IR sources (this thesis) and Herbig-Haro objects 7, 8, 9, 10, and 12. Grasdalen et al. (1973) have estimated the age of Herbig-Haro objects as a few times 10^5 years. There is an apparent obscuration increase in this region from northeast to southwest noted from the infrared observations listed in table 3.7: source no. 2 (Lk Hα 270), $A_V \simeq 11$; source 15, $A_V \simeq 11$; source 12, (H-H 12) $A_V \simeq 30$; and source 16, $A_V \simeq 42$.

The regular pattern of the long strip of visible stars, Herbig-Haro objects, and infrared sources in itself suggests a very young age. Loren (1976) has suggested a cloud model wherein two clouds are colliding with a relative line of sight velocity of about 2 km/s. The nearer cloud (8.3 km/s) is the denser and is more likely a thin shell section rather than a spherical cloud. Although the

relative cloud velocities are thought to be more or less in the line of sight, a transverse velocity of the foreground cloud to the southwest could explain both the age and obscuration sequence. If the transverse velocity is also 2 km/s at a cloud distance of 500 pc, the length of the overlap region corresponds to 1.9×10^6 years, in good agreement with the estimated age of the oldest stars in the sequence.

Stone (1970a, 1970b) has discussed the effects of a collision between two identical, "standard" clouds of 350 $M_\odot$ each at a relative velocity of 20 km/s. This work was suggested by the observations of calcium emission from clouds which show that they move with an r.m.s. velocity of about 10 km/s. Individual clouds moving at this velocity will typically undergo a collision every 6×10^6 years. With the usual "standard" cloud initial conditions, the minimum mass for gravitational instability is about 600 $M_\odot$. Stone's results show that after an initial compression, the clouds undergo an expansion, during which about 25 percent of the initial mass is lost. Thus, while the clouds as a whole will not become gravitationally unstable, there may be local high density regions with densities as high as 100 times that of the original density and where star formation may take place.

Only when collisions with relative velocities of 1 km/s or less occur will mass loss be small enough that

total gravitational instability will occur. Thus, a typical cloud should be seen expanding at about 1 km/s, which is the typical expansion velocity. If a cloud's lifetime is then 6×10^6 yr (time between collisions), then a typical cloud will not be able to grow larger than about 10 pc. The problem is that a few clouds statistically will avoid collisions for much longer than 6×10^6 yr, so that within a very few collision times the clouds will have diffused into a rather uniform medium, where dark cloud remnants have only small density gradients. Thus, whereas certain clouds may indeed collide to provide a place for stars to form, this model does not fit our observational picture of star formation or the interstellar medium.

Sancisi et al. (1974) have mapped the HI velocity field near NGC 1333. They find an expanding HI shell which intersects the velocity of the ambient component in the region of NGC 1333. This shell is thought to be due to the product of a nearby supervoa explosion (Öpik 1953). Loren (1976) argues that the foreground CO cloud is part of the expanding shell and this is most likely in the shape of a flattened sheet. Apparently the geometry of colliding clouds is important in determining the efficiency in forming gravitationally bound condensations. In Stone's (1970a, 1970b) models only one-dimensional compression was able to occur, since gas was able to squeeze out of the clouds'

interface and not be compressed. The flattened sheet geometry could be considerably more efficient in this process and help explain the apparent high efficiency of compression and star formation (to be discussed in the next chapter).

Sancisi (1970, 1974) and Sancisi et al. (1974) have shown that the expanding HI shell coincides with a string of star-forming dark clouds and OB associations beginning with NGC 1333 in the south (age $\simeq$ 2 x 10^6 yr), IC 348 (age $\simeq$ 2 x 10^7 yr) to the north, and even farther to the north the much older Perseus OB 2 association. This suggests that expanding supernovae shells are a highly efficient mechanism for the formation of OB associations consistent with the results of Ögelman and Maran (1976).

5.3.2 Role of Magnetic Fields

If the young stars formed in NGC 1333 are due to a supernova shock implosion, the pre-shocked cloud did not collapse to form stars prior to the shock. Lada et al. (1974) have shown that thermal, rotational, or turbulent pressures are insufficient to prevent the collapse. If a magnetic pressure prevents the cloud from collapse, Lada et al. (1974) show that B $\simeq$ 2 x 10^{-4} Gauss using the cloud density they observe of $n_{H_2} \simeq$ 2 x 10^4/cm^3, a radius of 1.5 pc, and equation (5.7) They also show this field strength is consistent with that in a general contraction with the

field frozen into the gas. Assuming $B \simeq 2 \times 10^{-4}$ Gauss, the magnetic pressure is $P_B \simeq 1.6 \times 10^{-9}$.

Using the above H_2 number density, $\rho \simeq 6.8 \times 10^{-20}$ gm/cm^3, and the relative velocity of the colliding clouds as 2 km/s, the dynamic pressure is $P_D \simeq 2.7 \times 10^{-9}$ and $P_B/P_D \simeq 6 \times 10^{-1}$. Thus, the magnetic field will have little influence on the evolution of the clouds during the collision.

5.4 M78 Dark Cloud

5.4.1 Field Geometry and Scenario for Cloud Evolution

The magnetic field geometry for M78 is displayed in figure 4.8. The magnetic field geometry is somewhat sketchy due to the small number of background stars we were able to observe, but there is a definite indication of a radial geometry. We also note that the unpolarized stars mostly occur near the cloud center where depolarization effects are likely to occur. There are no indications in any ^{12}CO surveys of large scale mass motion or unusually great turbulence (Milman et al. 1975; Tucker, Kutner, and Thaddeus 1973; and Brown et al. 1975). These facts, plus the large number of embedded stars discovered in this thesis (see Chapter 3), indicate that the cloud has undergone a radial collapse which has pulled in with it a "frozen-in" magnetic field.

5.4.2 Role of the Magnetic Field in Cloud Evolution

Lada et al. (1974) have estimated the density of H_2 for M78 at $10^4/cm^3$. With this and equation (5.8) we derive $B \simeq 7 \times 10^{-4}$ for the field frozen-in during cloud collapse and thus $P_B \simeq 2 \times 10^{-8}$. The typical cloud radius is estimated at 11 pc by Tucker et al. (1973) from ^{12}CO observations, which agrees well with the typical radius of high obscuration. With these parameters and equation (5.7), the magnetic field necessary to keep the cloud from collapsing is found to be $B \simeq 1.8 \times 10^{-3}$ Gauss. Thus, as we anticipated above, the magnetic field strength even of a field frozen into the gas is not sufficient to prevent this cloud from collapsing.

Brown et al. (1973) have shown that the largest turbulent velocities in M78 are seen in the 142α and 166α carbon recombination lines ($\Delta V \simeq 1.3$ km/s). Other, larger line widths seen in ^{12}CO are due principally to saturation and radiation trapping effects. Thus, the largest dynamic pressure is $P_B \simeq 5.8 \times 10^{-10}$ and $P_B/P_D \simeq 35$.

5.5 Discussion

In this section we have attempted to estimate the magnetic field strength for several clouds, determine a likely mechanism for the cloud evolution, and estimate the relative effect of the magnetic field with respect to the

dynamic pressure based on the largest mass motion or turbu-
lent velocities. Table 5.3 summarizes the results. The
formation of M78 and Corona Austrina dark clouds occur
through essentially quiescent collapse processes, and for
these P_B/P_D are larger than for the Rho Ophiuchi and NGC
1333 clouds, which are imploded through shock processes.
Table 5.4 summarizes the cloud formation scenarios. Thus,
while there might be a rough correlation between the rela-
tive magnetic field pressures and the method of cloud forma-
tion, in all cases the magnetic field has a significant role
in the evolution of the clouds, with the possible exception
of NGC 1333.

Table 5.3. Ratio of magnetic to dynamic pressures

Cloud	Cloud Formation Scenario	P_B/P_D
M78	quiescent collapse?	36
Corona Austrina	Parker instability	$\gtrsim 20$
Rho Ophiuchi	shock front	15
NGC 1333	cloud-cloud collision (supernova shock)	6×10^{-1}

Table 5.4. Summary of cloud formation mechanisms

Cloud	Most likely formation scenario	Other mechanisms		Major evidence against
Rho Ophiuchi	galactic or supernova shock	cloud-cloud collision	--	no two-component velocity structure
		Parker instability	--	magnetic field structure
		quiescent collapse	--	"streamers"
R Corona Austrina	Parker instability	cloud-cloud collision	--	no two-component velocity structure
		shock-induced	--	wrong morphology
		quiescent collapse	--	wrong magnetic field structure
NGC 1333	two-cloud collision	shock-induced	--	probably caused by two-cloud collision
		Parker instability	--	magnetic field structure
		quiescent collapse	--	two-component velocity structure

Table 5.4--Continued. Summary of cloud formation mechanisms

Cloud	Most likely formation scenario	Other mechanisms	Major evidence against
M78 (Lynds 1630)	quiescent collapse	Parker instability	-- magnetic field structure
		shock-induced	-- magnetic field structure
		cloud-cloud collision	-- no two-component velocity structure

CHAPTER 6

EFFECTS OF MAGNETIC FIELDS AND CLOUD
DYNAMICS ON STAR FORMATION

In this section we investigate the ability of the various clouds discussed above to form stars. To do this in a quantitative manner, we define the efficiency of star formation, ESF, as

$$ESF = \frac{M_{stars}}{M_{cloud}} = \frac{M_{stars}}{M_{gas} + M_{stars}} , \qquad (6.1)$$

where M_{stars} is the total mass of all stars in a cloud and M_{gas} is the mass of the cloud not used during star formation. A number of uncertainties arise in determining ESF:

1. The total number of stars embedded in the cloud is uncertain, as is the mass of individual stars. This problem is discussed in the following section.

2. The masses of the clouds are uncertain, since the density distributions are not, in general, known and the volume of the clouds can only be approximated by their projection on the plane of the sky and their distance.

3. The worst problem in trying to quantify ESF is that different clouds may be at different stages of

evolution. That is, while a cloud may have completed recent star formation another may only be beginning. There is no certain way to overcome this problem, except in understanding cloud evolution from the scenarios suggested above. Thus, while the Rho Ophiuchi cloud may have completed star formation, NGC 1333 is likely just beginning since the colliding clouds have not yet completely intersected.

6.1 Total Masses of Stars in Clouds

6.1.1 Rho Ophiuchi Cloud

In Chapter 4 we discovered an embedded cluster of 67 stars in the Rho Ophiuchi cloud and noted that the derived $\rho(M_K)$ of the cluster is similar to the Salpeter (1953) luminosity function. If $(V-K) \simeq 0$ for the O and B stars, we find, using our derived foreground absorption listed in table 3.1, that we have only sampled the star cluster for stars more luminous than $M_V = +2$. Assuming that stars of different luminosities are randomly distributed in the cluster, we can correct for the undetected low luminosity end of the Salpeter luminosity function between $M_V = +2$ to $M_V = +11$. We find

$$\frac{\Sigma[\Psi(\text{brighter than } M_V = +11)]}{\Sigma[\Psi(\text{brighter than } M_V = +2)]} \simeq 7.7,$$

which implies that the total number of stars formed is approximately 510.

There is another, very crude, method of checking this result with the p/A ratios determined in Chapter 4. From figure 4.6 we note that p/A decreases assymptotically from .065 to 0.2 in the first eight magnitudes of absorption. If the decrease in p/A of a factor of 3 is due to individual clouds representing fragmentation remnants, we can write $3R_{frag} = 8$(mag of A_v), where R_{frag} is the radius of a typical fragment. From the discussion in Chapter 3, 30 magnitudes of absorption corresponds to 1.4 pc, so that $R_{frag} \simeq$ .17 pc. Thus, the total number of fragments is given by

$$\text{Number of Fragments} \leq \left(\frac{1.4}{.17}\right)^3 = 560 \text{ ,}$$

where the equal sign is in the case that the cloud is totally filled by the fragments. While there is no claim made as to the meaningfulness of this calculation, it is interesting to note that the result is consistent with the more direct method above.

If there are 510 embedded stars, each with an average mass of $2M_\odot$, then $M_{stars} \simeq 1020\ M_\odot$.

6.1.2 M78 Cloud

In section 3.2 we reported the discovery of 70 embedded stars in M78. Since this cluster also closely resembles the high luminosity end of the Salpeter luminosity

function, we correct for the undetected faint end in the same manner as for the Rho Ophiuchi cloud and find 540 total stars. For a typical mass of $2M_\odot$ apiece, $M_{stars} \simeq 1080\ M_\odot$.

6.1.3 Corona Austrina Cloud

In section 3.3 we reported the discovery of 19 stars embedded in the Corona Austrina cloud. It is not likely that there is an appreciable number of additional stars which we did not detect since:

1. A high percentage of the sources we discovered are associated with visible stars.

2. The distribution of K magnitudes of the discovered sources cuts off well above the mapping detection limit.

3. Loren (1975) does not report a large number of ^{12}CO hot spots which are often associated with embedded stars.

   If a typical stellar mass is $2M_\odot$, then $M_{stars} \simeq 38$.

6.1.4 NGC 1333 Cloud

In section 3.4 we reported the discovery of 25 stars embedded in the NGC 1333 cloud. This must be a lower limit to the number of stars that will eventually be formed in this region, as the two colliding clouds have just begun to intersect. If we make the rough correction that future star formation takes place at the present rate, until the clouds

no longer intersect, then approximately 200 stars will eventually be formed. This, of course, is a lower limit to the number of stars which may form, since it does not take into account stars which were below our infrared detection limit. Lada et al. (1974) have shown that the stars formed in NGC 1333 have $M < 3M_\odot$. If we again assume $2M_\odot$ per star, $M_{stars} \simeq 400$.

6.2   Star Formation Efficiency

In table 6.1 are listed the calculated star formation efficiencies which were determined using the M_{star} discussed above and the cloud total masses based on the densities and sizes listed in the previous chapters. Also listed is the ratio of magnetic to dynamic pressures and the magnetic field strengths derived in the previous chapter.

Inspection of this table shows two things. First, there apparently is no correlation between B and ESF. Secondly, there does seem to be a strong correlation between ESF and P_B/P_D. These correlations suggest that magnetic fields do not have a first order effect on ESF. Rather, ESF (that is, the ability of a cloud to form very high density regions) is controlled almost solely by the mechanism of star formation.

It is also clear that dynamic processes are more efficient. The simple two cloud collision (NGC 1333) most

easily converts kinetic energy into cloud compression. An isolated cloud hit by a shock front (Rho Ophiuchi), although producing a concentrated region of star formation, is not nearly as efficient with respect to the total cloud mass. It is interesting to note that the ESF of 8% determined for this cloud is close to the 5% predicted by Woodward's (1975, 1976) models.

The results in table 6.1 indicate that dynamic pressures are important in controlling the ability of clouds to form stars. The role of the magnetic pressure in this process must still be viewed with caution since the field strengths derived from the assumptions of field freezing and the sense of the virial (expansion or collapse) are subject to large uncertainties. The quantitative role of magnetic fields in cloud collapse must await independent measurements of the field strengths.

Table 6.1. Star formation efficiencies

Cloud	ESF(%)	P_B/P_D	B(G)
NGC 1333	≥ 28	6×10^{-1}	2×10^{-4}
Rho Ophiuchus	8	11	5×10^{-4}
M78	2	36	7×10^{-4}
Corona Austrina	<1	$\gtrsim 20$	2×10^{-4}

LIST OF REFERENCES

Barnard, E. E. 1927, in Photographic Atlas of Selected
        Regions of the Milky Way, ed. E. B. Frost and M. R.
        Calvert (Washington D.C.: Carnegie Institute of
        Washington).

Blaauw, A. 1964, Ann. Rev. Astron. and Ap., 2, 213.

Black, J. H. and Fazio, G. G. 1973, Ap. J. (Letters), 185,
        L7.

Bless, R. C. and Savage, B. D. 1972, Ap. J., 171, 293.

Bok, B. J. 1937, The Distribution of Stars in Space,
        (Chicago: University of Chicago Press).

Bok, B. J. and Cordwell, C. S. 1973, in Molecules in the
        Galactic Environment, ed. M. A. Gordon and L. F.
        Snyder (New York: Interscience Publishers).

Bok, B. J. and Reilly, E. 1947, Ap. J., 105, 255.

Bottlinger, K. F. and Schneller, H. Z. 1930, A. Zh., 1,
        339.

Brown, R. L., Knapp, G. R., Kuiper, T. B. H., and Kuiper,
        E. N. R. 1975, Ap. J. (Letters), 195, L23.

Carrasco, L., Strom, S. E., and Strom, K. M. 1973, Ap. J.,
        182, 95.

Chaisson, E. J. 1975, Ap. J. (Letters), 197, L65.

Cheung, A. C., Chui, M. F., Matsakis, D., Townes, C. H.,
        and Yugvessen, K. S. 1973, Ap. J. (Letters), 186,
        L73.

Coyne, G., S. J., Gehrels, T. and Serkowski, K. 1974,
        A. J., 79, 581.

Crutcher, R. M., Evans, N. J., Troland, T., and Heiles, C.
        1975, Ap. J., 198, 91.

Cudaback, D. D. and Heiles, C. E. 1969, Ap. J. (Letters),
        155, L21.

Curtis, H. D. 1919, The Adolfo Stahl Lectures in Astronomy,
        (San Francisco: The Astronomical Society of the
        Pacific), p. 98.

Davis, L. and Greenstein, J. L. 1951, Ap. J., 114, 206.

Dickman, R. L. 1975, Ap. J., 202, 50.

Dieter, N. H. 1975, Ap. J., 199, 289.

Dolidze, M. V. and Arakelyan, M. A. 1959, Soviet Astro.-
        A. J., 3, 434.

Encrenaz, P. 1975, private communication to R. L. Brown
        and G. R. Knapp in Ap. J., 189, 253.

Encrenaz, P. J., Falgarone, E., and Lucas, R. 1975, Astr.
        and Ap., 44, 73.

Fedorovich, V. P. 1960, Variable Stars, 13, 166.

Fermi, E. 1949, Phys. Rev., 75, 1169.

Field, G. B. 1970, in Dark Nebulae, Globules, and Proto-
        stars, ed. B. T. Lynds (Tucson: University of
        Arizona Press).

Gaposchkin, S. and Greenstein, J. L. 1936, Harvard Obs.
        Bull., No. 904.

Garrison, R. F. 1967, Ap. J., 147, 1003.

Gately, I., Becklin, E. E., Matthews, K., Neugebauer, G.,
        Penston, M. V., and Scoville, N. 1974, Ap. J.
        (Letters), 191, L121.

Gold, T. 1952, MNRAS, 112, 215.

Goldreich, P. and Kwan, J. 1974, Ap. J., 189, 441.

Gottlieb, G. 1974, personal letter to author, 1 August 1974.

Grasdalen, G. L., Strom, K. M., and Strom, S. E. 1973,
        Ap. J. (Letters), 184, L53.

Greenberg, J. M. 1968, in Nebulae and Interstellar Matter,
        ed., B. M. Middlehurst and L. H. Aller (Chicago:
        University of Chicago Press).

Hall, J. S. 1937, Ap. J., 85, 145.

Hall, J. S. 1949, Science, 109, 166.

Hardy, E. and Mendoza, E. E. 1968, Assoc. Argent. Astr. Bol., No. 14.

Haro, G. 1949, A. J., 54, 188.

Haro, G. 1953, Ap. J., 117, 73.

Hartmann, J. 1904, Ap. J., 19, 268.

Harwit, M. 1970, Nature, 226, 61.

Hayden, F. A. 1952, Photographic Atlas of the Southern Milky Way, (Washington D.C.: Carnegie Institute of Washington).

Heiles, C. E. 1969, Ap. J., 157, 123.

Heiles, C. E. 1973, Ap. J., 183, 441.

Herbig, G. H. 1974, Lick. Obs. Bull., No. 658.

Herbig, G. H. 1975, Ap. J., 196, 129.

Herbig, G. H. and Kuhi, L. V. 1963, Ap. J., 137, 398.

Herbig, G. H. and Rao, N. K. 1972, Ap. J., 174, 401.

Herschel, W. 1784, Phil. Trans. Roy. Soc. London, A74, 437.

Hiltner, W. A. 1949, Science, 109, 165.

Hiltner, W. A. 1956, Ap. J. Suppl., 2, 389.

Hjalmarson, Å., Sume, A., Elldér, J., Rydbeck, O. E. H., Moore, E., Huguenin, R., Sandquist, A. A., Lindblad, P. O., and Lindroos, P. 1975, Research Laboratory of Electronics and Onsala Space Observatory Research Report No. 124.

Hubble, E. 1922, Ap. J., 56, 162.

Hulst van de, H. C. 1945, Ned. Tijdschr. Natuurk., 11, 201.

Hulst van de, H. C. 1967, Ann. Rev. Astron. and Ap., 5, 167.

Johansson, L. E. B., Höglund, B., Winnberg, A., Nguyen-Q-
    Rieu, and Goss, W. M. 1974, Ap. J., 189, 455.

Johnson, H. L. 1968, in Nebulae and Interstellar Matter,
    ed. B. M. Middlehurst and L. H. Aller (Chicago:
    University of Chicago Press).

Jones, R. V. and Spitzer, L. 1967, Ap. J., 147, 943.

Kamp van de, P. 1932, A. J., 42, 97.

Kaplan, S. A. and Pikelner, S. B. 1970, The Interstellar
    Medium, (Cambridge: Harvard University Press).

Khavtassi, J. 1955, Bull. Abastumani Obs., No. 18.

Kinman, T. D. and Mahaffey, C. T. 1974, Publ. A. S. P.,
    86, 336.

Knacke, R. F., Strom, K. M., Strom, S. E., and Young, E.
    1973, Ap. J., 179, 847.

Lada, C. J., Gottlieb, C. A., Litvak, M. M., and Lilley,
    A. E. 1974, Ap. J., 194, 609.

Larson, R. B. 1972, MNRAS, 156, 437.

Lerche, I. and Parker, E. N. 1967, Ap. J., 149, 549.

Lerche, I. and Parker, E. N. 1968, Ap. J., 154, 515.

Lilley, A. E. 1955, Ap. J., 121, 559.

Lin, C. C., Yuan, C., and Shu, F. H. 1969, Ap. J., 155,
    721.

Loren, R. B. 1975, Thesis, University of Texas, Austin.

Loren, R. B. 1976, Ap. J., in press.

Loren, R. B., Vanden Bout, P. A., and Davis, J. H. 1973,
    Ap. J. (Letters), 185, L67.

Lundmark, K. 1926, Upp. Obs. Medd., No. 12.

Lynds, B. T. 1962, Ap. J. Suppl., 7, No. 64, 1.

Martin, P. G. 1971, MNRAS, 153, 279.

Mathewson, D. S. and Ford, V. L.   1970, Mem. R. A. S., 74, 139.

Milman, A. S., Knapp, G. R., Kerr, F. J., Knapp, S. L., and Wilson, W. J.   1975, A. J., 80, 93.

Morris, M., Zuckerman, B., Palmer, P., and Turner, B. E. 1973, Ap. J., 186, 501.

Myers, P. C. and Ho, P. T. P.   1975, Ap. J. (Letters), 202, L25.

Ögelman, H. and Maran, S. P.   1976, Ap. J., in press.

Öpik, E. J.   1953, Irish A. J., 2, 219.

Parker, E. N.   1966, Ap. J., 145, 811.

Parker, E. N.   1967, Ap. J., 149, 535.

Penzias, A. A., Soloman, P. M., Jefferts, K. B., and Wilson, R. W.   1972, Ap. J. (Letters), 174, L43.

Plaskett, J. and Pearce, J. A.   1933, Publ. Dom. Ap. Obs., 5, 167.

Purcell, E. M. and Spitzer, L.   1971, Ap. J., 167, 31.

Rees, M. J. and Reinhart, M.   1972, Astron. and Ap., 19, 189.

Richtmeyer, R. D. and Teller, E.   1949, Phys. Rev., 75, 1729.

Roberts, W. W.   1969, Ap. J., 158, 123.

Rosino, L.   1960, Cont. Asiago, No. 109.

Russell, H.   1922, Proc. Nat. Acad. Sci., 8, 115.

Rydbeck, O. E. H., Kollberg, E., Hjalmarson, Å., Sumé, A., Elldér, J., and Irvine, W. M.   1975, Onsala Space Observatory Research Report No. 120.

Salpeter, E. G.   1953, Symposium on Astrophysics, (Ann Arbor: University of Michigan Press).

Sancisi, R.   1970, Astron. and Ap., 4, 387.

Sancisi, R.   1974, Proc. I. A. U. Symp. No. 60, 115.

Sancisi, R., Goss, W. M., Anderson, C., Johansson, L. E. B., and Winnberg, A. 1974, Astron. and Ap., 35, 445.

Serkowski, K. 1969, Ap. J. (Letters), 158, L107.

Serkowski, K. 1973, in Interstellar Polarization; I. A. U. Symposium No. 52, ed. J. M. Greenberg and H. C. van de Hulst (Dordrecht, Holland: D. Riedel Publ. Co.).

Serkowski, K., Mathewson, D. and Ford, V. 1975, Ap. J., 196, 261.

Shain, G. A. 1955, Astrom. Zh., 32, 381.

Shu, F. H. 1974, Astr. and Ap., 33, 55.

Shu, F. H., Milione, V., Gebel, W., Yuan, C., Goldsmith, D. W., and Roberts, W. W. 1972, Ap. J., 173, 557.

Shu, F. H., Milione, V., and Roberts, W. W. 1973, Ap. J., 183, 819.

Simon, M., Righini, G., Joyce, R. R., and Gezari, D. Y. 1973, Ap. J. (Letters), 186, L127.

Snow, T. P. and Cohen, J. G. 1974, Ap. J., 194, 313.

Spitzer, L. 1963, Origin of the Solar System, (New York: Academic Press).

Spitzer, L. 1968, Diffuse Matter in Interstellar Space, (New York: Interscience Publishers).

Stebbins, J., Huffer, C. M., and Whitford, A. E. 1940, Ap. J., 91, 20.

Stone, M. E. 1970a, Ap. J., 159, 277.

Stone, M. E. 1970b, Ap. J., 159, 293.

Strom, K. M., Strom, S. E., Carrasco, L., and Vrba, F. J. 1975, Ap. J., 196, 489.

Strom, K. M., Strom, S. E., and Grasdalen, G. L. 1974, Ap. J., 187, 83.

Strom, S. E., Grasdalen, G. L., and Strom, K. M. 1974, Ap. J., 191, 111.

Strom, S. E., Strom, K. M., and Grasdalen, G. L. 1975, Ann. Rev. Astr. and Ap., 13, 187.

Struve, F. G. W. 1847, Etudes d'astronomie stellaire, (St. Petersburg: Académie Imperiale des Sciences).

Struve, O. and Rudkjøbing, M. 1949, Ap. J., 171, 267.

Trumpler, R. J. 1930, Lick. Obs. Bull., 14, 154.

Tucker, K. O., Kutner, M. L., and Thaddeus, P. 1973, Ap. J. (Letters), 186, L13.

Veschur, G. L. 1970, Ap. J., 161, 867.

Vrba, F. J., Strom, S. E., and Strom, K. M. 1975, P. A. S. P., 87, 337.

Walker, M. F. 1956, Ap. J. Suppl., 2, 365.

Walker, M. F. 1957, Ap. J., 125, 636.

Werner, M. W., Elias, J. H., Gezari, D. Y., and Westbrook, W. E. 1974, Ap. J. (Letters), 192, L31.

Wickramasinghe, N. C. 1970, Nature, 228, 540.

Woodward, P. R. 1975, Ap. J., 195, 61.

Woodward, P. R. 1976, Ap. J., to be published.

Zellner, B. 1970, Thesis, University of Arizona.

Zuckerman, B., and Palmer, P. 1974, Ann. Rev. of As. and Ap., 12, 279.